MEASUREMENT OF SHEAR STRENGTH AND TEXTURE EVOLUTION IN BCC MATERIALS SUBJECTED TO HIGH PRESSURES

By

JUAN PABLO ESCOBEDO

A dissertation submitted in partial fulfillment of
the requirements for the degree of

DOCTOR OF PHILOSOPHY

WASHINGTON STATE UNIVERSITY
School of Mechanical and Materials Engineering

DECEMBER 2007

To the Faculty of Washington State University:

The members of the committee appointed to examine the dissertation of JUAN PABLO ESCOBEDO find it satisfactory and recommend that it be accepted.

_____

Chair

_____

_____

ACKNOWLEDGEMENT

I would like to acknowledge the guidance and support of my advisor Dr David Field for the last five years. His help both with the experimental work and the analysis, his professional attitude and easy to approach mentality are all noteworthy. I would also like to thank my committee members Dr. David Lassila, Dr. Hussein Zbib and Dr. Ding for their valuables suggestions. I would also like to thank Dr. Jeff Florando and Mary Leblanc , LLNL , for providing me with the equipment and samples for my experimental work and also for providing with valuable insight into various aspects of my research.

I also appreciate all the help and support of my friends and my group for the past five years. Last and not the least, I would thank my family for their emotional support during this period.

MEASUREMENT OF SHEAR STRENGTH AND TEXTURE EVOLUTION IN BCC MATERIALS SUBJECTED TO HIGH PRESSURES

Abstract

by Juan Pablo Escobedo , Ph.D.
Washington State University
December 2007

Chair: David P. Field

Deformation modeling of metals subjected to extreme pressures and strain rates requires an understanding of the pressure-dependent dislocation core structure and its effect upon dislocation mobility. The core structure and dislocation mobilities can be predicted as a function of applied pressure from sophisticated interatomic potentials calculations and first-principles based atomistic simulations.

The goal of the thesis is to develop and implement a testing procedure that experimentally determines pressure-dependent dislocation mobilities in oriented single crystals of the BCC transition metals. These experiments provide calibration data for models of materials subjected to extreme pressures and assist in model validation such as the Steinberg-Guinan hardening model or discrete dislocation dynamics simulations.

An experimental procedure is reported to perform shear tests on specimens held under moderately high hydrostatic pressures (on the order of 10 GPa). A thin foil of

polycrystalline Ta was used to perform experiments under hydrostatic pressures ranging from 2.1 to 4.2 GPa. A change in texture due to accumulation of slip was observed. Close to a strain of 1, the texture is predicted to change from {111} + {100} to{101}+{121}+{123}, the primary and secondary slip planes in BCC. These {101}+{121}+{123} textures were present in all the samples subjected to pressures greater than the threshold pressure to have internal shearing. The experimental (TEM) evidence shows different microstructures with the pressure being the only variable. At low pressures (2 GPa), an expected microstructure containing only dislocations was found to be responsible for the plastic deformation. At higher pressures (4 GPa) the dislocations appear to arrange themselves into elongated cell walls, with widths of 50-100 nm and lengths close to a micron.

Testing on Mo single crystals were carried out. Two different orientations {110}<111> and {121}<111> were tested such that simple shear deformation was achieved by single slip on a single slip system with no additional slip activity. The experiments provided data on the shear-stress – shear strain behavior of the single crystals as a function of pressure, giving an indication of dislocation mobility on the given slip system.

In all the cases, yielding and hardening behavior were observed to be sensitive to the imposed pressure. The values obtained experimentally are considerably higher than those predicted by the models based on a linear pressure-dependent shear modulus G(P).

TABLE OF CONTENTS

LIST OF TABLES

LIST OF FIGURES

Chapter 1
Introduction

The study of material strength under ultrahigh pressures is an important subject due to the fact that almost all the knowledge we have of the materials comes from tests carried out at ambient pressure [1]. Of particular interest in the present work is material behavior at moderately high pressures. Properties such as hardening and ductility of metals are sensitive to high pressures, even at relatively low pressures 0.7-3.0 GPa. A remarkable increase in ductility of some materials has been reported at high pressure [2-3]. Such is the case with tungsten, which is brittle at atmospheric pressure but can achieve elongations as high as 100% when subjected to a pressure of 2.8 GPa [5].

Modeling the constitutive behavior of materials subjected to such pressures requires an understanding of the pressure-dependent dislocation core structure and associated properties. The structure can be predicted using sophisticated interatomic potentials and first-principles based atomistic simulations [6-13]. Pressure and structure dependent dislocation mobilities are an important output from these models that can be fed into calculations based upon dislocation dynamics and crystal plasticity.

Dislocation dynamics based models have recently been successful in predicting dislocation structure evolution in small volumes of material [14-20]. Larger scale models describing the response of structural members to extreme loading conditions must incorporate information from the smaller length scales to accurately predict material behavior.

Dislocation mobilities are important for deformation models at several length scales, and are explicitly required in dislocation dynamics. The measured pressure-dependent dislocation mobilities and accompanying structure characterization could also provide valuable information to those involved in modeling interatomic potentials, dislocation core structures, and dislocation mobilities.

Outline & Objectives of the Current Research

The current research presents an approach to determine pressure dependent mechanical behavior of BCC metals, specifically Tantalum The high-pressure deformation experiments were done using a modified Bridgman cell [21-29], this was designed and constructed at LLNL and adapted to our facilities. The deformations were performed over a range of pressures from 1 GPa to approximately 4.5 GPa. The experiments provided data on the stress-strain behavior of the thin foil specimens as a function of pressure, giving an indication of how the flow stress and hardening is enhanced by subjecting the material to high pressure.

Following is the outline of the current research

- Chapter 1 gives background on the materials used and the expected or predicted dependence of mechanical properties with pressure. This is done by providing previous experimental and modeling work.
- Chapter 2 illustrates both the experimental techniques that were used to characterize the specimens used in this investigation, and the modeling tools that

were used to explain the mechanical behavior of materials. The experimental techniques include Vickers microhardness, Scanning Electron Microscopy (SEM): in particular Electron Backscatter Diffraction (EBSD) and Transmission Electron Microscopy (TEM). The modeling techniques include the Visco-Plastic Self-Consistent (VPSC) model and Discrete Dislocation Dynamics (DD).

- In Chapter 3 is given all the experimental details of the device that was designed and constructed for this study. Along with all the modifications that were implemented to reach an optimum operation for imposing hydrostatic pressure on thin foil specimens.
- Chapters 4 describes the effect of high pressure on the mechanical behavior of tantalum, the modeling that was done in order to explain that behavior and the characterization done dislocation structure on the precipitation
- Chapter 5 describes the preliminary tests performed on Mo single crystals
- Chapter 6 explains the contributions of the current research and its significance.
- Chapter 7 gives the main conclusions of the current dissertation.
- Chapter 8 provides suggestions for future work, both experimental and modeling efforts that should be pursued .

1.1 General Background

Background on the materials used, the expected or predicted dependence of mechanical properties with pressure, and finally, previous experimental and modeling work is presented in this section. Some specific details will be extended during the development of the thesis.

1.1.1 BCC materials

A unit cell is depicted in Figure 1.1.

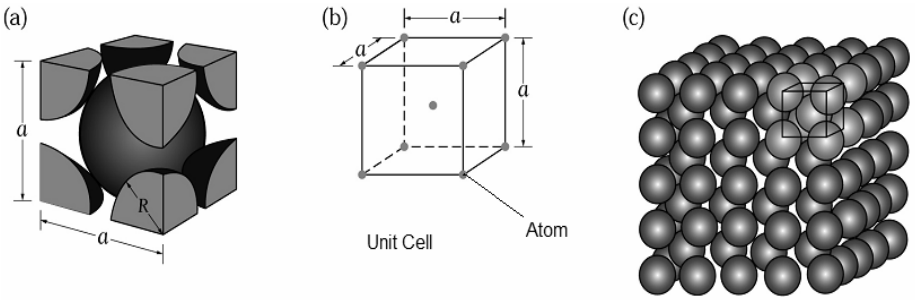

Figure 1.1 Atomic features of the BCC metals.[website]

The refractory BCC metals have high melting points and moduli. Many of their applications are specialized and exploit these properties. For example: tungsten lamp filaments operate at up to 2800°C, and molybdenum furnace windings to 2000°C. They are extensively used as alloying elements in steels and in super alloys, raising not only the yield and creep strengths, but also the moduli.

Schmid's law states that dislocation glide on a given slip system, defined by the slip plane and the direction of slip, starts when the magnitude of the resolved shear stress on that system reaches a constant critical value (CRSS). Implicitly this assumes that

components of the stress tensor other than shear resolved in the slip plane in the slip direction do not play any role in the deformation process. Furthermore, the critical stress must be independent of the sense of shear.

These assumptions are generally valid in metals with close-packed crystal structures for which Schmid's law was originally established. In contrast, BCC metals clearly deviate from the Schmid law. This is usually an indication that dislocation core effects are important. It was noted by many authors [7-8, 29-32] that the screw dislocation core plays an important role in the mechanical behavior of the BCC materials. A further explanation is given in the modeling background in this Chapter.

The yield stress of some BCC metals decreases as the metal is made more pure. There is debate as to whether the Peierls stress results from an intrinsic lattice resistance or from small concentrations of interstitial impurities. The question does not concern us here, except that it must be recognized that the yield parameters refer to a particular level of purity.

Table 1.1 records the properties for the case of polycrystalline Mo and Ta. The critical resolved shear stress of BCC single crystals is related to the polycrystalline shear strength by the Taylor factor, $M_s = 1.67$ for randomly textured materials [33].

Table 1.1 Material properties		
	Molybdenum	Tantalum
Atomic volume, Ω [x10^{-29}m^3]	1.53	1.80
Burgers vector, b [nm]	0.273	0.286
Melting temperature, T_m [K]	2883	3271
Shear modulus of, G [GPa]	1.34	0.612
Density [gr/cm3]	10.28	16.65

1.1.2 Dislocation velocity and applied stress:

Before studying the effect of pressure it is good to know how the velocity of a dislocation depends on the measured stress. There are a number of constitutive relationships that describe dislocation velocity as a function of stress [34-41]. The function that has been usually employed to express the empirical relationship between dislocation velocity and applied shear stress is:

$$v = v_o \left(\frac{\tau}{\tau_o} \right)^m \tag{1.1}$$

where v_o , τ_o are usually taken as 1 cm/sec and the required stress to give the dislocation this velocity, and m is a hardening exponent. It is commonly accepted that there is a limiting velocity for the dislocation movement and it has been found that this velocity is the velocity of sound in a given material.

A classic work in the late fifties by Gillman and Johnston [35] working on LiF, shows that there is a tendency for the dislocation velocity value to asymptotically approach the velocity of sound as the applied shear stress increases to an infinite value.

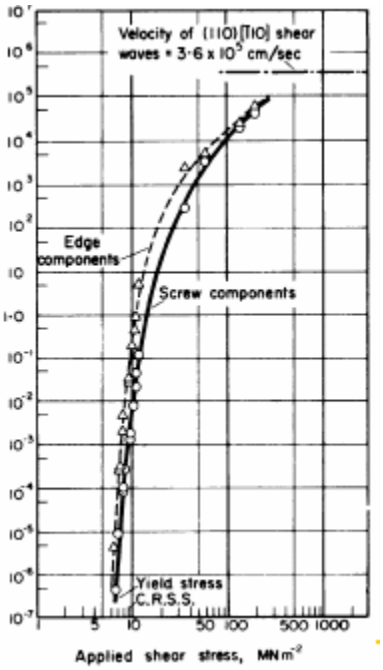

Figure 1.2 Stress dependence of dislocation velocity in LiF [16]

Despite the experimental validation of Equation 1.1, it fails in the sense that it does not point to a limiting velocity of the dislocation as the applied stress goes to infinity. Gillman [36] proposed that the velocity of the dislocation be expressed in the form:

$$v = v^* e^{-A/\tau} \tag{1.2}$$

where again A and v^* are determined experimentally. So at an infinite value for τ the velocity of the dislocation will be the limiting velocity v^*, the velocity of sound in this medium.

Dorn, Mitchell and Hansen [42] have suggested that there are stresses at which the dislocations do not move, so the stress should be made up of an athermal

contribution τ_A, and the applied stress τ. Then the velocity should be related to stress in the form $\tau^* = \tau - \tau_A$ and not τ alone. Another modification has been made to this model and applied to polycrystalline material. There is an inclusion of a hardening term that should be included to correct the curves after the yield point, so Equation 1.1 is modified to be:

$$v = v_o \left(\frac{\tau - c\varepsilon_p}{\tau_o} \right)^m \tag{1.3}$$

where ε_p is the plastic strain and c is the macroscopic work hardening coefficient.

In a work by H. Conrad and H. Prekel [39-40], on molybdenum single crystals, they demonstrate that the dislocation velocities, measured by the etch pitching technique followed Equation 1.1. By using this technique the velocity is calculated by measuring the farthest distance traveled by the dislocation divided by the time of loading.

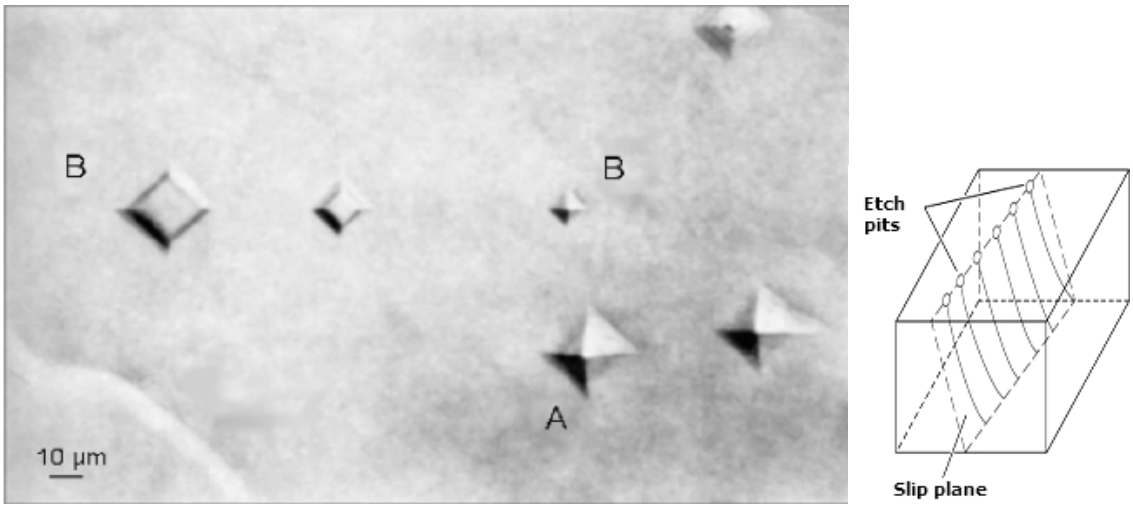

Figure 1.3 The movement of dislocations in LiF. B under two subsequent stress pulses is indicated by the pits, A did not move, [27]

The results presented in Figure 1.4 show that Molybdenum obeys Equation 1.1 at least over the ranges of applied stress in the experiment.

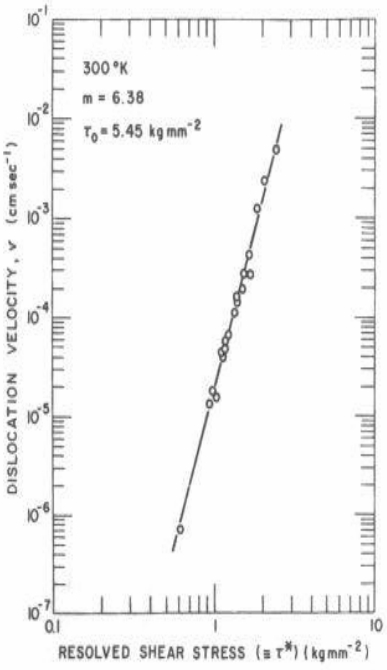

Figure 1.4 Stress dependence of dislocation velocity in Mo at room temperature. [39].

It should be noted that this model does not relate dislocation mobility to deviatoric stress components other than τ and hydrostatic pressure.

1.2 Experimental background

This section contains the work done hitherto in the field of experimental mechanics at high pressure. A review is given where the medium used was a fluid either liquid or gas, followed by a subsection of the work by Bridgman, whose work inspired this effort.

1.2.1 Review of high pressure experiments

There are several media that have been used to impose hydrostatic pressure, these include the three main states of matter: solids, liquids, and gases [43-45]. Figure 1.5

shows the schematic of one of the vessels used for deformation while maintaining the pressure for levels up to 3 GPa. As depicted in Figure 1.5, the pressure is reach by compressing the fluid in the vessel via pressing a plunger into the bore of the pressure vessel.

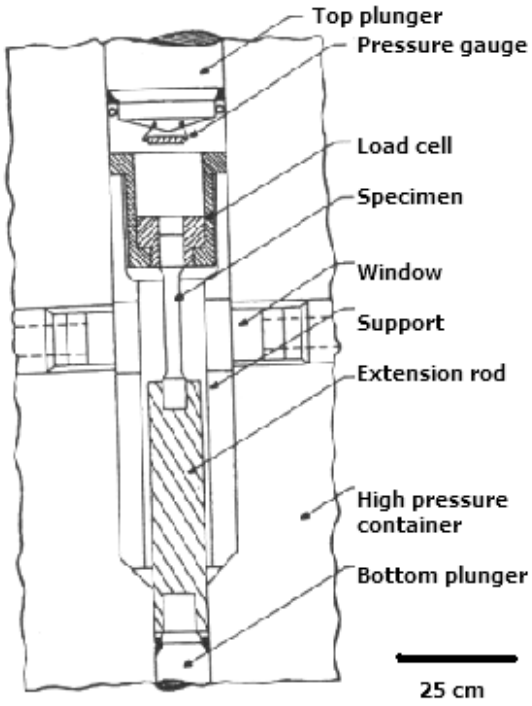

Figure 1.5 Schematic of an apparatus to achieve high pressure using oil as medium.[44]

The pressure is monitored by manganin coil pressure gauges. This kind of coil has a good linear and reproducible response of the resistance against the superimposed pressure that makes them suitable for this task.

Typically, the pressurization and depressurization rates are kept with a low constant value in order to eliminate thermodynamic effects such as cooling or heating of the sample before the deformation process.

Once the pressure is reached, it is kept constant by using an intensifier or retracting the bottom hydraulic piston while the top plunger is being inserted. Having the

desired pressure level maintained, the tensile or compressive deformation process is achieved by operating the assembly train containing the specimen. The strain or displacement of the specimen is measured either by monitoring the piston displacement or in more recent studies [47-48] using pressure compensated strain gauges attached to the specimen surface.

One example of the gas-based system is depicted in Figure 1.6. In this device, the pressure is attained by using a pressure intensifier contained in the multi-walled pressure vessel. The gas present at high pressure is kept at low volume because of the danger associated with stored energy and a possible catastrophic failure of the pressure vessel.

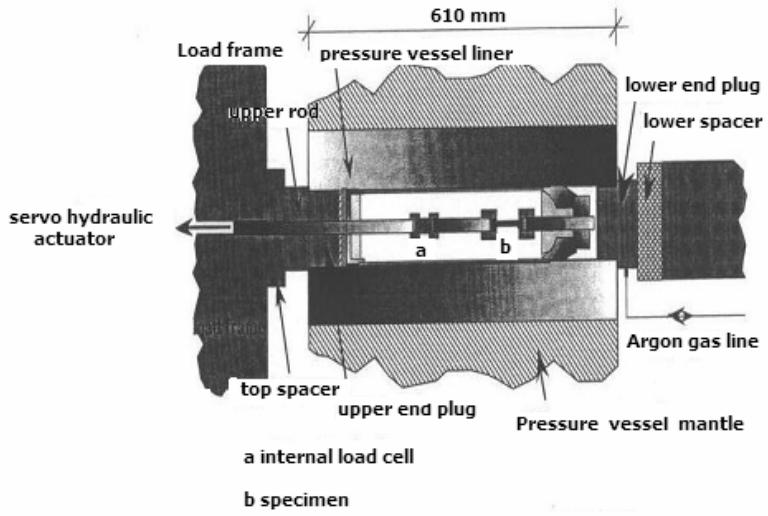

Figure 1.6 Schematic of an apparatus to achieve high pressure using Ar as medium.[38]

These kinds of apparatuses work the same way as the systems based in oil reservoirs with similar diagnostic features as those depicted in Figure 1.6. Pressure fluctuations in gas systems are generally less than those with oil systems, because the device that exerts the pressure is usually connected with the feature controlling the displacement of the specimen.

It is important to note that in most cases where the test was conducted at high pressure, the specimen was coated or jacketed with some impermeable membrane in order to eliminate the contamination as result of the penetration of the fluid media into surface cracks or porosity in the specimen. This coating membrane is very thin and does not affect the actual response of the specimen to the imposed loading conditions.

For higher pressures, in excess of 3 GPa, the common apparatus used is the diamond anvil cell (DAC). To achieve these pressures, experiments have been conducted using the diamond anvil cell, (Figure 1.7) [48-50], where the specimen is loaded to high-pressures between the diamond anvils. Although this device allows ultrahigh pressures to be reached readily, it has the deficiency that the hydrostatic, frictional and deviatoric stresses increase in an uncontrolled manner as the load increases [51].

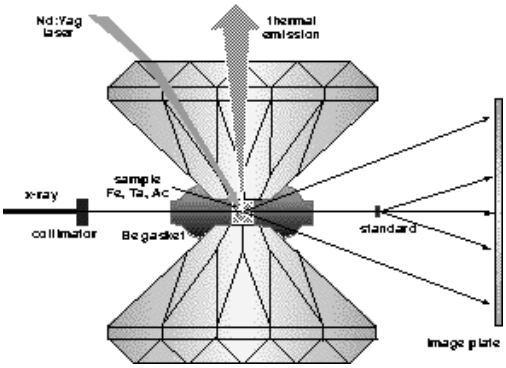

Figure 1.7 - Schematic of the diamond anvil cell (DAC), the sample is pressed between the anvils and an x-ray source is used to study the materials during the process [51].

Typically the volume of material tested in these kinds of systems is small and properties that are observed are sometimes a function of the sample size. Postmortem analysis in these types of experiments is often difficult or impossible because of the sample size. One goal of our experiment is to perform high-pressure experiments using a

larger specimen size that can be analyzed using standard characterization tools subsequent to testing.

Finally, extremely high pressures can be attained in shock loading experiments that use the impact of high velocity objects. These dynamic loading experiments are not treated in depth during the development of the thesis because our experiments were carried out under quasistatic conditions.

As it will be discussed in the following section, according to yielding J_2 and similar criteria [52-54] there should be no effect of the hydrostatic pressure, so the flow stress behavior should be the same at atmospheric as at any pressure. It has been observed that this is not the case. One simple exception can be that pressurization serves as a means of generating dislocations around inclusions or other defects, this is due to the existence of stresses that arise because of the differences in elastic-plastic properties between the matrix and second phase particles.

This section focuses on the results primarily from the experiments using liquid or gas media and modest temperatures from room temperature to a maximum of 300 ºC.

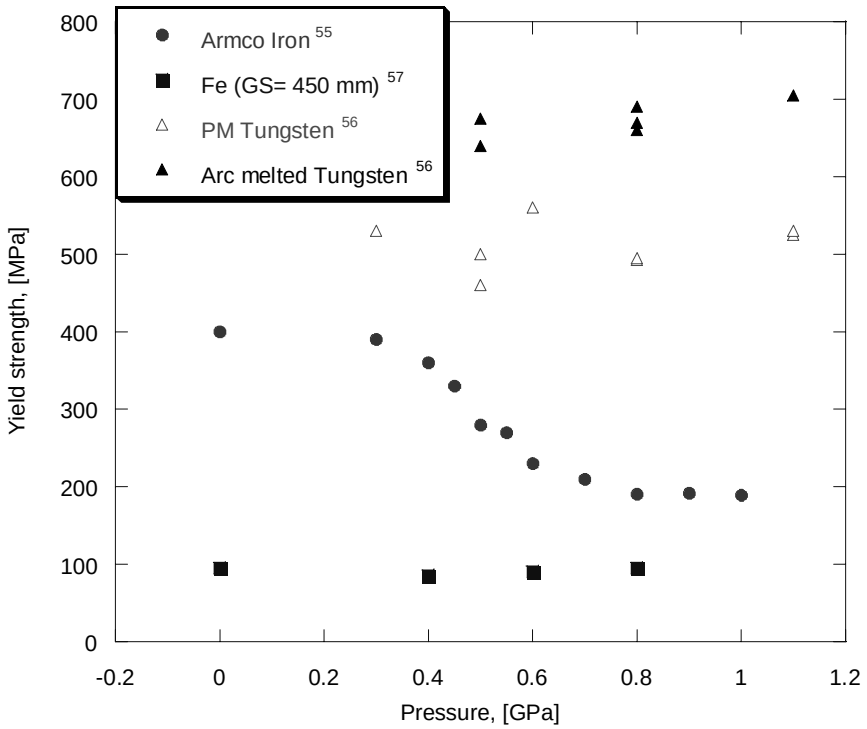

Figure 1.8 Effect of hydrostatic pressure on some BCC materials

Figure 1.8 summarizes the results of different authors [55-57] on the reported behavior of flow stress of BCC materials under superimposed pressure. The measurements of yield were done during tensile deformations under hydrostatic pressures. The pressure was exerted either by oil or Ar gas media. Both Fe and W exhibit changes in yielding as a function of pressure.

It has been observed [36] that the imposed hydrostatic pressure significantly inhibits the dislocation mobility in ionic materials such as LiF, and therefore there is an increase in the flow stress above that obtained at atmospheric pressure. TEM analyses of these kinds of materials reveal that dislocation generation was present near non-metallic inclusions and other inhomogeneities in the material, and hence these mobile pressure induced dislocations reduced the yield stress. In some cases, if the pressure was high

enough, it generated an excess of dislocation density and consequently an increase in the yield strength because of hardening due to dislocation interaction.

Some experimental results show the effect of pressure on the hardening exponent, n. In tests carried out under uniaxial tension or in plane strain tension specimens for some high strength aluminum alloys (7075-T651) [58,59], it was generally revealed that *n* increases with increasing pressure.

One of the most interesting changes in properties is the enhancement of ductility of BCC materials under imposed pressure. This change in properties allows the study of mechanical properties on this kind of materials not possible on normal conditions because of the high degree of brittleness. This enhancement has been related to the constriction of micro-voids responsible for cracks, or as a means of enhancing the dislocation density near inclusions in the matrix.

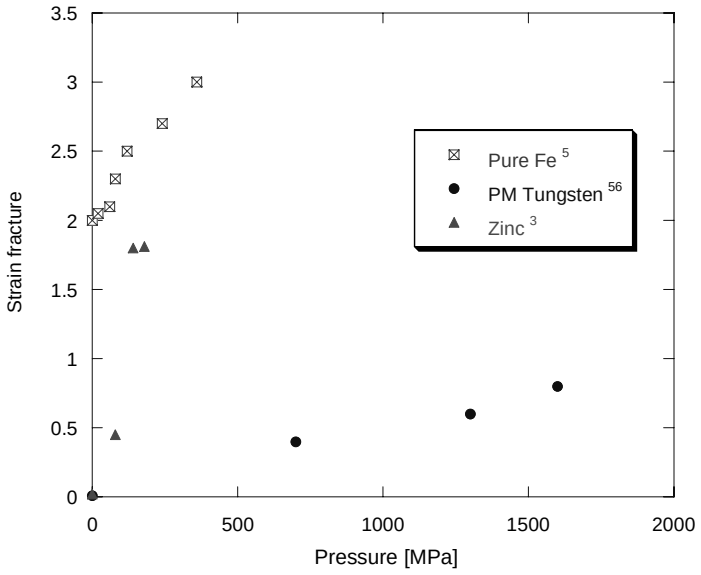

Figure 1.9 Enhancement of the ductility on materials with bcc structure.

As depicted in Figure 1.9 the ductility is enhanced as much as 80 times, in the case of iron and other brittle materials such as tungsten, magnesium, and zinc [5,56,3].

The work presented so far was done in oil and gas environment, the following section presents a work by using solid as the medium of applying the pressure.

1.2.2 Bridgman work

The Bridgman technique for studying the behavior of materials under hydrostatic pressure has a long history [21-29]. The present work was based on, and compared to, his results. Bridgman's work was the threshold to high-pressure experiments. However his research was done during the discovery of the dislocations era and therefore his explanations lie more in the qualitative description of the results more than in a physical interpretation.

For the experiments designed in the current research, two major features were desired; strict control in the loading path, in order to separate the effects of hydrostatic and deviatoric stresses, and the ability to perform post-mortem characterization such as hardness measurements and TEM analysis. To accomplish these goals a modified Bridgman cell was developed. Of the various types of anvils developed by Bridgman for high-pressure work, the one developed for applying a shearing load on specimens under high pressure came the closest to achieving the desired test objectives. Details will be given in the experimental section.

If the material follows the von Mises equation [54], the stress should not be greater than a certain value given by the Equation 1.4

$$(\sigma_x - \sigma_y)^2 + (\sigma_y - \sigma_z)^2 + (\sigma_z - \sigma_x)^2 = const. \qquad (1.4)$$

where σ_x, σ_y, and σ_z represent the principal stresses in the cartesian system.

This will lead to the result of the tangential force necessary to produce shearing of one plane on another and is independent of the normal stresses as depicted in the Figure 1.10

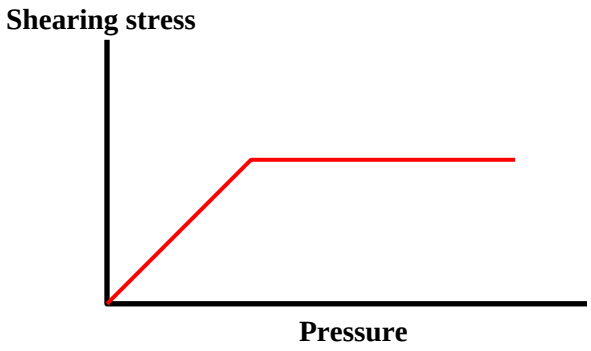

Figure 1.10 Ideal behavior of the material exhibiting pressure independence of the shear strength [22]

When the specimen starts to flow, the rotating force assumes a constant value, independent of the normal pressure, and the curve consists of two straight lines. This condition seems to be satisfied under the practice in the engineering range on ordinary materials, but it deviates under extreme conditions. The most common type of curve found experimentally by Bridgman is shown next in Figure 1.11.

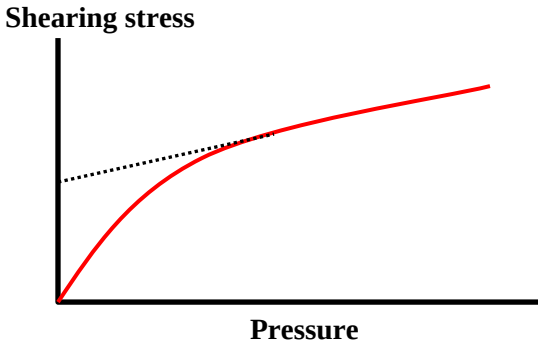

Figure 1.11 Typical, experimental behavior of the material exhibiting pressure dependence of the shear strength [22]

The transition from the initial stage of surface slip to the final stage of internal flow is marked by a knee in the curve, after this point the curve usually rises distinctly less rapidly than in the initial stages and usually with concavity toward the pressure axis. For the average substance, the knee occurs very roughly in the neighborhood of 1.9 GPa. Beyond the knee point the curve describes the conditions inside the metal rather than the conditions in the surface. A rough extrapolation can be made to indicate the internal conditions in the pressure range under the knee.

In Bridgman's work, a pressure of 50000 kg/cm^2 (5 GPa) was easily attainable using parts made out of hardened steel. Later studies with blocks made out of carboloy allowed him to reach double that of the original pressures.

In the cases of Ta and Mo Bridgman [22-23,25] found that the shearing was perfectly smooth. Correlation can be implied between the smoothness and the number of slip systems in the crystal. This is in agreement with the fact that for the BCC materials, there are 48 possible slip systems and therefore any of them could be the via for easy glide in the sense of the torque applied force. Table 1.2 summarizes the results found by Bridgman for the case of Mo and Ta.

Table 1.2
Bridgman Results

	Molybdenum	**Tantalum**
Pressure [GPa]	Shear strength [MPa]	Shear strength [MPa]
0.98	58.8	360
1.96	235.2	740
2.94	509.6	870
3.92	803.6	1040
4.9	1185.8	1150

There are many other types of curves than that shown in Figure 1.11, but by far it was the most common, and representative of Ta and Mo, the two metals studied in this research. Some of Bridgman results for Ta and Mo are depicted in the Figure 1.12.

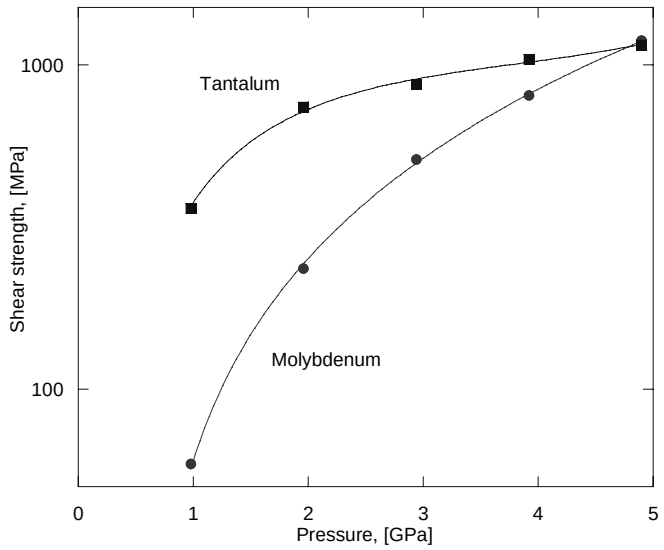

Figure 1.12 Experimental behavior of Mo and Ta exhibiting pressure dependence of the shear strength. [22,25]

Although the data are sparse because of the difficulty of conducting the experiments, both Mo and Ta were found to exhibit significant increase in shear strength at relatively modest high pressures, up to 5 GPa, even with the limited stress measurement capabilities of the time. Figure 1.12 shows a marked variation of shearing strength with pressure for these two materials, which indicates an evident deviation from the idealized plasticity model that states that the shearing strength is independent of normal stresses.

1.3 Modeling Background

In order to understand the underlying mechanisms responsible for the mechanical behavior and its dependence upon high pressure, it is necessary to investigate all the possible mechanisms occurring at the different size scales, Figure 1.13 shows the Multiscale Model that contains all the different scales that may give an explanation to the experimental results.

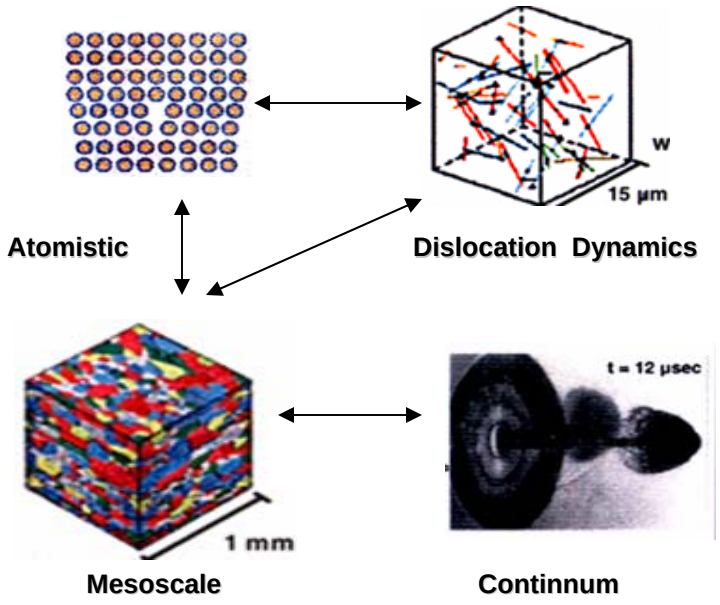

Figure 1.13 *Multiscale model [51]*

In the following sections is presented a background on the different approaches to study the mechanical behavior of metals, all of them were explored in a large or lesser degree during this investigation. The order in which the background on each regime is presented resembles the order that they were surveyed during the course of this investigation.

1.3.1 Continuum approach: Criteria for yielding

1.3.1.1: Tresca and von Mises criteria

There are two continuum criteria on yielding of metals. The Tresca [52] or Coulomb [53] criterion establishes that yielding will occur when the maximum shear stress reaches a critical value equal to the shear stress in tension:

$$\tau = \frac{\sigma_1 - \sigma_3}{2} = \frac{\sigma_y}{2} \tag{1.5}$$

σ_1 and σ_3 are the largest and smallest principal stress, and σ_y is the uniaxial yield stress.

To study the effect of pressure, we assume that a state of uniaxial stress exists:

$$\begin{aligned} \sigma_1 &= \sigma - P \\ \sigma_2 &= -P \\ \sigma_3 &= -P \end{aligned} \tag{1.6}$$

where σ is the stress in tension and P is the pressure. Simple calculation of $\sigma_1 - \sigma_3$ leads to independence with respect to pressure, so the yield stress should remain constant without any effect of the pressure.

Following now the Maxwell-von Mises criterion [54], a model based on shear strain energy, it predicts that yielding occurs when the second deviatoric invariant J_2 reaches a critical value. The invariant J_2 is defined as

$$J_2 = \frac{1}{6}\left[(\sigma_1 - \sigma_2)^2 + (\sigma_2 - \sigma_3)^2 + (\sigma_3 - \sigma_1)^2\right] \tag{1.7}$$

where σ_1, σ_2, and σ_3 represent the principal stresses. Assuming the same conditions of testing and substituting the values from Equation 1.1, it is easily found that $J_2 = \frac{1}{6}\sigma^2$.

The yield stress is again independent of pressure using this criterion and therefore the yield stress should remain constant with pressure. So the effect of hydrostatic pressure is predicted to not be responsible for changes in yield stress following these two criteria.

In a more recent work by Steinberg and Guinan, it is found that, contrary to the predictions by Tresca and von Mises, the pressure affects the shear modulus of the material and subsequently the yield stress. Details are described in the next section.

1.3.1.2 Steinberg-Guinan Model

The Steinberg-Guinan model was initially developed for high strain rate tests [60, 61] but then modified [62] to make it suitable to lower strain rates. This model is applicable for estimating the yield strength as function of plastic strain, pressure and internal energy (temperature).

It is known that in one modification of the von Mises model, the yield stress (Y) is affected by the plastic strain, the well-known hardening effect. With this phenomenon the yield stress and the shear modulus (G) are affected by other parameters such as pressure, temperature and strain rate.

The Steinberg-Guinan model relies on the assumption of independence of the strain rate, so this theory should be taken as a guide and proper modifications should be

expected. There is sufficient evidence that the shear modulus increases with increasing pressure, but it is not the same as the yield stress. If independence of strain rate is assumed, it is expected that Y will be proportional to G. Although the experiments reveal that Y tends to increase more rapidly than the shear modulus with varying pressure, the increments in the two of them are proportional yielding the relation in Equation 1.8:

$$\frac{1}{Y_0}\frac{dY}{dP}\Big)_0 \approx \frac{1}{G_0}\frac{dG}{dP}\Big)_0 \tag{1.8}$$

It can be concluded that as the shear modulus increases with pressure so does the yield stress.

The constitutive equations for both the shear modulus and yield strength, again assuming rate independence are found to be:

$$G = G_0\left[1+\left(\frac{G_P'}{G_0}\right)\frac{P}{\eta^{1/3}}\right] \tag{1.9}$$

and

$$Y = Y_0 * \left[1+\beta(\varepsilon_i+\varepsilon)\right]^n * \left[1+\left(\frac{Y_P'}{Y_0}\right)\frac{P}{\eta^{1/3}}\right] \tag{1.10}$$

where η is the compressibility of the material defined as the initial volume v_0 and divided by the specific volume v; P is the pressure, G the shear modulus, Y is yield strength, β and n are work hardening parameters and ε is the strain. The subscript $_0$ refers to reference values (T= 300 K, P=0, ε=0), and the primed parameters are the partial derivative with respect to the parameter indicated. Because the experiment was conducted at room temperature, the terms corresponding to temperature dependence were neglected.

The model establishes the limitation of a maximum yield stress in the form:

$$Y = Y_0 * \left[1 + \beta\left(\varepsilon_i + \varepsilon\right)\right]^n \leq Y_{\max} \tag{1.11}$$

At low pressures, experiments show that G varies linearly with P. At ultrahigh pressures the Thomas-Fermi [63] theory predicts that P is proportional to $\eta^{5/3}$ and G to $\eta^{4/3}$. This is in agreement with Equation 1.9. If $P \to 0$ and $\eta \to 1$ then $G = G_0 + G_P' P$, and also if $\eta \to \infty$, then G varies in the form of $\eta^{4/3}$.

In addition to this simple verification, the authors compared the validation of Equation 1.8 comparing the pressure-dependent parts with Thomas-Fermi calculations at ultra high pressures. It was found that Equation 1.9 predicts G within a factor close to 2 with that calculated from Thomas-Fermi values. Therefore G will not become unreasonably large at high pressure, giving a limiting behavior to this property, as one should expect. To allow that Y can increase more rapidly than G, the pressure coefficients can be set individually, also if Y_p/Y_o increases faster than G_p/G_o, Y is still bound to a value $G/10$, so in this case Y cannot be unphysically large. Therefore Equation 1.8 seems to be a good representation of the pressure dependence.

The present study follows the procedure to maintain the same strain rate and vary the pressure. Once again it must be recognized that the yield parameters and shear modulus refer to a particular strain rate. It was found experimentally that both Ta and Mo have indeed dependence with the pressure. This high pressure related increase in the yield stress phenomenon has been studied in other works and is presented in the following section.

1.3.2 Atomistic approach

It is widely accepted that the deformation in BCC materials is mainly governed by dislocations with screw character. Different studies have shown that the mobility ratio of edge-to-screw is as much as 40 [64]. So in the initial stages of plastic deformation all the edge components are driven out of the sample and the slow screw dislocations are left to control the deformation. This phenomenon has been confirmed by TEM analysis on Mo after a strain of 1% (see Figure 4.4a), and by in situ straining of a Mo film (Figure 1.14b).

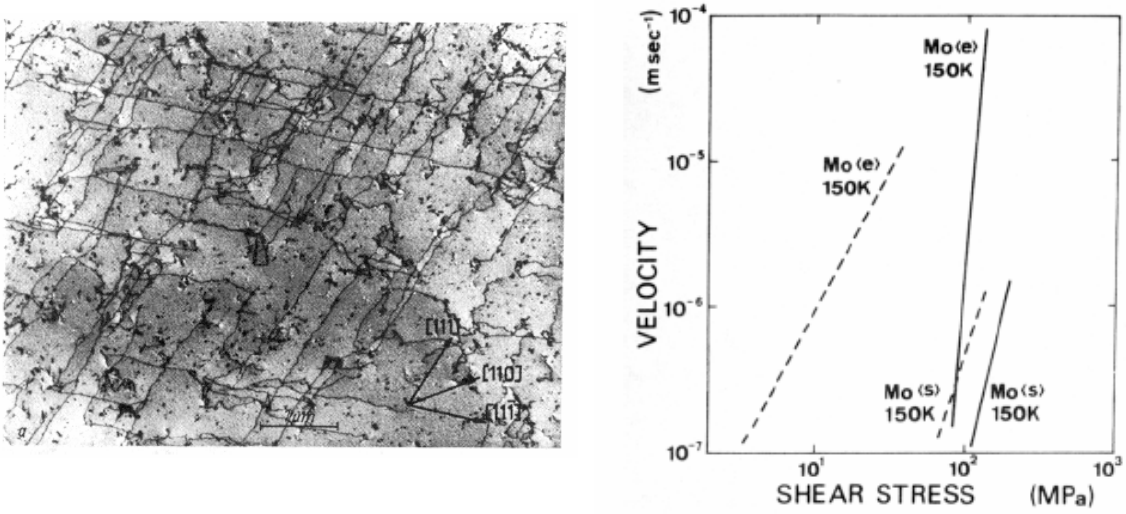

Figure 1.14 (a) Dislocation microstructure in Mo under 2% tensile strain along [110] at 77K[65] (b) Velocity of edge (e) and screw (s) dislocations in Mo as a function of stress by in situ high voltage electron microscopy [66].

One of the reasons for such difference in mobility is their different atomic arrangement at the core of the dislocation. The detailed structure of screw dislocation core in BCC metals has been examined through atomistic simulations [67-71]. Most of the calculations predict a polarized core structure, this is in accordance with HREM experiments [72]. Polarization is a significant issue since the details of the atomic

rearrangement in the core are thought to have an effect on the lattice resistance to dislocation motion. Specifically it has been thought that the high Peierls stress of the screw dislocation is a direct consequence of its non-planar core structure. In the context of this thesis is important to establish how the pressure can affect the core polarization and therefore the increase in the Peierls stress. Any change in these properties could be associated with the experimental observation of pressure dependent flow stress. Details are given in the next sections.

1.3.2.1 Core structure

A study by Soderling and Moriarty [8,10] investigates the behavior of the *a*/2 <111> screw dislocation core at different pressure conditions. As they showed and the results are reproduced in Figure 4.4, the internal details of the core structure have strong pressure dependence. These details can be related to the degree of polarization of the core. In general, the two energetically equivalent configurations of the degenerate core display a broken two-fold <110> symmetry. The physical origin of this broken symmetry is a translation, parallel to the dislocation line but in opposite sense for the two different core orientations, of the three central atoms nearest to the core center , as it is depicted in Figure 1.15.

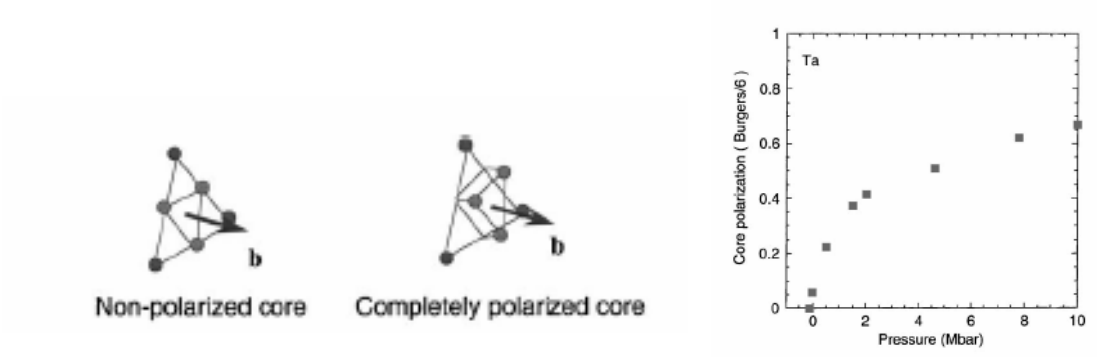

Figure 1.15 Polarization of the dislocation core as function of pressure.[8]

This property, termed the polarity (or polarization) of the dislocation core [8] can be used to quantitatively analyze the pressure-dependent screw dislocation core properties. By symmetry, the polarization vector p can only vary uniquely from $-b/6$ to $+b/6$.

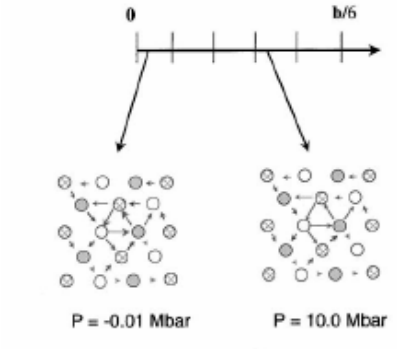

Figure 1.16 Polarization of the dislocation core as function of pressure [8]

At $p = 0$, the two core configurations coincide and a fully symmetric core structure is formed with a higher six-fold symmetry. At $p = \pm b/6$, on the other hand, a completely polarized core is obtained with maximum three-fold spread out along <121> directions.

Under compression, the polarization of the core is predicted to increase. Figure 4.5(b) shows the variation of core polarization as a function of pressure up to 10 Mbar for bcc Ta. This result clearly shows that the magnitude of polarization increases rapidly below 2 Mbar (200GPa). It then increases more gradually above 2 Mbar and reaches a value of 0.12*b* at very high-pressure near 10 Mbar.

1.3.2.2 Peierls Stress

One of the most common factors considered to influence the dislocation mobility is the stress needed to overcome the Peierls force. The motion of the dislocations is driven by an applied resolved shear stress and is hindered by the lattice resistance, which is weak enough that it may be overcome by thermal activation [13,73-74]. The lattice resistance is presumed to be described by a Peierls energy function, which assigns an energy per unit length to dislocation segments as a function of their position on the slip plane.

In BCC crystals, as explained in the previous section, the core of screw dislocation segments relaxes into low-energy non-planar configurations [8,10]. This introduces deep valleys into the Peierls energy function aligned with the Burgers vector directions possessing the periodicity of the lattice as shown in Figure 4.7.

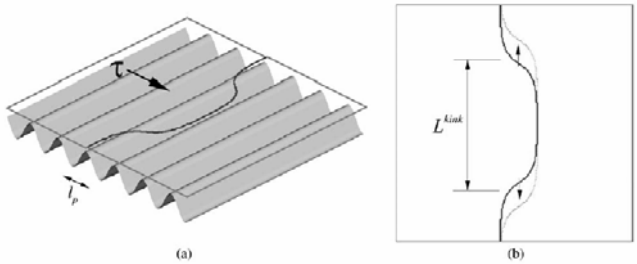

Figure 1.17 Schematic showing the Peierls stress barrier in the lattice. [6]

The energy barrier for the motion of screw segments, and the intrinsic Peierls stress, may be expected to be large, and the energy barrier for the motion of edge segments to be comparatively smaller. While it is generally accepted that the high Peierls barriers of the $a_0/2$ <111> screw dislocations are a consequence of the three-fold symmetry of the <111> axes in the BCC structure, the literature abounds in different and to a large extent conflicting proposals on how this is to be related to the flow stress.

This stress has been studied by atomistic simulations by Yang and Moriarty [8], it was shown that the Peierls stress increases as the shear modulus increases, almost in a linear way. The results are presented in Figure 1.18,

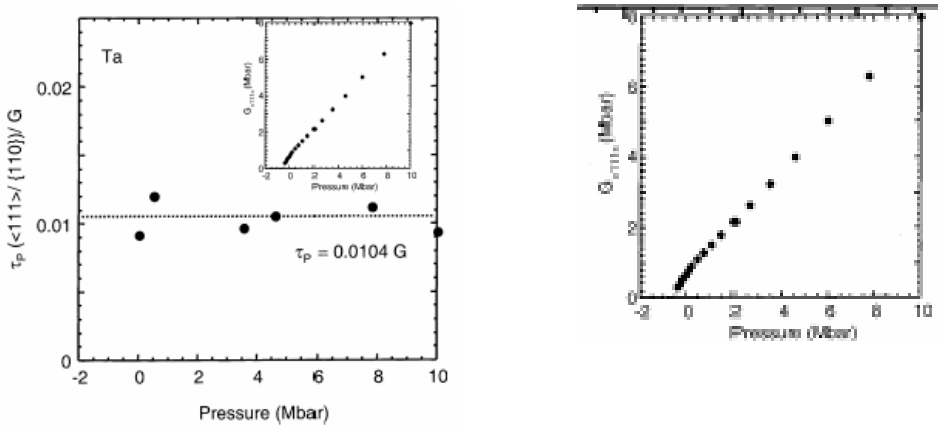

Figure1.18 Plot showing the linear dependence between the Peierls stress and the shear modulus [8],

In the classical manner the Peierls stress for screw dislocations is expressed by the following equation:

$$\tau_p = \frac{G}{1-\upsilon} e^{\left[\frac{2\pi a}{(1-\upsilon)b}\right]} \tag{4.3}$$

where G is the shear modulus, ν the Poisson's ratio, b burgers vector and a lattice parameter, all of them functions of pressure. If the approximation of the Steinberg model is used, the increment of the Peierls stress will escalate linearly with the shear modulus and therefore would be close to 3 % .

1.3.2.3 Pressure effect: Dislocation motion vs. twinning

The last phenomenon to be included here is the discussion of which is the preferred mechanism of plastic deformation under pressure from the atomistic point of view. Dislocation glide and deformation twinning are the two major plastic deformation modes in metals. Their nucleation and multiplication/growth under stress govern the mechanical behavior of materials. Various models have been proposed for the nucleation of twins from dislocations [references], but direct experimental confirmation of these models are rare. There are several studies [75-76] where they simulated the nucleation and growth of deformation twins in BCC Mo using the Finnis–Sinclair empirical potential [77-79]. Shear deformations were carried out under hydrostatic tension and compression to determine the effects of pressure. Figure 1.19 shows the twinning shear directions corresponding to the BCC structure.

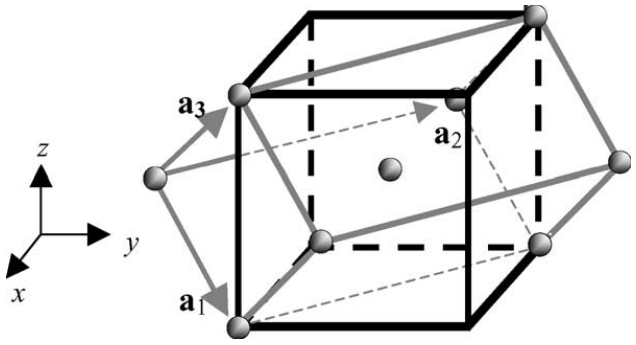

*Figure 1.19. Elementary cell with basis vectors **a**1, **a**2, **a**3 corresponding to vectors in the [1 1 .1], [.1 1 0] and [1 1 1] directions, respectively. The b.c.c.unit cell is delineated by the thick lines. Twinning shear is along −**a**1 direction on the **a**1 × **a**2 plane.[75]*

Simulation cells containing up to half million Mo atoms were employed in the calculations, with periodic boundary conditions in all three directions. Shear displacements were imposed along [1 1 1] directions on (1 1 2) planes; the confining pressure being adjusted by changing the lattice parameter. The effect of pressure on the shear strength is shown in Figure 1.20. The *x*-axis in this figure is the ratio of the simulation cell vector length to that under zero pressure, which is an indication of the confining pressure. The critical resolved shear stress (CRSS) for twinning shear on (1 1 2)[1 1 1] increased with pressure increase from *P*= −20 to 12 GPa. Hydrostatic tension decreased the shear strength and yield strain of lattice.

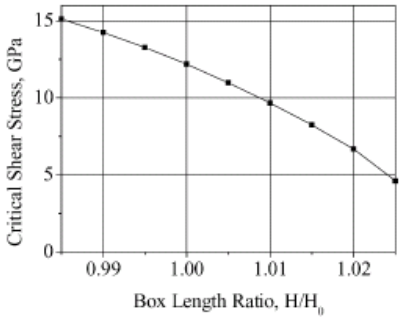

Figure 1.20 Pressure dependence of the ideal shear strength in (1 1 2)[1 1 1] (in the twining sense) at 1K.[75-76]

The increase of shear strength when the lattice was compressed can be understood as greater interactions when the atoms come into closer contact, thus making it more difficult for the crystal to deform.

The yield strain is also different, from 11 to 6% depending on the confining pressure, with smaller values when the system was in tension. When a large enough hydrostatic pressure (e.g., 10 GPa) was applied, shearing the crystal along (1 1 2)[-1 -1 1] in the twining sense did not create a deformation twin, but instead nucleated a dislocation loop of (0 1 1)[-1 -1 1] character, which has a positive Schmid factor with the applied shear stress. This is reported as homogenous dislocation nucleation.

This atomistic information on the dislocation core, Peierls stress can be used to construct mobility laws, which serve as inputs for the equation of motion in dislocation dynamics simulations.

1.3.3 Microscale (Dislocation realm):

Discussion of physical process governing the dislocation mobility

There are different approaches to study how dislocation dynamics is affected by hydrostatic pressure. Hydrostatic pressure constricts the dislocation movement, giving the materials a pressure-induced hardening effect, making it more difficult to deform the specimens with increasing pressure. It has been suggested that the magnitude of the resisting force arises from different contributions to movement of dislocations including the following factors

- Interaction with impurity atoms or precipitates
- Peierls stress

- Drag resulting from jogs
- Interaction with other dislocations
- Interaction with other lattice defects other than impurities

So the applied stress can be expressed as the sum of all contributions

$$\tau^* = \tau_{IA} + \tau_{PN} + \tau_{DI} + \tau_{JD} + \tau_{CL} \tag{4.4}$$

Experimentally it can be deduced which of these contributions dominate, by imposing conditions of temperature and impurity content allows a simplification of the process. While all the factors can contribute to control the dislocation mobility. The important question is whether they all contribute or if there is a predominant factor. Since the applied shear stress to attain certain strain increases as much as 100 % when we double the pressure, the controlling resisting factors should change in the same amount.

In the following discussion, the magnitude of possible pressure effects on each of these factors is considered in turn.

1.3.3.1 Temperature

This is the most studied of the factors of dislocation mobility in BCC metals. In general terms, the pronounced dependence of the flow stress of BCC metals on temperature, T, and plastic strain rate, ε_{pl} , below their *knee temperatures* T_K (about 0.2 of the melting temperatures; in Mo: T_K=500 K at ε_{pl}= 8.6×10−4 s^{-1}) is attributed to the need to overcome the exceptionally high Peierls barriers of $a_0/2<111>$ screw dislocations by

thermally activated formation of kink pairs and the subsequent kink migration along the dislocations (a_0=edge length of the elementary cube, in Mo a_0 = 0.315 nm)[80-81].

In the experiment reported in this thesis some rise in temperature could be present in the specimen due to friction during deformation but because the research was carried out at ambient temperature, the temperature effects were neglected (isothermal).

1.3.3.2 Impurities

Other possible controlling factors of the dislocation mobility could be the dragging or pinning effect of interactions with impurity atoms. It has been shown in many studies [82,83] that the impurity content has a large effect on the dislocation mobility at one atmosphere. There are three principal ways in which the impurities may interact with mobile dislocations. The first involves the possibility that pressure may cause impurities to segregate to dislocations. The impurities preferentially settle on a dislocation and therefore they must diffuse through the lattice, because of the well established large decrease in diffusion rate with pressure in crystalline materials, it is unlikely that the concentration of impurities would increase by diffusion with pressure. This is substantiated by the fact that the application of hydrostatic pressure affects the dynamic resistance of the lattice to dislocation mobility. The second involves the interaction of their strain fields as the dislocation moves through the lattice. The last possibility is for materials which have an ionic character, not the case for Mo. This involved the possible pinning of the dislocation due to charge on the impurity and the dislocation.

Impurity effect was not considered in the current experiments because all the testing was done on samples to a low impurity level (= 60 ppm).

1.3.3.3 Change in dislocation energies with pressure

The creation of a dislocation in a crystal produces a strain in the lattice. Such dilatation is expected to require more energy under a hydrostatic pressure than one atmosphere. In the case of screw dislocations there is no permanent dilatation of the lattice so no energy is necessary to create it. In the case of edge dislocations some of the energy is dissipated after the creation of the dislocation, and the remaining energy is stored in the form of elastic energy, i.e., a permanent elastic strain in the lattice.

It has been shown in other studies that the screw dislocation moves through the lattice due to the formation of double kinks in the dislocation line [84,85]. Studies via atomistic simulations [10,13-14] suggest that a straight screw dislocation in Mo moves by a double-kink mechanism, with a high double kink nucleation barrier (= 2 eV). In another study by Moriarty and Duesbery [30], static atomistic simulations also have found a small migration barrier for kinks on screw dislocations, suggesting that a screw dislocation with a pre-existing density of kinks would be highly mobile. These kinks are edge in character, *b* perpendicular to the dislocation line, as shown in Figure 4.15.

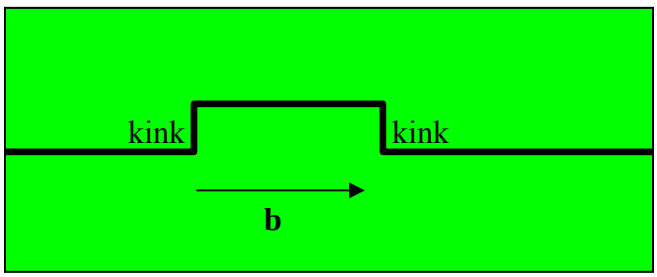

Figure 1.21 Schematic showing a double kink nucleation in the screw dislocation, causing strain in the lattice.

In these studies for the perfect screw dislocation the lowest kink-pair formation energy was found to be in good agreement with an empirical estimate based on the simulated low-temperature yield stress in Ta via dislocation dynamics [10,86]. Under an applied shear stress, the corresponding kink–kink interaction energy follows the expected λ^{-1} linear elastic behavior for separation λ larger than $7b$, while the applied stress varies as $\lambda^{-1.5}$.

Added to this it would be expected that to attain a given velocity at pressure, a higher applied stress would be needed because of the additional strain energy associated with these dislocation segments. In other words, the necessary increase in applied stress should be directly related to the increase in strain energy.

Keyes [87], using a strain energy model, derived several relationships describing the pressure dependence of the work needed to cause a dilatation in an elastic solid.
In this model the change in volume (V) for the work (W*) is related to:

$$\left(\frac{\partial V}{\partial W}\right)_{P,T} = \left(\frac{\partial \ln G}{\partial P}\right)_{T} - \chi_{T} \tag{4.5}$$

where G is the elastic shear modulus and χ_T is the isothermal compressibility

By identifying the change in volume with the activation volume of the dilatation, and the work with the additional energy needed to create the dislocation at pressure, it can be shown that

$$\left(\frac{\partial V}{\partial W}\right)_{P,T} = \left(\frac{\partial \ln W}{\partial P}\right)_{T}. \tag{4.6}$$

Combining Equations 4.5 and 4.6 we get:

$$\Delta \ln W = \left[\left(\frac{\partial \ln G}{\partial P}\right)_{T} - \chi_{T}\right]\Delta P \tag{4.7}$$

By inserting the value for isothermal compressibility and the largest value for the rate of change of shear modulus with pressure equation 4.7 reduces to

$$\Delta \ln W = 1.25 * 10^{-2}\, GPa^{-1}\, \Delta P \tag{4.8}$$

This relation would give the largest possible work done to create a dislocation at pressure. The ratio increase in energy is close to 1.03 at 2.1 GPa and at 4.2 GPa close to 1.05. Thus a maximum of about 5% of the increase in applied shear stress with pressure may be attributed to the increase in energy needed to create a dislocation at pressure.

1.3.3.4 Jogs

Another possible contribution to the change in dislocation mobility is a change in jog behavior. The jog is defined as a jump out of plane in the dislocation line. The burgers vector of a jog in a screw dislocation is perpendicular to the jog and therefore the jog is edge in character (see Figure 4.16).While the jog can glide along the core of the screw dislocation in the direction of its burgers vector, it cannot glide in the direction of the screw dislocation motion. If the screw dislocation moves and drags the jog along, the jog must move in a direction perpendicular to its burgers vector, as shown in Figure 4.16.

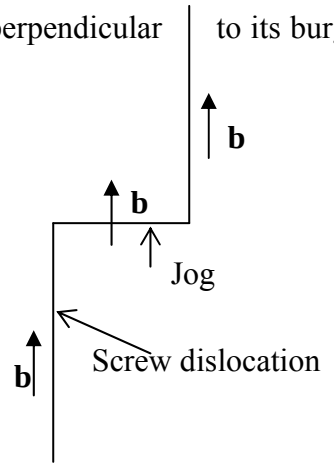

Figure 4.16 Jog on a screw dislocation.

This requires a non-conservative motion, as for example climb of a vacancy; this is illustrated in Figure 4.17.

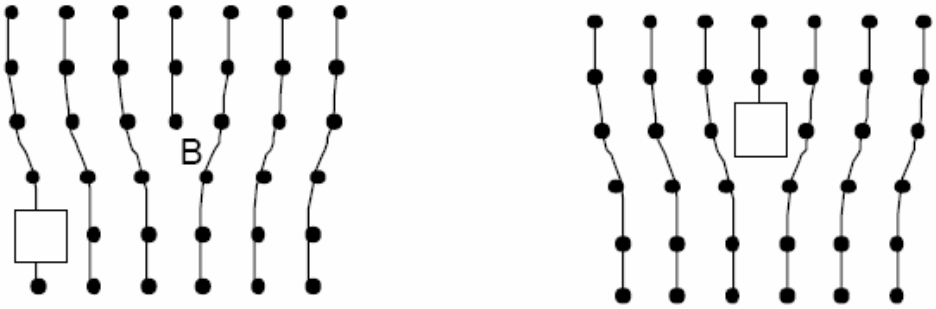

Figure 4.17 Schematic showing the diffusion of a vacancy to the core resulting in positive climb [37].

Positive climb can occur either by diffusion of previously existing vacancies to the core of the dislocation or the formation of an interstitial from the core and its subsequent diffusion away (Figure 4.17). Negative climb can occur with either a previously existing interstitial diffusing to the core or the formation of a vacancy adjacent to the core that diffuses away. The net result would be a trail of defects left in the wake of jogs situated on a moving screw dislocation.

Both of these processes are diffusion–related processes and as it was shown before the diffusion is found to decrease with pressure. In the work of Hanaffe [82] ,

where the effect of pressure on the dislocation mobility in polycrystalline LiF was studied, he found that the drag effects will cause the yield stress to be increased by as much as 200% when applying pressure up to 10 kbar (1 GPa). Due to the large increment, this process is very unlikely to occur in the oriented single crystal, but can happen in the polycrystalline Ta where increments of these levels are present.

1.3.3.5 Dislocation Interaction

Another possible controlling factor of dislocation mobility is the dragging effect of interaction with other dislocations. Here the concern is to know the effect of pressure on the nature of the interaction. Hanaffe [82] studied this interaction. He followed the procedure that when the screw dislocations were halted by intersections the velocities were not plotted at one atmosphere or at pressure. The average of intersections of screw dislocations on {110} planes with screw dislocations on {110} planes would be the same at pressure as at 1 atmosphere. Thus, it can be concluded that the total number of intersections would be the same as at 1 atmosphere. So, if the change in dislocation mobility with pressure is the result of dislocation interaction mechanisms, it can only be due to an increase in the interaction forces.

The forces between dislocations can be calculated using the Peach- Koehler equation. In the case of two parallel screw dislocations we have the following expression in Equation 4.9

$$F = \frac{Gbb'}{2\pi r}\vec{r} \tag{4.9}$$

where G is the shear modulus, b and b' are the burgers vector of the dislocations and r is the separation between dislocations.

This is a simple form of the Peach-Koehler equation, a more complex equation could be derived for particular dislocation arrangements, some of these can be found in Weertman's Elementary dislocation theory [38]. Here as the Peierls stress, the equation reveals that the energy of interaction depends again on G, b and ν.

Chapter 2
Characterization and Modeling Techniques

A short introduction to the characterization and the modeling techniques used during the research is given here. Standard SEM and TEM analyses were used to characterize the material. In addition microhardness and electron backscatter diffraction (EBSD) are important for validation of the experiment. Along with the experimental efforts, simulations tools were obtained and run in our facilities. The simulations were expected to provide an insight on the mechanisms occurring in our tests and were used either to corroborate or disregard some of our assumptions. These are briefly described below. The results and information obtained from these techniques are presented in later chapters.

2.1 Microhardness

Hardness testing represents a fast and economical method for material evaluation. It is measured in terms of the size of an impression made on a specimen by an indenter of a specified shape when a specified force is applied for a given time. The indent is measured after the force has been removed. Examples of indirect information obtained through hardness testing are: service life, wear behavior and even information about the material strength.

In the Vickers hardness test a diamond indenter, in the form of a square-based pyramid with an angle of 136º between the opposite faces at the vertex, is pressed into the surface of the test piece using a prescribed force. After the force has been removed, the diagonal lengths of the indentation d_1 and d_2 are measured optically.

The Vickers hardness number HV is the test force divided by the sloping area of the indenter up to a depth where it has the same cross-sectional area as the residual indent:

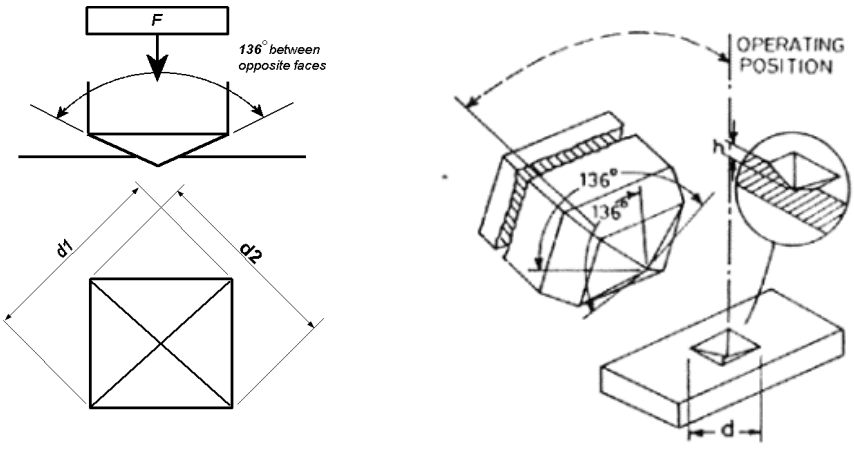

Figure 2.1 Vickers hardness apparatus [website]

HV = Constant × Test force / Surface area of indentation

$$HV = 0.102 \times \frac{2F \sin\left(\frac{\alpha}{2}\right)}{d^2} \qquad (2.1)$$

where: d = arithmetic mean, in mm, of the two diagonal lengths d_1 and d_2

In the present work the hardness measurements were used to study the changes in material strength in our samples. It is true that the hardness often provides only limited information about the material property that is directly of interest. Therefore it was combined with other techniques to validate the conclusions reached by using this method.

.

2.2 Electron Backscatter Diffraction - Orientation Imaging Microscopy

Orientation imaging microscopy (OIM) is an imaging technique based on the indexing of electron backscatter diffraction patterns (EBSP). EBSPs are produced when electrons of narrowly defined energy strike a crystalline sample. The backscatter-diffracted electrons are distributed on the surfaces of cones and for each diffracted plane there will be two cones. The diffracted electrons can be detected using a phosphor screen, which captures the conic sections that form a pair of lines on the screen. These lines are called Kikuchi bands and their width depends on the lattice spacing, and the crystal orientation. The pattern can be indexed with knowledge of the Bravais lattice (FCC, BCC, etc) and the relative width of the lines. This process is depicted in Figure 2.2.

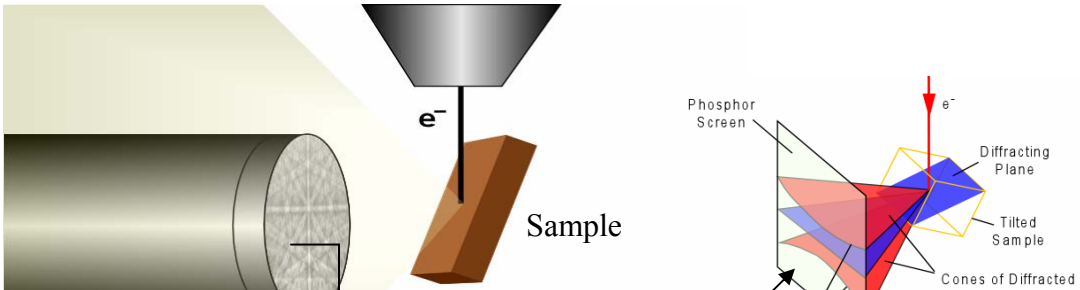

Figure 2.2 Basic arrangement of the EBSD system [88]

With this information, an orientation map can be created. This figure shows the position of a sample direction relative to the crystal reference frame using an orientation color key. The sample direction is considered by entering indices defining a vector by components of the samples axes (RD, TD and ND).

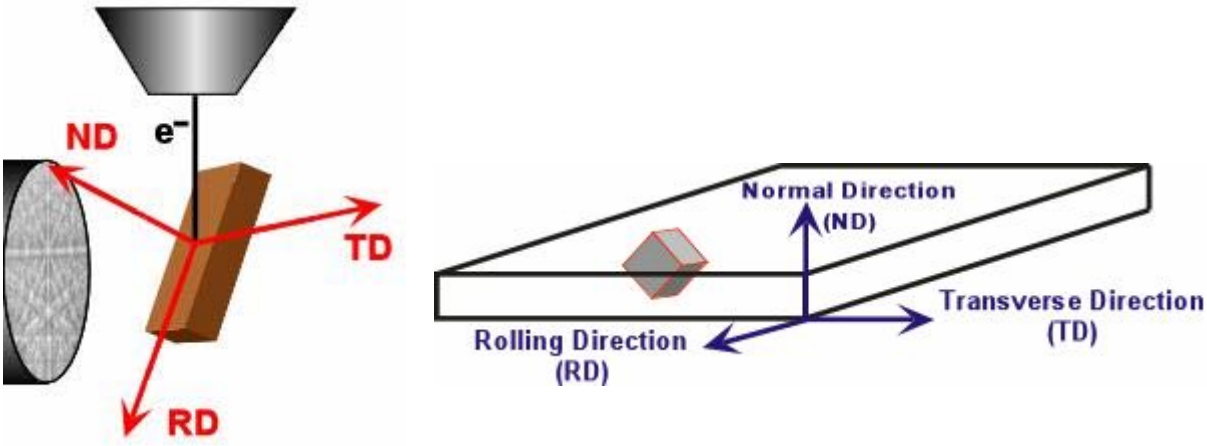

Figure 2.3 Assignment of frame reference [88]

Because of symmetry each orientation will produce several points at symmetrically equivalent locations in the plot. If the inverse pole figure is plotted using only the unit triangle, then only one point per orientation will appear in the plot as shown in Figure 2.4.

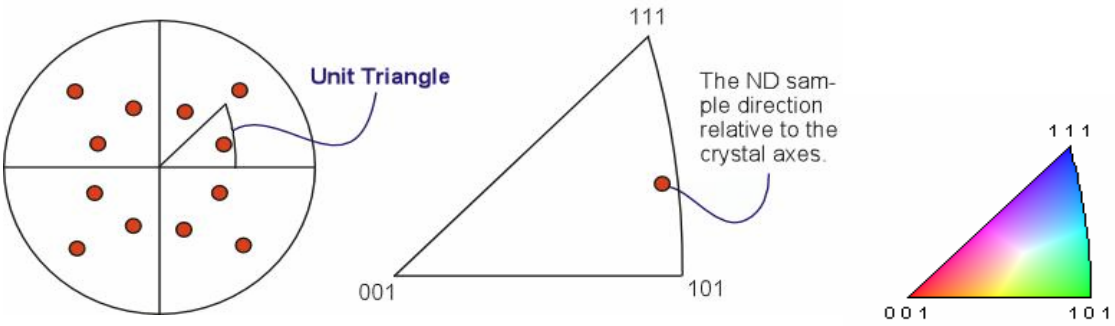

Figure 2.4 a) Full pole figure, b) Unit triangle, c)color code [88]

The orientation maps are generated for the data obtained using a color code for the stereographic unit triangle (Figure 2.4c). The grains closer to the (111) orientation are colored blue while those close to the (001) are red. Figure 2.5 shows an orientation image of a cross-section of the Ta foil used in this research.

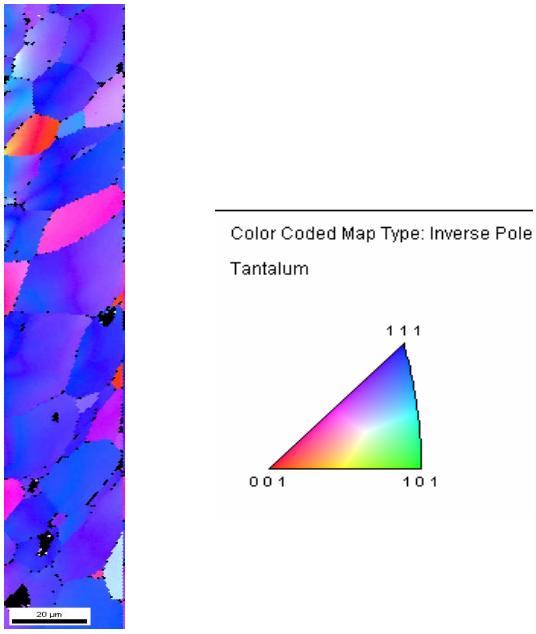

Figure 2.5 Orientation image and the color code map of the Ta foil cross section.

The image is based on the quality of the Kikuchi pattern, this quality depends on how good is the diffraction process and therefore is a function of the amount of defects in the lattice of the specimen, the most common of these defects is the dislocation content.

During the experimental research this technique was used to characterize the polycrystalline Ta and experimentally determine the zones that were load bearing, giving an indication of the distribution of the pressure. It was also used as a tool to find the orientation of the Mo single crystals.

2.3 Transmission electron microscopy

Transmission electron microscopy (**TEM**) is by far the most important technique for studying defects in great detail. Much of what was stated before about defects would be speculative theory, or would never have been conceived without **TEM**. The electrons interact with the material in two ways: inelastic and elastic scattering. Inelastic scattering (leading eventually to absorption) must be avoided since it contains no local information. The electron beam then will be only elastically scattered, i.e. diffracted; the lattice and the defects present modulate amplitude and phase of the primary beam and the diffracted beams locally. The image, or better, the contrast of a dislocation depends on several parameters. Most important are:

- The diffraction conditions. the Bragg condition fulfilled for many reciprocal lattice vectors *g*, for none, or just for two. All cases are easily adjusted by tilting the specimen relative to the electron beam while watching the diffraction pattern. The preferred condition for regular imaging is the "two-beam" case with only one "reflex" excited; i.e. the Bragg condition is only met for one point in the reciprocal lattice or one diffraction vector *g* (usually with small Miller indices, e.g. {111} or {220}.

- The excitation error: with the Bragg condition met exactly (excitation error = 0; dynamical case) or only approximately (excitation error < 0 or > 0; kinematical case).
- The magnitude of the scalar product between the reciprocal lattice vector g and the Burgers vector b, $\mathbf{g} \cdot \mathbf{b}$. If it is zero or very small, the contrast is weak, i.e. the dislocation is invisible.
- At least four (usually five) imaging lenses are needed in addition to two condenser lenses (not shown). For most imaging modes an aperture right after the objective lens must be provided.
- The beam paths for the diffraction mode and the imaging mode are shown Figure 2.6.

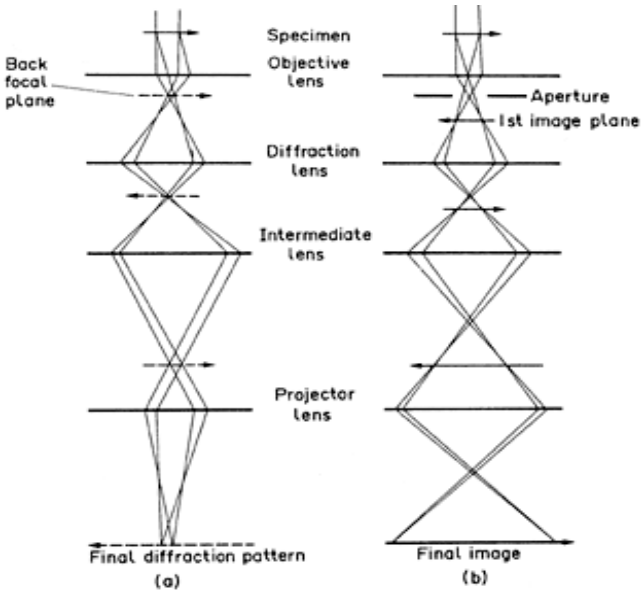

Figure 2.6 Schematic of the basic design of the TEM [website]

- The most important lens is the objective lens. Its resolution limit defines the resolution of the whole microscope. The aperture after the objective lens is

essential for the conventional imaging modes. It is usually set to only admit the primary beam, or one of the diffracted beams into the optical system.

Figure 2.7 illustrates some imaging conditions for dislocations with maximum and minimum **g.b** product.

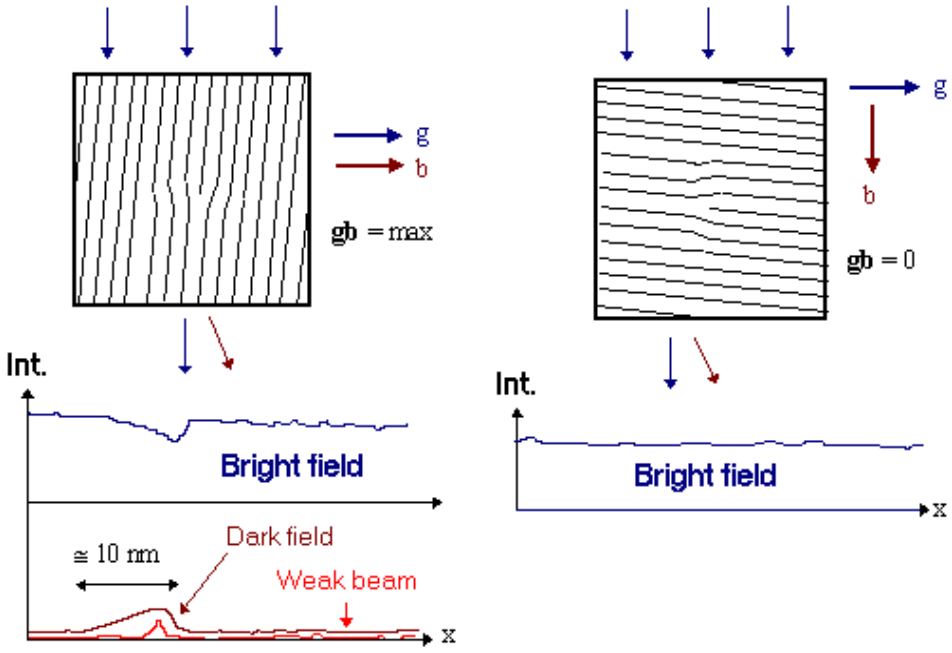

*Figure 2.7 Minimum and maximum of **g.b.** [web]*

Summary of TEM contrast

- Dislocations are invisible or exhibit only weak contrast if $\boldsymbol{g} \cdot \boldsymbol{b} = 0$. This can be used for a Burgers vector analysis by imaging the same dislocation with different diffraction vectors and observing the contrast.
- Under kinematic bright field conditions (Bragg condition met almost, but not quite), the dislocation is imaged as a dark line on a bright background. The width

of the line corresponds to the width of the region next to one side of the dislocation where the Bragg condition is now met; which is usually several nm.

- Under dark field conditions the dislocation appears bright on a dark background
- Under dark field conditions with large excitation errors the Bragg condition is only met in a small region close to the core of the dislocation. The image consists of a thin white line on a pitch black background. This is the so-called "weak-beam" condition; it has the highest resolution of conventional imaging modes. It is hard to use, however, because almost nothing is seen on the screen (making adjustments difficult) and long exposure times are needed which are only practical with a very stable instrument.

2.4 Visco-Plastic Self-Consistent (VPSC) formulation

Description

VPSC is a computer code written in FORTRAN 77 which simulates the plastic deformation of polycrystalline aggregates. VPSC stands for Visco Plastic Self Consistent and refers to the particular mechanical regime addressed (VP) and to the approach used (SC). VPSC accounts for full anisotropy in properties and response of the single crystals and the aggregate. It simulates the plastic deformation of aggregates subjected to external strains and stresses. VPSC is based on the physical deformation mechanisms of slip and twinning, and accounts for grain interaction effects. In addition to providing the macroscopic stress-strain response, it accounts for hardening, reorientation and shape change of individual grains. As a consequence, it predicts the evolution of hardening and

texture associated with plastic forming. The simulation procedure can be applied to deformation of metals, intermetallics and geologic aggregates.

Self-consistent polycrystal formalism

In brief, the polycrystal is represented by means of weighted orientations. The orientations represent grains and the weights represent volume fractions. The latter are chosen to reproduce the initial texture of the material. Each grain is treated as an ellipsoidal visco-plastic inclusion embedded in an effective visco-plastic medium. Both, inclusion and medium have fully anisotropic properties. The effective medium represents the 'average' environment 'seen' by each grain. Deformation is based on crystal plasticity mechanisms -slip and twinning systems- activated by a Resolved Shear Stress. Comprehensive derivations can be found in Tomé and Lebensohn [89,90].

Algorithm

Details of the VPSC formalism/calculations are given in the appendix section for interested readers. To keep with the flow of this thesis we describe here the algorithm that contains the steps required to predict the local and overall visco-plastic response of a polycrystal.

- For an applied macroscopic velocity gradient $\dot{U}_{i,j} = D_{ij} + W_{ij}$ (decomposed here into the symmetric strain-rate D_{ij} and the skew-symmetric rotation-rate W_{ij}). In order to start an iterative search of the local states, one should assume initial

values for the local deviatoric stresses and moduli. Starting with an initial Taylor guess, i..e.: $d_{ij} = D_{ij}$ for all grains, we solve the non-linear Equation and use of an appropriate linearization scheme to calculate initial values of σ'_{ij}, M_{ijkl} and d^{o}_{ij}, respectively, for each grain .

- Next, initial guesses for the macroscopic moduli $\overline{M}_{ijkl}$ and D^{o}_{ij} (usually simple averages of the corresponding local moduli) are obtained. With them, and the applied strain-rate D_{ij}, the initial guess for the macroscopic stress follows from the inversion of the macroscopic constitutive law, while the Eshelby tensors S_{ijmn} and Π_{ijmn} can be calculated using the macroscopic moduli and the grain shape by means of the procedure described above

- Subsequently, the interaction tensor $\widetilde{M}_{ijkl}$, and the localization tensors B_{ijkl} and Φ_{ij}, can be obtained as well. With these tensors, new estimates of $\overline{M}_{ijkl}$ and D^{o}_{ij} are obtained by solving iteratively the self-consistent equations (for unique grain shape or for a distribution of grain shapes). After achieving convergence on the macroscopic moduli (and, consequently, also on the macroscopic stress Σ'_{ij} and the interaction tensor $\widetilde{M}_{ijkl}$), a new estimate of the grain stress can be obtained combining the local constitutive equation and the interaction equation as follows:

$$\dot{\gamma}_o \sum_s m_{ij}^s \left(\frac{m_{pq}^s \ \sigma'_{pq}}{\tau^s} \right)^n - D_{ij} = -\widetilde{M}_{ijkl} \left(\sigma'_{kl} - \Sigma'_{kl} \right) \tag{2.2}$$

Equation (2.2) constitutes a 5x5 non-linear system of algebraic equations, where the unknowns are the five independent components of the deviatoric stress tensor σ'_{kl} of the grain. If the recalculated local stresses are different from the input values for any of the grains that constitute the polycrystal, a new iteration should be started. Otherwise, the iterative scheme is completed and the shear-rates on the slip (or twinning) systems and the strain-rate of each grain are calculated, while the rotation-rate of each grain is obtained as:

$$w_{ij} = W_{ij} + \widetilde{w}_{ij} \tag{2.3}$$

where $\widetilde{w}_{ij}$ is given by $\widetilde{w}_{ij} = \Pi_{ijkl} d^*_{kl} = \Pi_{ijkl} S^{-1}_{klmn} \widetilde{d}_{mn}$.

- The above numerical scheme can be used either to obtain the anisotropic response of the polycrystal, probing it along different strain-paths (i.e.: applying different strain-rates D_{ij} and obtaining the corresponding stress response Σ'_{ij}), or to predict texture development, by applying incremental deformation steps. The latter case requires the incremental updating of the shape and the orientation of the grains (due to both slip and twinning reorientation) and updating the critical stress of the deformation systems, due to strain hardening, as well.

Example: rolling of a BCC structure

The samples to be used for this study were obtained out of a thin foil of Ta with a nominal thickness of 50 μm. To get to a sheet of this thickness the starting material was most likely rolled. Presented here is an example meant to familiarize the user/reader with the simulation tool and to test the predicted microstructure with the measured Ta samples.

Run conditions:

- Initial random texture file RAND500.TEX with 500 orientations.
- BCC crystals with slip on {110}<111>, {112}<111>, {123}<111>
- Plane strain up to ε_{33}=100% using one or three deformation modes.

Cases A and B:

These two cases differ in that deformation is accommodated using either {110}<111> slip, or {110}<111> + {112}<111> + {123}<111> slip, respectively. The latter case can is usually regarded as 'pencil glide'. Figure 2-8 depicts the texture of the

rolled sheet. These results were obtained from the VPSC manual provided by Dr. Tomé of Los Alamos National Lab.

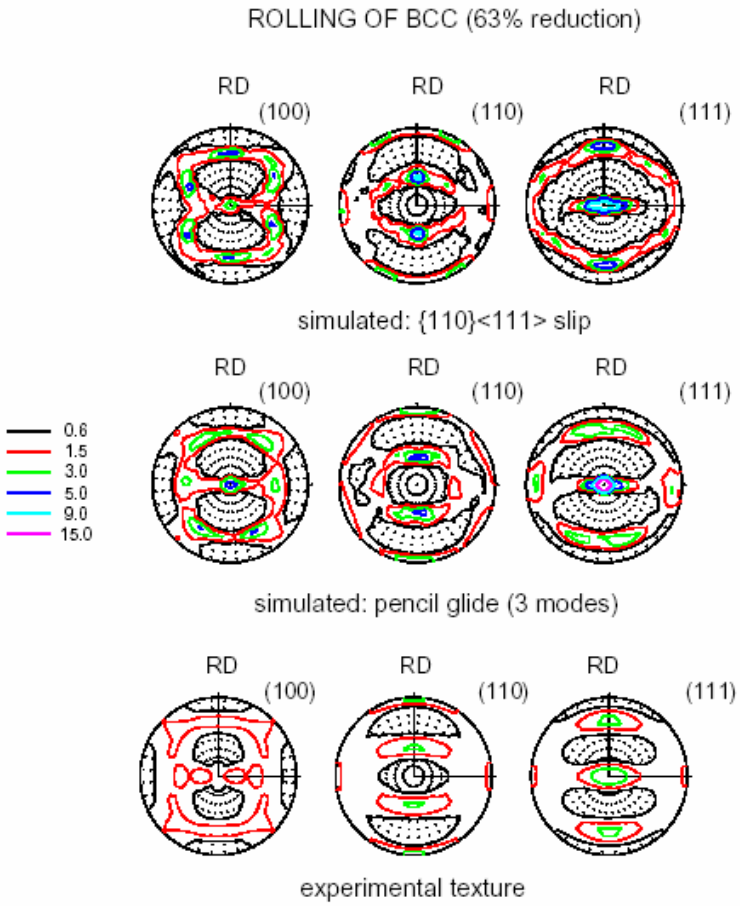

Figure 2.8 Texture of BCC after 63% rolling reduction. Simulations assume either {110}<111> slip, or {110}<111> + {112}<111> + {123}<111> slip (pencil glide) [91].

A Matlab program was written in order to be able to convert our data to the necessary input files required by the VPSC program, and viceversa, convert the output files given by the VPSC code to a format that could be used by the OIM software, details are given in the Appendix 3.

The simulation of the rolling process was performed and the results are given in Figure 2.9

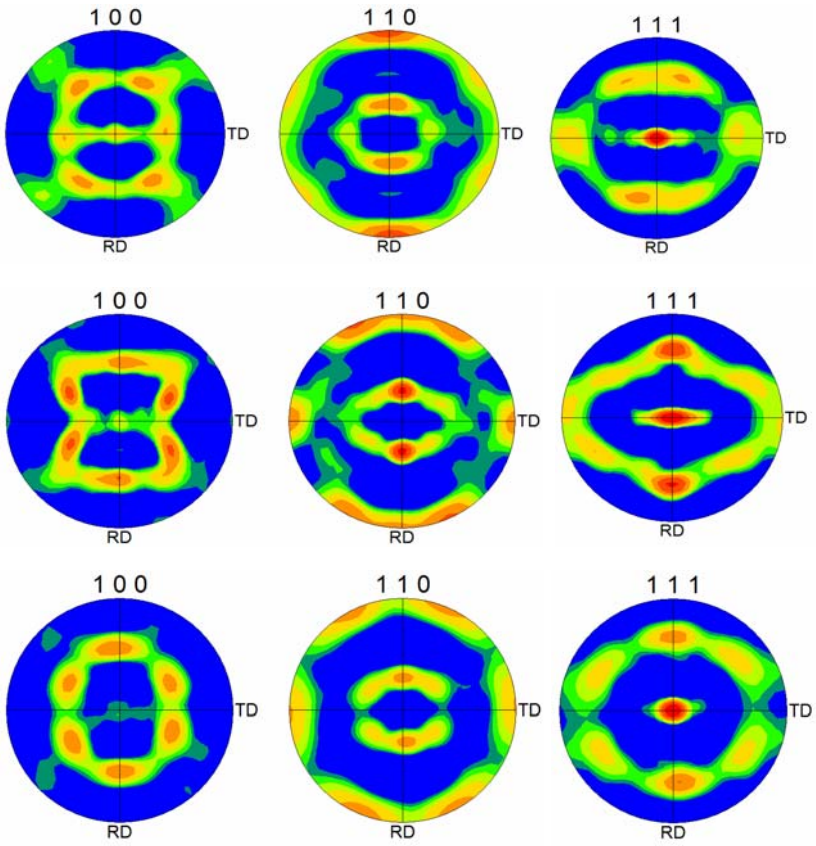

Figure 2.9: Texture of BCC after 63% rolling reduction. Simulations (a){110}<111> slip, (b) pencil glide (c) Experimental obtained from the Ta foil.

Comparing Figures 2.9 (a) and (b) with their respective in Figures 2.8 it was confirmed that we were able to reproduce the expected results. Figure 2.9 (c) shows the experimental microstructure of one of our samples, and as was predicted/expected it is the typical microstructure of BCC material that has undergone a rolling process.

One of the advantages of sing the OIM software as a post processing analysis tool is that it allows for easier visualization and manipulation of the data with all the built-in

capabilities of the software. To exemplify, see Figure 2.10, where it is shown the predicted microstructure for the previous cases in the form of Inverse Pole Figure Maps.

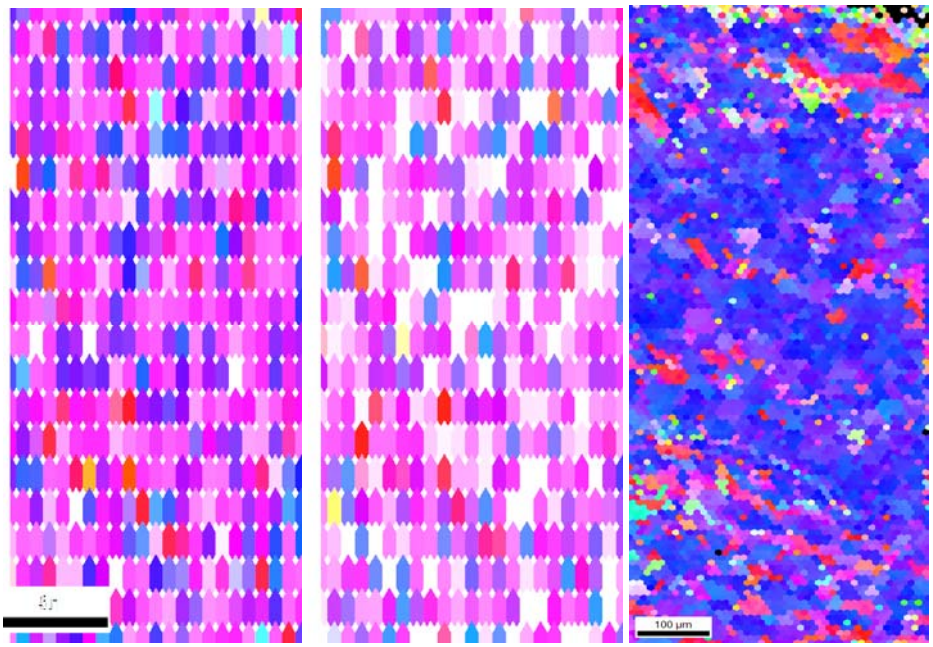

Figure 2.10 IPF of the microstructures after 63% rolling reduction. Simulations (a){110}<111> slip, (b) pencil glide (c) Experimental obtained from the Ta foil.

These results can be compared easily with the EBSD scan performed on one of the samples shown in Figure 2.10 (c).

2.5 Dislocation dynamics

Description

The 3D discrete dislocation model *(micro3d)* developed at WSU by Dr. Zbib and co-workers simulates the behavior of large numbers of dislocations [17-18,20]. The model is based on fundamental laws that govern dislocation motion and their interaction

with various defects and interfaces. The model as it is contains all the salient features that should be considered when simulating the behavior of bcc metals, such as the double kink nucleation on large segments of screw dislocation, the freedom to allow cross slipping of dislocations to adjacent planes, and all the short and long range interactions between dislocation that could lead to the formation of jogs.

Algorithm

It has been constructed within a generalized enough framework so that many classes of dislocation problems can be investigated, including:

a) Simple dislocation mechanisms, such as Frank-Read sources.
b) Stability of dislocation cell structures, such as cell walls and dislocation boundaries.
c) Evolution of random distribution of dislocations.
d) Interaction among dislocations and point defects and particles, SFT's, loops, etc.

The main issue is to predict the spatio-temporal evolution of the dynamical and self-organizing system consisting of N dislocation segments, and the manner in which they interact with each other and other defects and surfaces to determine the overall strength of the metal under various loading conditions. The fundamental aspects of the model are built from the basic physical laws that govern:

a) the mobility of an individual dislocation,
b) short range interactions between two dislocations on core level, and

c) long-range interactions associated with elastic distortions.

The main governing equation for the dynamics of each dislocation segment is given by [73]

$$m_i^* \dot{\mathbf{v}}_i + \frac{1}{M_i(T,p)} \dot{\mathbf{v}}_i = \left[\sum_{j=1}^{N-1} (\boldsymbol{\sigma}_{j,j+1}^{D} + \boldsymbol{\sigma}^{a}).\mathbf{b}_i \times \boldsymbol{\xi}_i + \mathbf{F}_{i-self} \right]_{glide-component} \quad (2.4)$$

Here $\boldsymbol{F_i(v)}$ is the inertial force, $\boldsymbol{v_i}$ is the dislocation segment velocity, M_g is the mobility, $\boldsymbol{F}^{a}$ is the force produced by applied stresses, and $\boldsymbol{F}_i^{int}$ is the internal force arising from interactions with other defects and dislocations and from the Peierls barrier if present. Calculation of the long range interaction is most expensive (order N^2). Therefore, a method was developed (superdislocation method) to reduce the order of interaction (to *NlogN*) with high accuracy [15,20].

Determination of the mobility and interaction forces (long range elastic stress fields, and short range) constitutes the core of the model. Generally, M_g is a function of the angle between the Burgers vector and the dislocation line sense, especially at low temperatures. In bcc single crystals, at low temperatures a pure screw dislocation has a rather complex three-dimensional core structure, resulting in a high Peierls stress which is overcome by stress-assisted thermal activation [73]. This leads to a relatively low mobility for screw dislocations while the mobility of mixed dislocations is very high. The kinetics of a screw dislocation is characterized by the mechanism of the succession of kink nucleation and lateral double kink migration, which are edge dislocations. This theory leads to a temperature-dependent mobility with activation enthalpy associated with

kink nucleation. The *"assumed"* constitutive nature of the plastic deformation tensor $\boldsymbol{D}^p$ and flow stress and their dependence upon internal variables and gradients of internal variables is very critical, since they dictate, among other things, the length scale of the problem and the phenomena that the model can capture.

In short terms, the discrete dislocation dynamics model (*micro3d*) provides the most rigorous and physically based approach for computing the plastic strain and strain hardening in metals through an explicit evaluation of the motion and evolution of all individual discrete dislocations in the crystal.

Example: Dislocation multiplication in Mo

Presented next is an application of how the dislocation dynamics code was used to study the plastic deformation of Mo single crystals. The dislocation arrangement obtained during the DD simulation is shown in Figure 2.11, and the overall stress-strain response in Figure 2.11(*b*). The latter shows well-resolved plastic yield behavior, with the yield stress of 130 MPa, in reasonable agreement with experimental observations [92]

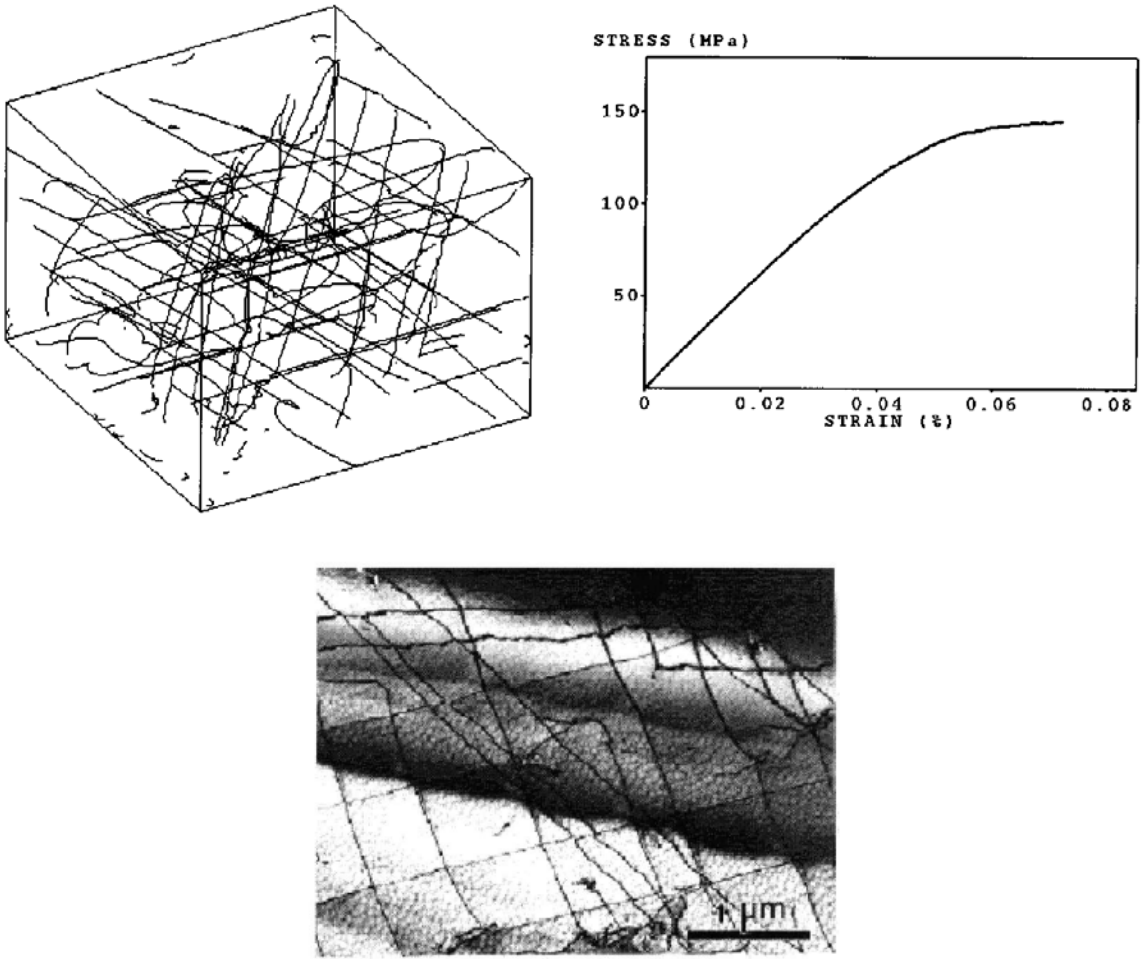

Figure 2.11 (a) A snapshot of the simulated microstructure. (b) The simulated stress-strain response in the inset. (c) TEM micrograph showing characteristic cross-grids of screw dislocations [92].

The characteristic cross-grid pattern is also clearly observed and should be compared with the transmission electron micrograph of the deformed specimen given in Figure 2.10(*c*). The cross-grid consists of two sets of intersecting screw dislocations with ½ [1-11] and ½ [1-11] Burgers vectors respectively, viewed along the [101] direction.

Chapter 3
Experimental development

3.1 Bridgman original anvil cell

Of the various types of cells developed by Bridgman for high-pressure work, the one developed for applying a shearing load on thin samples specimens under high pressure most closely achieves the desired test objectives. This cell is described schematically in Figure 3.1

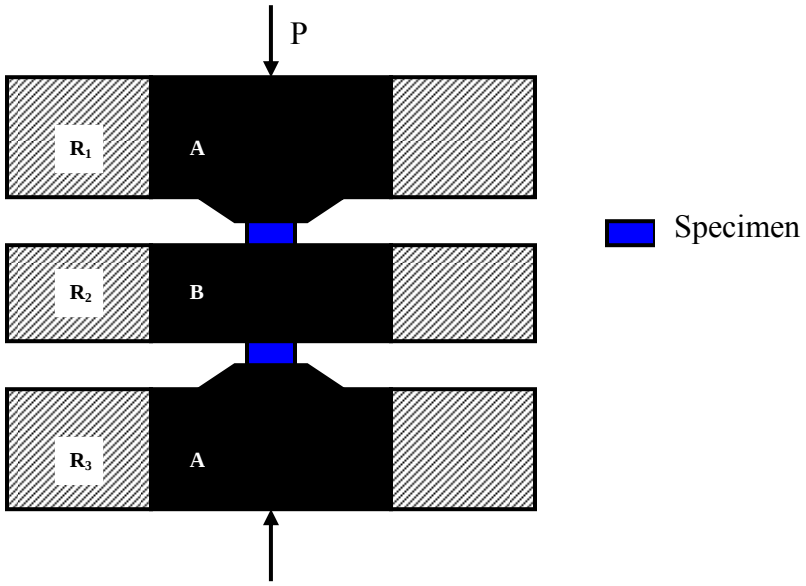

Figure 3.1 Schematic of the original Bridgman anvil cell.

In Bridgman's original design [21-23,25,28] blocks **A** are two hardened steel cylindrical blocks bearing short platens **C** with a 1° taper double angle**. B** is a rectangular block of hardened steel. All of them are press fitted into the hardened steel rings $\mathbf{R_1}$, $\mathbf{R_2}$ and $\mathbf{R_3}$. The specimens to be tested are small thin disks placed between block **B** and the platens **C**. The whole assembly, mounted in a jig to keep the alignment, was placed

between the plates of the hydraulic press. Load is applied to blocks **A,** causing the material to extrude laterally until an equilibrium thickness is reached. For most of the materials this thickness was close to 25 microns, in this equilibrium thickness the material being tested is in a condition of hydrostatic pressure over most of the interior region, with a narrow annulus near the edge where there is a radially direct component of the shearing stresses produced by the friction of the material. In fact it is these radially directed shearing frictional forces, which seal the specimen and directs the force towards the interior region, as illustrated in Figure 3.2.

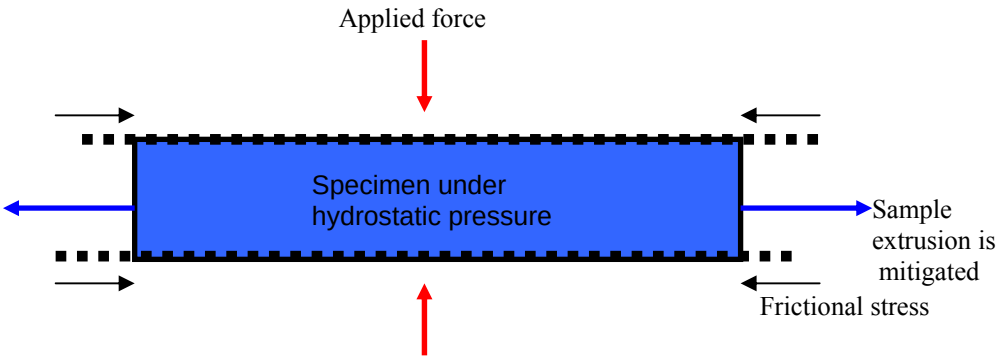

Figure 3.2 Schematic showing how the hydrostatic pressure is accomplished by exerting axial load and frictional stress.

Having the specimen under pressure the block **B** then is rotated about the axis through the platens **C**. At low pressures rotation is achieved by surface slip between the specimen and the blocks, when the pressure is high enough the surfaces of the specimen stick to the roughened anvils and rotation causes plastic deformation of the materials being examined. The experiment basically consists of measuring how much torque is required to rotate as function of thrust exerted by the press. Simple calculation can lead to an estimation of the shear stress as a function of mean pressure.

3.2 Experimental set up

Using the concept of Bridgman's cell, a new high-pressure testing apparatus was designed and constructed at LLNL. Modifications were made to adapt the system to our facilities (given in the Appendix section. A schematic of the complete device is depicted in Figures 3.3 and 3.4. It consists of a set of upper platens (p1) attached to the crosshead of a biaxial materials testing system with the bottom platens free to perform vertical and angular displacements. Angular displacement is accomplished using a driving clevis (p5) attached to the bottom part of the apparatus.

The experiment described in this work enables monitoring of the mechanical response of materials deformed in shear under hydrostatic pressure in the range of 0-50 GPa depending upon the size of the specimens. Observations of the pressure-induced work hardening and, of special interest, measurement of the pressure-dependent dislocation mobility in oriented single crystals are goals of the experiment.

A stationary sleeve rigidly attached to the upper platen and fitting with close tolerance over the lower platen ensures proper alignment between the mating surfaces while the load is applied. Brass rings were attached at the top and bottom of the lower barrel to avoid steel on steel friction during loading. To ensure that frictional forces would be negligible, a low viscosity lubricant, 30 weight oil, was spread on the brass rings.

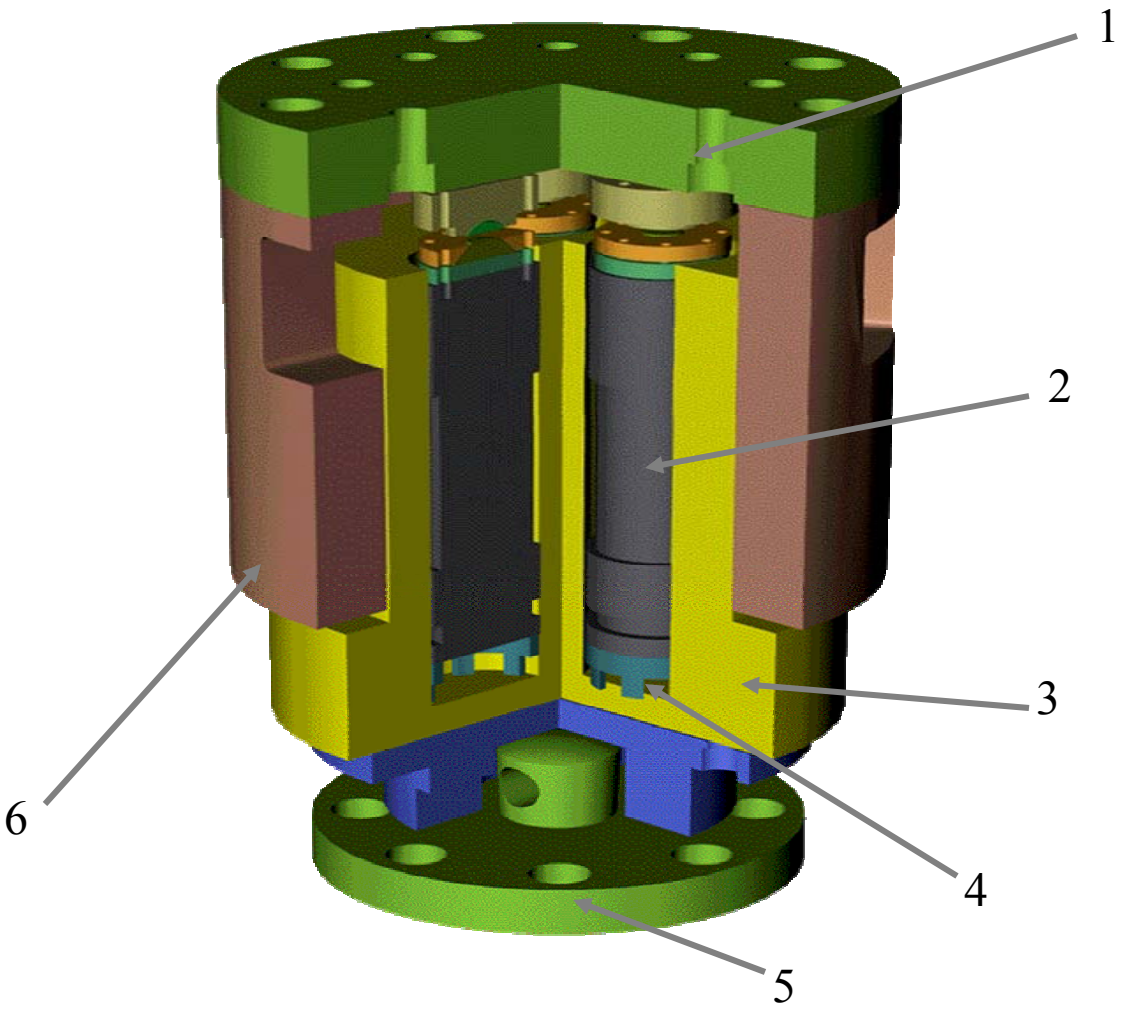

Figure 3.3 Schematic of the apparatus used for high-pressure deformation.

1. Upper part containing upper platens
2. Piston
3. Brass ring
4. Oil reservoir
5. Clevis attached to the ram
6. Outer

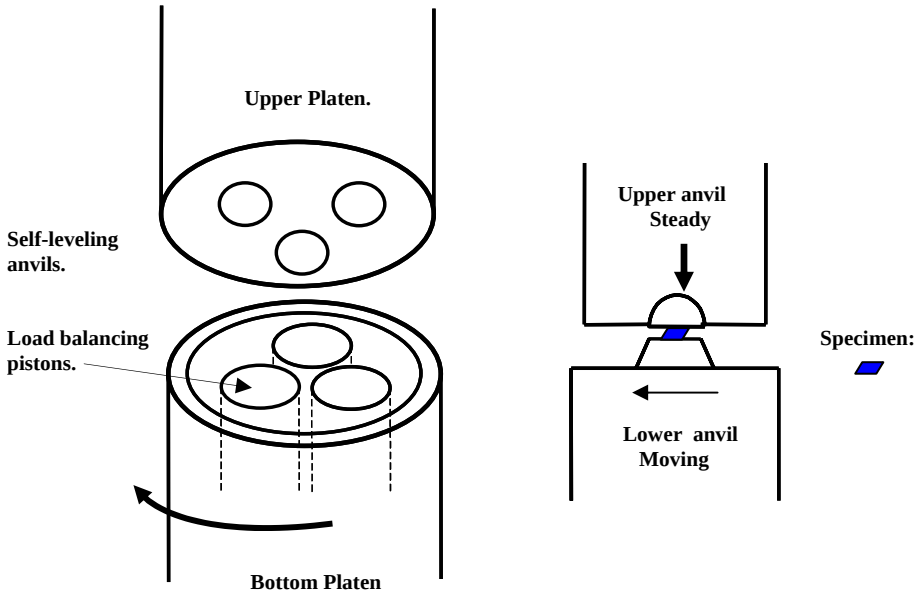

Figure 3.4 – Simplification of the schematic of the modified Bridgman cell used to perform the experiments. The specimens are plastically deformed in shear by the torsion motion of the bottom platen.

In this modified Bridgman cell, three independent supported anvils in both the top and bottom platens are arranged symmetrically. The anvil centers are all positioned on a circle centered on the loading axis of the testing system. This arrangement produces a near negligible shear strain gradient as compared with the original Bridgman single anvil design, thereby creating a more uniform shear stress in the specimen. The anvils in the top platen are formed with a hemispherical section that fits snugly into the mating surface. Using a thin foil of indium between these hemispherical surfaces provides for self-leveling of the anvils upon initial loading. Equal pressure is attained between all anvils by positioning each anvil atop a hydraulically-controlled piston, all of which are connected to a common oil reservoir. For the "tri-anvil" testing apparatus the anvil material chosen was tungsten carbide. The surfaces of the anvils were roughened (using 1200 grit emery cloth) to have better frictional contact with the specimens. This enables

one to monitor the strain of the specimens by measuring the displacement of the platens relative to each other.

The deformation of the specimens in the tri-anvil apparatus is achieved with the same general philosophy as with the original Bridgman design: axial load followed by rotational displacement, this can be divided into a four-step process:

First, the specimens are centered on each anvil using a sample-positioning tool. The tool is specially designed for each specimen geometry, and aligns the center of each specimen to within 25 μm of the anvil center. The bottom platen is vertically displaced leaving a small gap between the specimens and the upper anvils.

Second, axial load is applied using load control and a rate of 2.2kN/sec (500 lbf/sec) once the desired load is reached, it is held constant. As in the original experiment, although some slip in the surface of the material could be present at low pressures, when the pressure is high enough the surfaces of the specimen stick to the roughened anvils (evidence of this is presented later in the discussion). Once the specimens are under the desired pressure, the third step consists of rotational displacement applied to the bottom platen, causing essentially unidirectional shearing strains on the specimens positioned within each anvil, as shown in Figure 3.4.

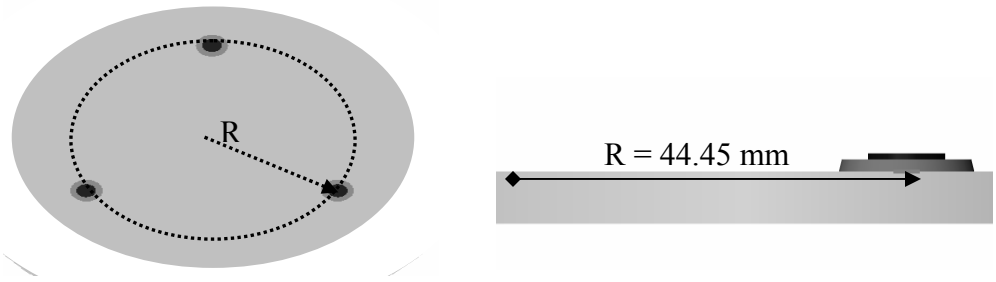

Figure 3.5 – Schematic of anvils arranged in the lower plate.

The shear loading can be assumed unidirectional because of the small specimen size, (radius/thickness ratio ranges from 60 – 600) and low angle rotations ($\theta \approx 0.5^{o} = 8.7$ mrad) in comparison to the circumference of the circle on which the specimens lie R = 44.45 mm. Because of the small angle through which the deformation occurs, the approximation $l = R \tan \theta \approx R\theta$ can be used. Finally, the specimens are unloaded and recovered for post-mortem analysis.

To measure local strain in the specimen being deformed, displacement gages were attached to the saddles placed at the bottoms and tops of the platens. The properties of the strain gages are shown in Appendix A1. The compliance of the machine can also be seen in the Appendix section. The extensometers were calibrated using an Instron micrometer stage extensometer calibrator in the range of +/- .015 inches using a excitation voltage of 5 V and the signal conditioning equipment from the MTS system in our facilities.

To verify that the torque measurements read by the system were due to the specimen tested and not intrinsic friction of the apparatus, a test without load and a rotation rate of 0.3 degrees / minute was performed. A value of .254 ± 0.0147 N-m was read by the ram of the MTS machine. The expected shear stress for the specimens is expected to be at least 60 MPa, translated to a torque of 50 N-m. Therefore, the intrinsic torque is on the order of less than 1%, and can be neglected.

3.3 Validation of the experiment

There are two major concerns when using this type of device for producing a nearly homogeneous hydrostatic pressure in the sample being tested. These two are the nature and magnitude of the pressure distribution in the sample. By nature is meant to what extent the stress state in the sample evolves from a pure compression to pure hydrostatic pressure. The second is related to the pressure gradients that may/do exist in the sample. The one-anvil Bridgman cell has been used by different authors over the course of the years [93-97]. Since its inception it was recognized that the original set up presented a problem with the distribution of the pressure within the sample, this problem was even mentioned by Bridgman, who a reported all his findings as function of mean pressures. In this section experimental evidence will be shown in order to prove that these two major problems can be overcome (or nearly solved) by using specimens with a ratio of diameter/ thickness on the order of 60-600 and by redesigning the geometry of the upper and lower anvils from flat-flat to flat-domed.

3.3.1 State of stress

As in the Bridgman experiments it was anticipated that when pressure is applied the material deforms elastically until an equilibrium thickness is reached and hydrostatic pressure is distributed inside the specimen [21-23,25]. Therefore it is imperative to the establishment of this new experimental technique the determination that the stress state in the material upon initial loading is primarily hydrostatic. It is known that plastic deformation in metallic systems occurs primarily via dislocation generation and

movement due to shear stresses. The effective stress $\bar{\sigma}$ is equal to σ_y, the yield strength in tension. The effective stress is given by von Mises [54] as

$$\bar{\sigma} = \frac{1}{\sqrt{2}}[(\sigma_1 - \sigma_2)^2 + (\sigma_2 - \sigma_3)^2 + (\sigma_3 - \sigma_1)^2]^{1/2} \quad (3.1)$$

where σ_1, σ_2, and σ_3 represent the principal stresses. In the case of hydrostatic pressure, $\sigma_1 = \sigma_2 = \sigma_3$, which results in no shear stresses present to provide a driving force for dislocation motion, therefore structural properties are not changed due to hydrostatic pressure alone. Experimentally, as it was realized by Bridgman and follower workers in the field of high pressure [93,95] it is difficult to achieve a pure hydrostatic pressure, a realistic goal would be to have the deviatoric components such as σ_{31} below the critical shear stress for the material, in this case as it will be shown later in this dissertation about 50 MPa for Ta. By using Equation 3.1, the von Mises shear stress. In this case the sample is symmetric in the xy plane, then we can assume $\sigma_1 = \sigma_2$, therefore the effective stress could be simplified to

$$\bar{\sigma} = \frac{1}{\sqrt{2}}[(\sigma_1 - \sigma_3)^2 + (\sigma_3 - \sigma_1)^2]^{1/2} = |(\sigma_3 - \sigma_1)| \leq \tau_{Ta} = 50\text{MPa}$$

The tests will be run such that $\sigma_3 : 2 - 4\text{GPa}(= 2000 - 4000\text{MPa})$ meaning that σ_1, σ_2 should be at the most 2.5 % (for 2 GPa) different from σ_1, by staying within this limit we can develop a near pure hydrostatic state being imposed on the samples.

In order to determine whether the desired state of hydrostatic pressure could be attained by applying axial load on the thin foil specimens, initial tests were performed on polycrystalline tantalum samples at pressures of 2.0-4.0 GPa. The foils of polycrystalline tantalum were purchased from Goodfellow, Inc. with an impurity content of less than 0.1

% (Al 5, Ca 2, Co 1, Cr 5, Cu 2, Fe 30, Mg 5, Mn 2, Mo 100, Na 10, Nb <500, Ni 3, Si 10, Sn 2, Ti 20, all ppm), annealing and purification processes will be given in Chapter 4. The specimens to be tested were obtained from the foil using a punch designed for TEM sample preparation. The geometry of the specimens was disk-shaped with a diameter of 3.0 mm and a nominal thickness of 50 +/- 10 μm.

As it is known that dislocation activity causes strain hardening in the material, so if significant dislocation activity occurs, the hardness of the metal after loading could be expected to increase. Finally, direct observation of the microstructures by EBSD and TEM should reveal the microstructural changes due to dislocation activity. The absence of dislocation activity will ensure that the test objectives were achieved.

3.3.1.1 Initial characterization of polycrystalline Tantalum

Automated electron backscatter diffraction (EBSD) was used to characterize the initial structure of the annealed Ta foils. This technique was introduced in Chapter 2, and is used to reveal the texture and grain size distribution of the material as well as spatially specific information such as structural gradients and misorientation distributions.

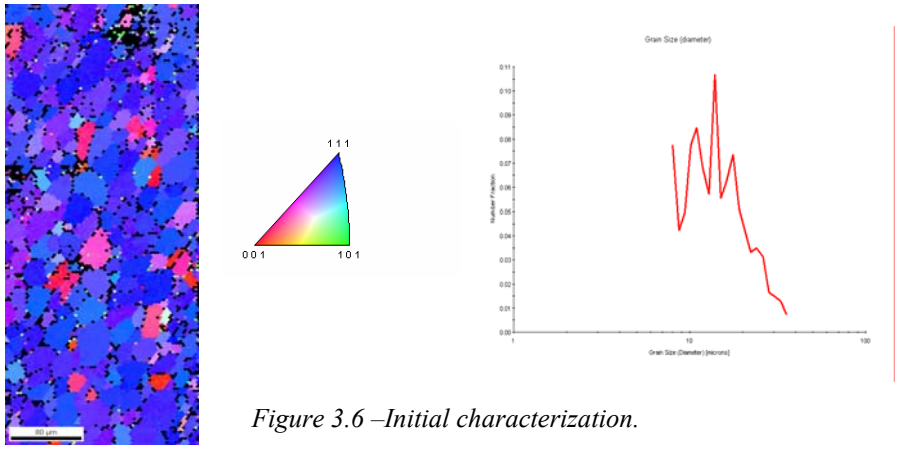

Figure 3.6 –Initial characterization.

Specimens of this material were subjected to two different types of tests. The first imposed only a hydrostatic pressure, with no shearing applied. These specimens were used as controls to determine the amount and distribution of plastic deformation suffered by the specimens during imposition of the hydrostatic pressure alone. The second set of tests involved shearing the specimens to strains on the order of 1-4 while subjected to a given hydrostatic pressure. For the sheared specimens an angular rate of 0.3 degrees/min was imposed using the ram rotation as the control signal.

3.3.1.2 Hardness measurements

Measurement of microhardness profiles across the specimen diameter is a way that dislocation activity during hydrostatic loading can be analyzed, as mentioned in the Chapter 2. A Vickers hardness apparatus was used to measure the point-to-point variation in mechanical properties of the samples subjected to pressures of 4 GPa, The load used in taking the hardness measurements was 100 grams.

The microhardness measurements were done using steel holders as the substrates for the deformed specimens. The specimens were glued to the holders and pressure was applied in order to flatten the surface making it suitable for analysis. Hardness measurements were made every 0.5 mm from side-to-side across the specimen, the results are shown in Figure 3.7. It is evident from Fig. 3.7 that the samples subjected to loading show no hardening effects due to the superimposed pressure, the original value was estimated to be 102±3 GPa, and after loading equal to 108± 7GPa, the two values being the same within the experimental error when measuring hardness.

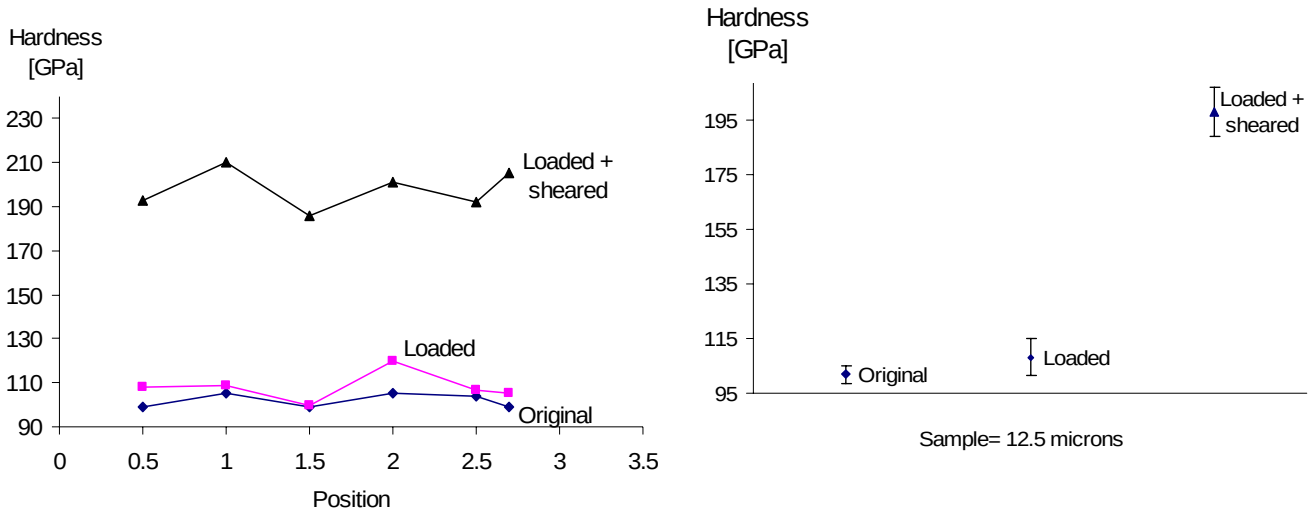

Figure 3.7 Hardening effect due to the pressure applied

On the contrary, the samples sheared after loading show values of 197±9 GPa, an evident increase in hardness close to 82%. These values of hardness corroborate that the stress-strain response is a measure of the strength of the specimens held under pressure and not an effect of deformation prior to the straining of the material.

Direct microstructural observations were made using automated EBSD and TEM techniques to study the dislocation activity during the deformation process.

3.3.1.3 Orientation imaging microscopy analysis

For the EBSD analyses, the samples were prepared in two ways to analyze both the normal surface and the cross section of the samples. To examine the cross section the samples were mounted in a transparent resin so that suitable cross-sections of the foils could be prepared. The samples were cut approximately along the slip direction with the cross section of the sample exposed for characterization. In both cases the exposed surface was prepared using standard metallographic procedures. Color coding of the

orientations is indicated by the orientation color key shown with poles normal to the foil surface being represented (horizontal on the images shown).

Figure 3.8 contains orientation images of the cross-sections and normal surfaces for the original foil (a), for a specimen loaded to 4.0 GPa and unloaded (b) and of the specimen deformed to an average shear strain of 3 read by the extensometer.

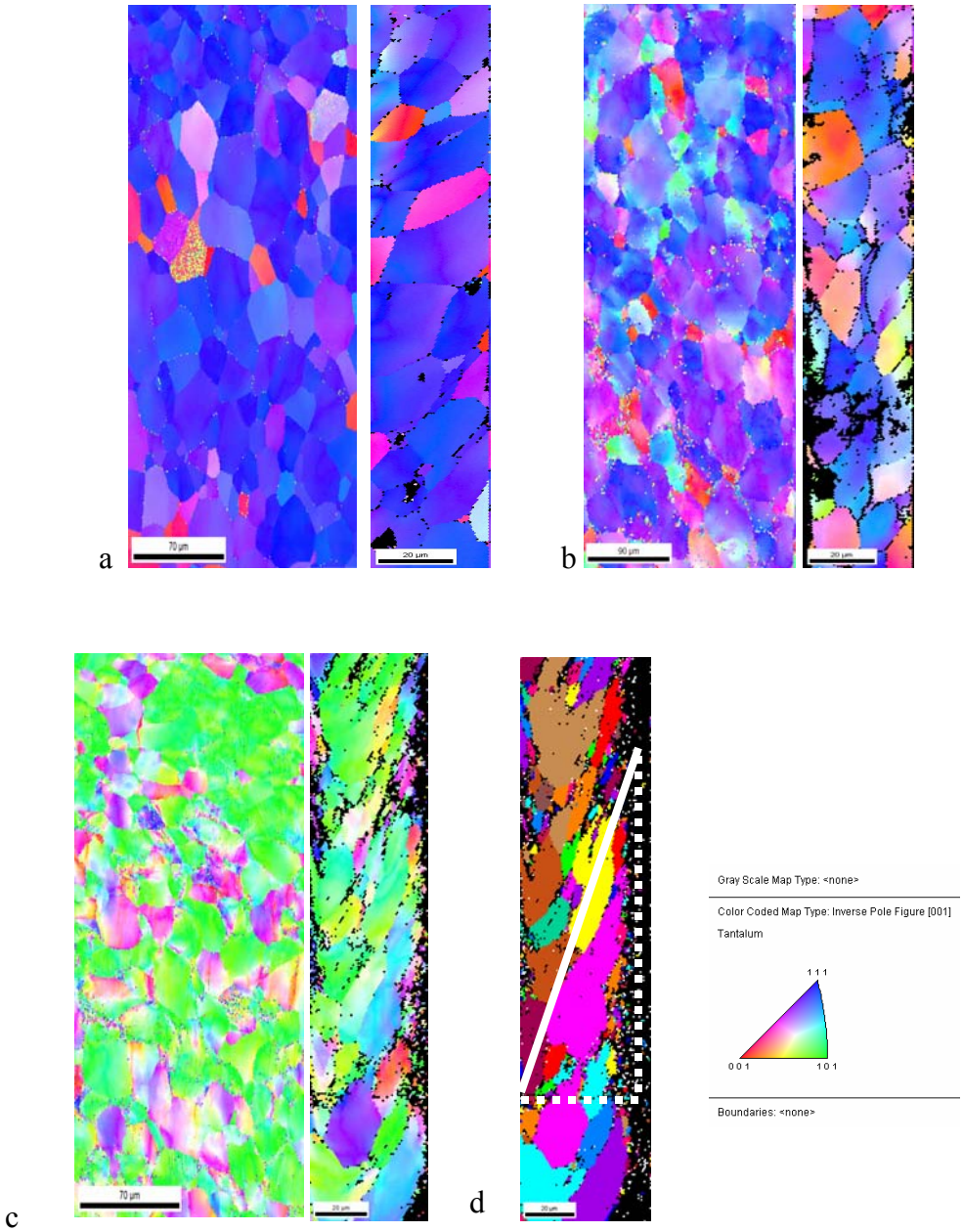

Figure 3.8 – OIM analysis of the cross section showing the grain behavior of the specimen subjected to 4.2 GPa a) Original specimen, b) held under high pressure, c and d) sheared under pressure.

Figure 3.8a shows the orientation images of the original specimen. The grains are well shaped and defined, and a {111} texture is evident. Figure 3.8(b) shows a similar microstructure as the undeformed specimen, no significant deformation can be appreciated for these specimens that were subjected to a normal pressure of 4 GPa. These results indicate that the deviatoric components of the applied stress are below the shear stress for tantalum, close to 50 MPa. Figure 3.8c shows the microstructure of a specimen sheared under a pressure of 4 GPa. The grains appear sheared and elongated along the slip direction and a developed {101} texture due to slip (to be proven by VPSC simulation of the texture evolution) is also evident. These results are consistent with the values of hardness obtained for loaded and unloaded at 4 GPa, where there is no significant change in the microhardness and thus no change in the microstructure of the sample due to activation and interaction of dislocations.

A unique grain color map was also created for the sheared specimen. In this type of map color is assigned randomly to each of the grains in order to differentiate them from each other. From this map an approximate amount of strain can be indirectly extracted. In the case of the tests done at 4.2 GPa, a nominal strain of about 3.2 was read by the extensometers. Measuring the strain from the orientation image, using the observed shearing direction (indicated by a solid white line in Figure 3.8(d) yields a strain of 3.0. This result gives assurance that the measurements taken by the extensometers, using the assumption that the specimen surfaces stick to the deformation anvils approximates the actual strain experienced by the specimen.

3.3.1.4 Transmission electron microscopy

To study the dislocation activity in detail both deformed and undeformed specimens were analyzed by bright field imaging in the TEM. Reported here are the results for specimens loaded to a pressure of 4.0 GPa.

Figure 3.9a shows the BF image of the original Ta foil that was used for the tests. No appreciable dislocation density prior to the deformation process is observed. For the specimen loaded to a pressure of 4.2 GPa without shearing (shown in Figure 3.9b), a slight increase in dislocation content is observed, but the grains are still relatively free from dislocation debris. This explains why the measurements of the hardness in the specimens loaded and unloaded without shearing were close to those obtained for the undeformed specimens. It also helps to interpret the orientation images where some slight in-grain lattice distortion is observed due to the geometrically necessary component of the dislocation structure.

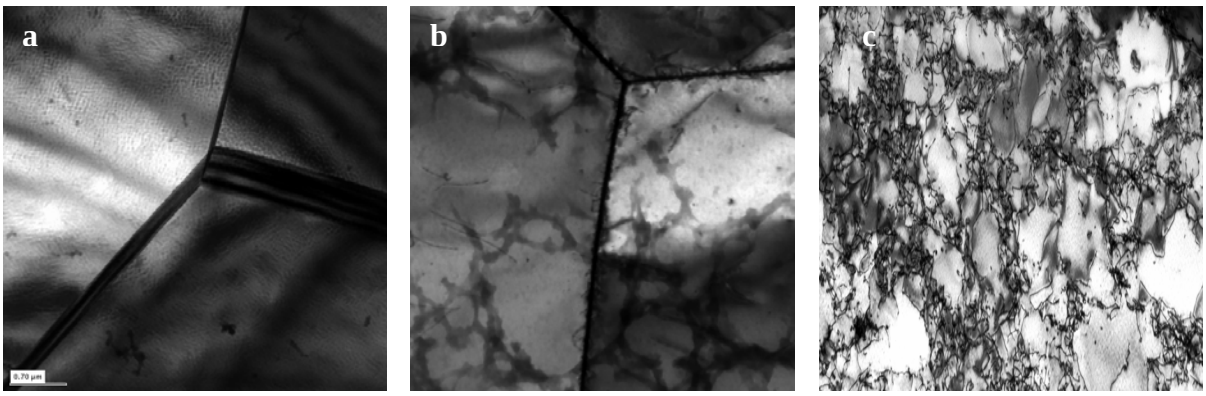

Figure 3.9 TEM analysis of the samples at 4.2 GPa: .a) undeformed specimen b) specimen loaded and unloaded with no shearing, and c) specimen loaded and sheared.

These results show that while some dislocation motion occurs near the specimen centers during loading of the specimens, the crystallites remain largely undeformed. The structure therefore must undergo primarily elastic strain during loading to high pressures.

For the specimens loaded to high pressure followed by shearing (Figure 3.9c), the TEM images show that the specimen contains a well-developed dislocation network. The TEM images of the specimens of both types of deformation are consistent with the observations obtained using hardness and EBSD techniques.

3.3.2 Pressure distribution

The second issue to be addressed is the pressure distribution within the specimen when using an opposed anvils set up. As it is found in the literature, many investigators have attempted [20-25, 94-96] to determine the pressure gradients that exist under static conditions (not rotating). This can be thought as a lower pressure analogous to the DAC, where very large gradients can be measured in situ [6]. The main conclusions from these studies are:

- Pressure gradients of the order of 0.4 GPa/mm frequently occur.
- The pressure at the center of the anvils may be greater or less than the nominal applied pressure.
- Greater pressure is due to a phenomenon called the multiplication effect. This effect is a function of the ratio of diameter to thickness, where the higher the ratio the lower the effect.

- The pressure at any radial position is proportional to the nominal pressure.
- There is a peripheral region around the outside of the specimen in which the pressure drops very rapidly. These studies claim that because of this, as much as 50 % of the sample area may be non-load-supporting.

The first issue to be attacked is the multiplication effect, as it has been reported by Myers [94-95], this effect can be neglected by choosing a proper diameter to thickness ratio, in their study it was found that for ratios larger than 16:1 there was not a significant pressure intensification. As it was mentioned before, the dimensions of the samples to be used in this study are 3 mm diameter and 50-12.5 μm in thickness which give ratios of 60 to 240, well above the 16:1 proposed by Myers.

The next issued is to find the pressure gradients that may exist in the sample. All the observations stated above were for static conditions, in our case the loading step of the experiment. Once the anvil starts rotating or in our case moving tangentially, the gradients developed are much more difficult to evaluate. Nevertheless in the literature [93] is found that by having a dynamic set up, as our case, the pressure distribution becomes more uniform.

These gradients can be minimized by designing/optimizing the geometry of the anvils. A similar study was recently carried out by Levitas and co-workers [98-99], their efforts focused on redesigning the geometry of the gaskets that were used in their dynamic (rotating) anvil cell (RDAC). Their results show that minor changes in the dimensions of the gasket, such as thickness and diameter, led to a more homogeneous

pressure distribution in the sample. Unfortunately, the main advantage of the DAC set up, which is that it allows *in situ* measurements of the pressure at any position inside the cell by means of x-ray diffraction, can not be implemented in the tri-anvil. Obviously in this case the anvils are not transparent to the x-rays. So in order to analyze how the pressure was distributed within the specimen during the shearing step, the only option we have is by following the same approach as before in which electron microscopy was used to study microstructural changes in the sample.

The initial geometry of the anvils consisted of having two flat surfaces as shown in Figure 3.10, the sample was compressed between these two surfaces.

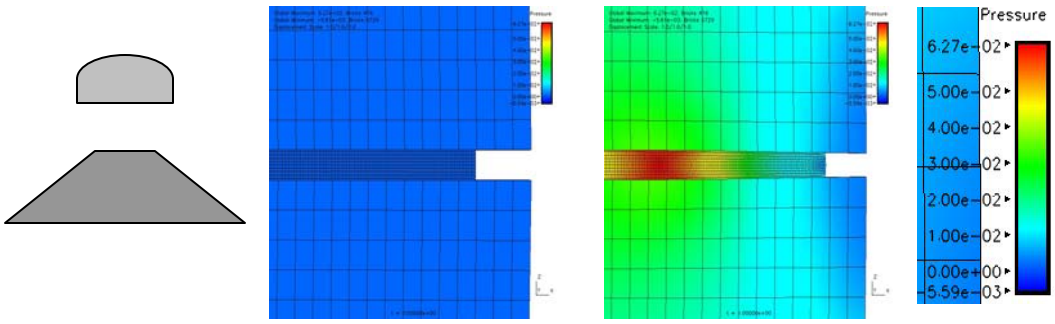

Figure 3.10 a) Schematic of the original anvil design, b) finite element simulation of the sample at 4GPa

A finite element calculation of this condition is given in Figure 3.10b, therein is shown that very close to the edge of the sample there is low pressure/stress-free region, as mentioned before this region can represent as much as 50 % of the total area.

It is possible to experimentally determine how much area is under pressure. Previous studies [94-97,] have used pressure induced phase transitions in materials such as bismuth as a way to investigate the areas that were subjected to a minimum threshold pressure. By measuring the transitions at different distances from the center of the anvil they were able to estimate the gradients that existed in the anvils. In our study we decided

to use a similar approach, but instead of phase transition of other materials, we used the texture evolution occurring in our sample. As it has been shown we have to impose a minimum pressure in order to have internal shearing in the material, this is given by $\mu \boldsymbol{P} = \tau$, where μ is the friction coefficient between anvil and sample and τ is the shear stress (pressure dependent) of the material, in our case the minimal pressure that we needed to apply was close to 3 GPa, for lower pressures slippage occurred. So by analyzing how much of the material was sheared we can determine the areas that were load-bearing. Tests were carried out at 4GPa and EBSD was performed on the surface of the samples, the result is shown in Figure 3.11b

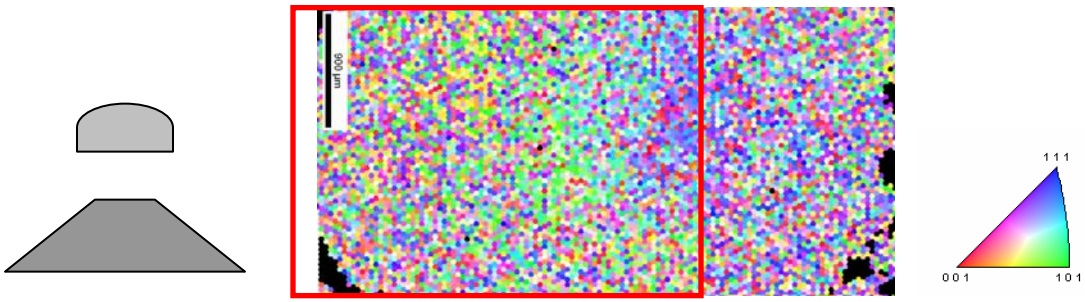

Figure 3.11 a)Schematic of the original anvil design used, b) EBSD of the sample sheared at 4GPa

It can be appreciated that the sheared area, which as mentioned before is given by the area that shifted from {111} to {101} texture, occupies a region that covers from edge to the center of the sample. The main reason for this effect is that at high pressure the anvils elastically deform giving the specimen a lens shape with higher strained areas at the edges. As we proceed to move the lower anvil, plastic deformation is being imposed in the edge-to-center direction, this shearing is highly directional with minimum or

almost no shearing taking place in the opposite edge. This condition is depicted in Figure 3.12

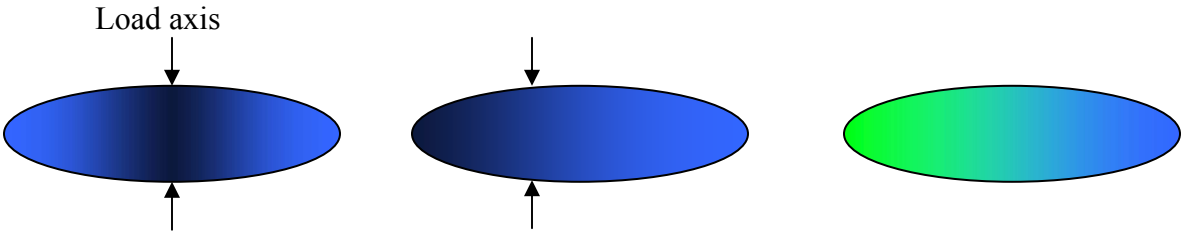

Figure 3.12 a) Symmetric pressure distribution, b)asymmetric pressure on deforming specimen, c)amount of deformation in a lens shaped specimen.

To avoid the problem of the anvils cupping after deformation, giving the sample a non-uniform thickness and therefore pressure gradients, several ideas were analyzed with the help of FEM. The goal was to have a uniform thickness throughout the major portion of the specimen held under pressure. Two approaches were investigated; starting with lens shaped specimens that will flatten out upon loading, or modifying the anvil geometry. The philosophy of the second idea is that at high pressure the anvils will reach a flat configuration providing the sample with an improved homogenous thickness/pressure. This new geometry is depicted in Figure 3.13a,

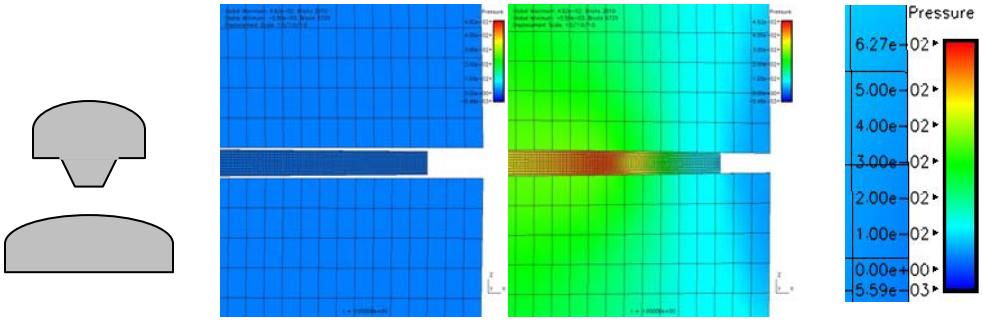

Figure 3.13 a) New anvil geometry, b)improved pressure distribution

It can be appreciated in the calculation depicted in Figure 3.13(b) that by reducing the exposed area of the upper anvil and by having a domed surface on the lower anvil a more uniform pressure distribution could be imposed on the sample.

To experimentally validate this new methodology, again tests were carried out at 4 GPa and post mortem EBSD was performed in the sheared specimens, a representative result is presented in the next figure (Figure 3.14).

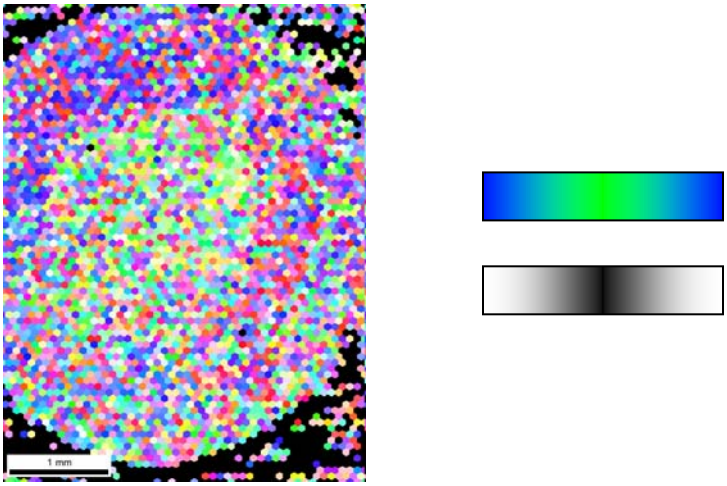

Figure 3.14 a) IPF of the sheared specimen, b)Schematic of texture (=pressure) distribution

It can be observed that in this case the deformation is taking place at the center of the specimen, so indeed the anvils are reaching a flat configuration that allows a radially symmetrical shearing of the sample, but this region is not covering the entire area of the sample. In Figure 3.14(b) is shown schematically that only the region that reached the minimum pressure was able to be sheared. At this point two anvil geometries were tested giving complementary results for the texture changes occurring in the specimens, again this texture change gives an indication of the pressure at which the specimen is being held. So the ideal configuration should be in between these two extremes already tested: flat – flat and a flat-domed geometries. The next step was to smoothen the dome of the

lower anvil. For this purpose a time-controlled mechanical polishing would give the best results, because the anvils were made out of WC, the polishing material chosen was diamond compound. The anvils were polished for time increments of 5 minutes, after each time increment the anvils were put back in the tri anvil device and shear tests were carried out at 4 GPa. For each test EBSD analysis was performed on the specimens, the results are shown in Figure 3.15.

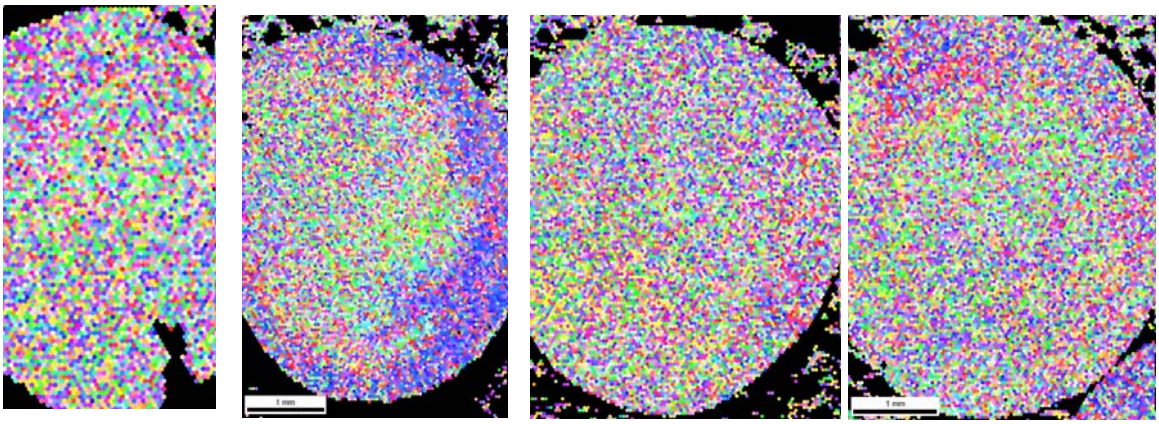

Figure 3.15 IPF of the sheared samples by using polished anvils a)5min, b)10min,c)15 min, d)20 min

It can be appreciated that the longer the domed anvil was polished the more area was able to be sheared, which in turn translates to more uniform distribution of the pressure.

The experimental characterization of the samples held under pressure, established that the procedure described herein represents a reliable method to impose nearly uniform hydrostatic pressure on the thin foil specimens. The developed hydrostatic stress assertion was validated indirectly by applying characterization methods and measuring properties such as hardness, dislocation density and microstructure evolution (texture development) for the specimens subjected to such pressures. All properties measured

after loading and unloading (with no shear deformation) were close to those from the original foils. The homogenous assertion comes from the measured texture developed in the specimen. As it was stated before, this shifting in texture is only possible in the regions that were held under enough pressure to avoid slippage of the anvil on the sample. After assuring in good confidence that the pressure attained was near a homogenous hydrostatic condition, specimens were deformed in shear to different pressure to analyze their mechanical properties as function of the superimposed pressure, details are given in the following Chapter 4.

Chapter 4

Tantalum results: Discussion of the deformation of Polycrystalline Ta

4.1 Mechanical Response: flow stress as function of Pressure.

As stated previously, the samples were prepared with a geometry of about 3 mm in diameter, and a mean thickness of 50 μm. Because each test requires a set of three samples (Tri anvil device), the load necessary to achieve a nominal pressure of 1 GPa was roughly 22.3 kN (5 kips). The tests were carried out with increments of 0.5 GPa up to about 50% of the capacity of the testing system which converts to a pressure of 4.5 GPa for the given sample size. The values for torque and bottom anvil displacement were recorded and converted to stress-strain by using the geometric values of sample/device, this behavior is presented in Figure 4.1.

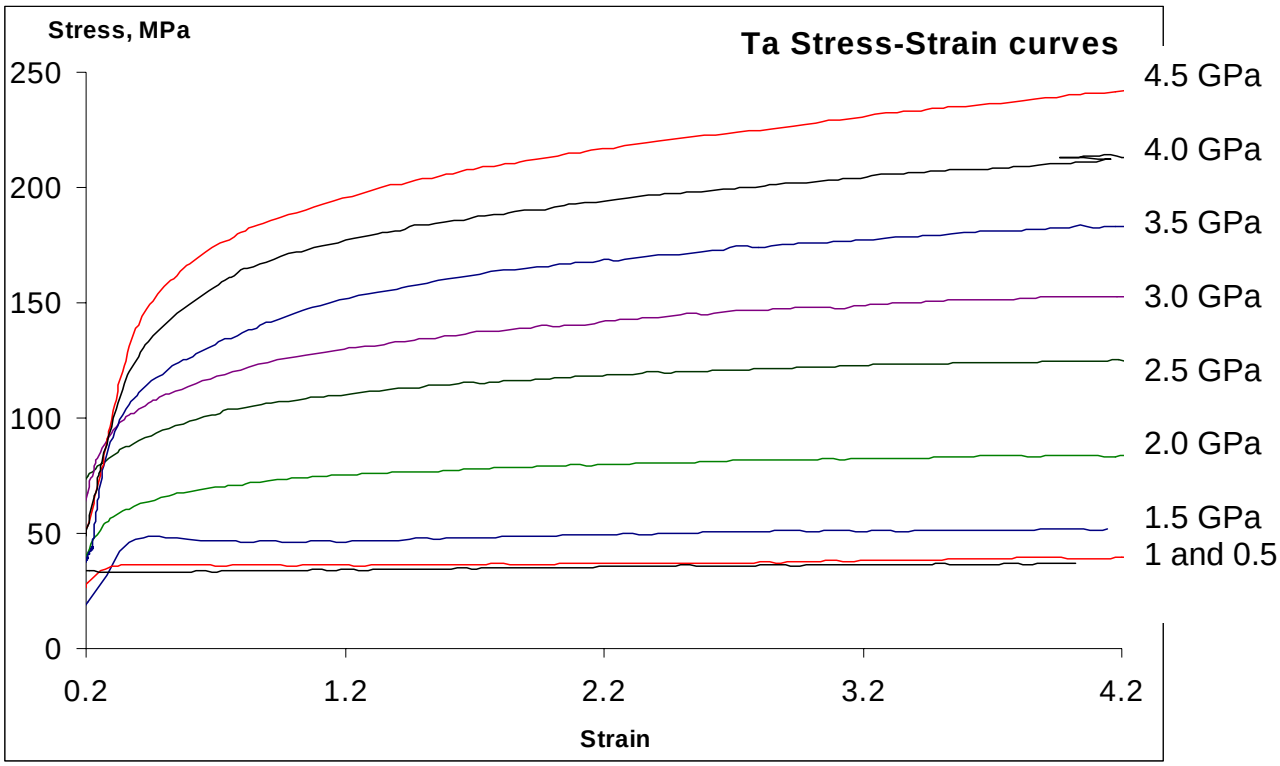

Figure 4.1 – Results of the effect of pressure on the stress vs. strain behavior of polycrystalline Ta foil.

These results are in agreement with the behavior observed by Bridgman using the rotating set up. As mentioned in the introduction section, it was anticipated that at low pressures slipping would occur between anvils and sample surface, this can be observed in Figure 4.2, the graph of stress vs. pressure.

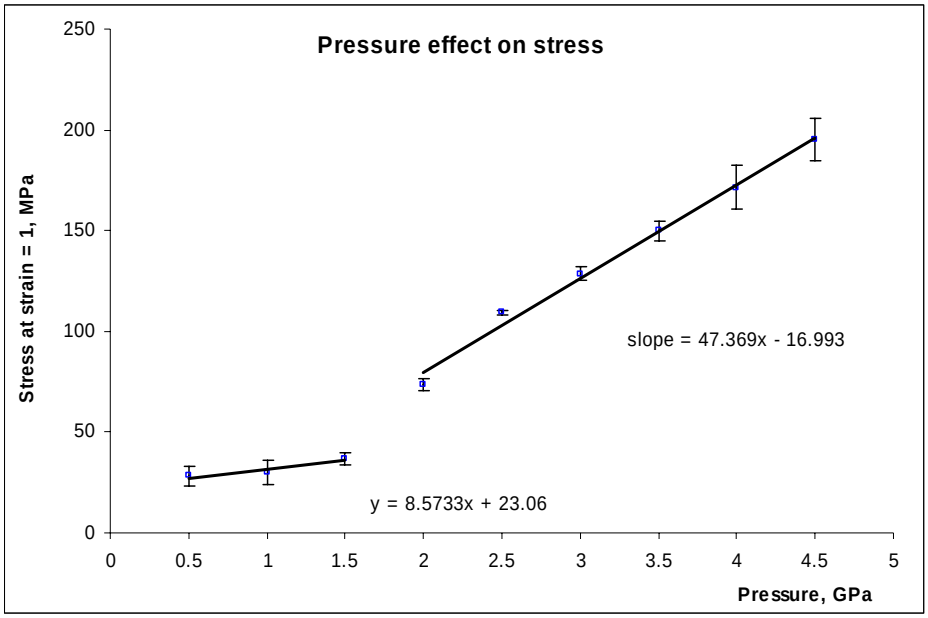

Figure 4.2 Flow stress vs. pressure at strain = 1.

This graph clearly shows that for pressure of 0.5 – 1.5 GPa the bottom anvil is just sliding on the surface of the sample. At pressures above 2.0 -2.5 GPa the anvils adhere to the surfaces of the sample and the movement of the lower anvil is accommodated through the internal shearing of the sample. As was also explained in the previous chapter, this sheared section was maximized by a change in the design of the anvils, so approximately the same area was deformed for pressures from 2.5 to 4.5 GPa.

After initial hardening, an intermediate zone is observed with a significantly reduced hardening rate, and a pressure-dependent inflection point. Finally, above a strain of 0.5 the material initiates a plateau zone (similar to stage IV hardening), which appears

to be a steady state work hardening region observed in the material. It is immediately apparent that the flow stress behavior is a strong function of the imposed pressure.

In the introduction section several yielding criteria were introduced, the results presented here surpass any predicted value for the flow stress for Tantalum subjected to pressure. In order to understand the underlying mechanisms responsible for these high values of stresses, it was necessary to investigate all the possible mechanisms occurring at the different size scales, Figure 4.3 shows the Multiscale Model that contains all the different scales that may give an explanation to the experimental results.

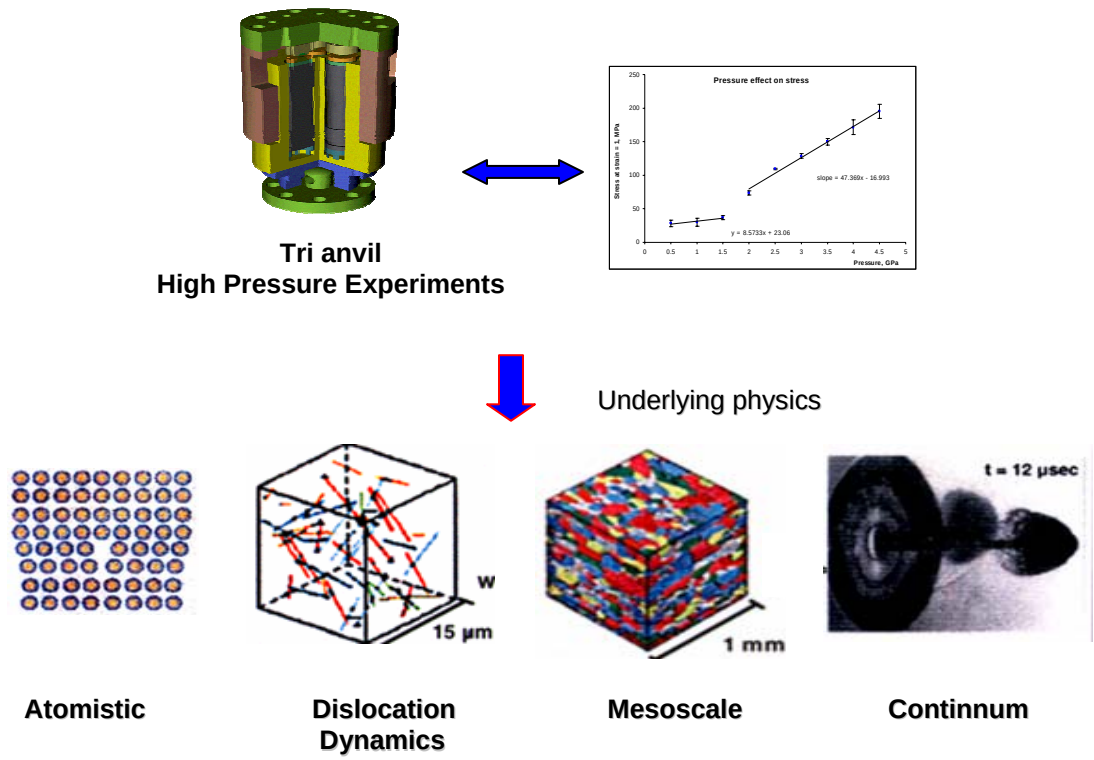

Figure 4.3 Multiscale model

Different characterization techniques were used to analyze the deformed samples, and when possible the results were validated with an associated simulation tool that operates in the same size scale.

4.2 Continuum approach

The first approach to understand how pressure changes the mechanical behavior of materials was to follow a continuum-type formulation. The formulation that was introduced by Steinberg and Guinan [60-62], details given in the Introduction Chapter, is the chief among the elasto-viscoplastic constitutive models for materials under high pressure (and high strain rates). This model is the most commonly used in the hydrodynamic computer codes. In their model the pressure dependence of the yield strength is found to be proportional to the shear modulus in the form

$$\frac{1}{Y_0}\frac{dY}{dP}\Big)_0 \approx \frac{1}{G_0}\frac{dG}{dP}\Big)_0$$

$$Y = Y_0 * \left[1+\beta(\varepsilon_i+\varepsilon)\right]^n * \left[1+\left(\frac{Y_P'}{Y_0}\right)\frac{P}{\eta^{1/3}}\right] \qquad (4.1)$$

From these equations a close linear relation between the yield strength and the applied pressure is expected. In addition, if the values of the parameters for polycrystalline Tantalum, Table 4.1 [61] are used in the constitutive Equations 4.1, the expected yield strength under different pressures can be calculated and compared with the values obtained experimentally.

Table 4.1 Steinberg - Guinan constants

Material	G_o [GPa]	Y_o [GPa]	Y_{max} [GPa]	β	n	G_p / G_o [GPa]
Tantalum	69	0.77	1.1	10	0.1	14.5

A deviation from the model is evident with discrepancies between the expected and the experimental values (see figure in Appendix A.7). These discrepancies are in

both the value and the behavior of the yield stress as a function of pressure, it is important to note that the experiment was done just after the limit in pressure studied by Steinberg-Guinan (≤ 2GPa). More evident deviation is that the model in the case of Ta predicts a small linear increase of about 3% in the yield strength but a more substantial increase is found experimentally, being of the order of 190% with pressure increased up to 4.2 GPa. These results tended to be similar to those of the work Bridgman [21-29], Weir [6] and other authors [100-101].

The measured yield strengths presented here, while much more affected than those predicted by the Steinberg-Guinan model, lie significantly below the maximum values for yield in Ta established by their investigations,

$$Y = Y_0 * \left[1 + \beta(\varepsilon_i + \varepsilon)\right]^n \leq Y_{\max} \tag{4.2}$$

where Y_{max} has been established to be 1.1 GPa [60-62] in the case of Ta, experimentally the values of yield stresses, although difficult to estimate are in the range of 50-150 MPa (Figure 4.1). From these results it was obvious that it was necessary to explore within the other scales such as the mesoscale, the microscale or even the atomistic scale.

4.3 Atomistic approach

Because of the great wealth of studies available on the dislocation behavior in the atomistic size scale we switched our efforts to this type of investigation. Emphasis was put on studies that contain high pressure as one of the variables when studying dislocation mobility in Ta and Mo. Most of the research is in the form of simulations/calculations. An experimental counterpart could be the use of High

Resolution Transmission Electron Microscopy (HRTEM), but as to date this possibility has been neglected or ignored.

Most of the simulation efforts can be divided in three major branches: first principle calculations, Monte-Carlo simulations (MC) and Molecular dynamics simulations (MD). Among the three options, the best suited tool to our conditions was the Molecular Dynamics approach. Only the first stages related to the relaxation process were able to be performed. Fruitful discussions with experts in the area such as Dr. Hoagland and Dr. Argentine (?) (LANL), Dr. Wolf (INL) and Dr. Bringa (LLNL) led to the conclusion that any result obtained through this technique would not be helpful to explain the experimental results, mainly because of the low strain rates used, the time range and the pressures reached in the tri-anvil device. Experimentally we had $\dot{\varepsilon} \le 1, \boldsymbol{t} \approx 1\min, \boldsymbol{P} < 5\,\boldsymbol{GPa}$, while MD uses $\dot{\varepsilon} \ge 10^5, \boldsymbol{t} \le 10\boldsymbol{ns}, \boldsymbol{P} > 50\,\boldsymbol{GPa}$. Nevertheless herein are presented the most important results obtained by different authors that could provide any insight in explaining how the pressure affects the properties.

From these studies the following conclusions can be drawn:

(1) The confining pressure has an appreciable effect on defect nucleation behavior. Increase of pressure will not facilitate the nucleation of twin; instead, dislocation may be nucleated by shear in a twinning system. Hydrostatic tension promotes twin nucleation.

(2) The yield strength of twinning shear increases monotonically with increasing confining pressure.

Based on these results obtained through atomistic simulation we encountered the disjunctive to have either dislocation gliding or twinning, with the pressure being the key factor to have either one of them. In the following two sections are described the efforts we pursued to elucidate the mechanism that was responsible and a plausible explanation for such increase in the flow stress.

4.4 Mesoscale (Grain size scale)

EBSD analyses were performed on the specimens deformed using the original flat-flat anvil configuration introduced in Chapter 3. Although later on it was concluded that original anvil set up caused some regions of the specimen to be low or non load-bearing and therefore minimum deformation was occurring in these places. The results obtained at the time were striking because they showed two different textures for the samples sheared to the same strain but held at different pressures.

Figures 4.4 show the microstructure of the original sample and deformed samples

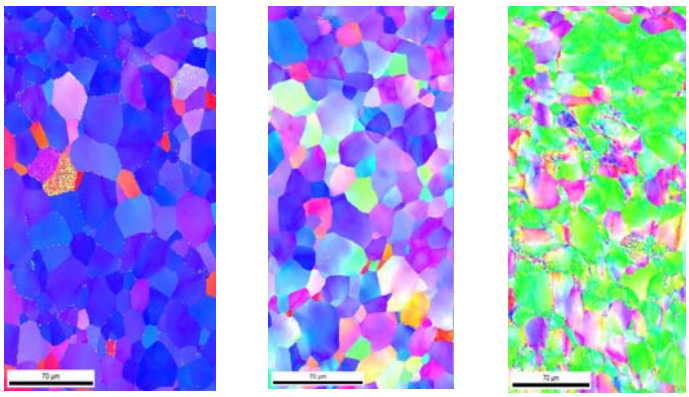

Figure 4.4 Microstructure of Ta samples(a) Original annealed (b) sheared at 2 GPa (c)sheared at 4GPa

As it was mentioned in the experimental development (Chapter 3) and shown in Figure 4.11 (a), the original microstructure of the starting material consisted of a mixture of strong {111} with a little component of {100} textures. After deformation two different textures were present in the specimen subjected to different pressures, a weak {101} (or a strong {121} texture, the other slip system available in BCC) at 2 GPa and a strong {101} texture at 4 GPa.

Our first hypothesis was that the specimens underwent different deformation mechanisms, in particular slipping at low pressures and twinning at higher pressures. A study by Hsiung and Lassila [102-104] shows that twinning occurs in Tantulum under shock conditions, where pressures close to 35 GPa are necessary to activate the twinning mechanism. These are normally accompanied by a phase transformation from BCC to the omega phase (HCP structure). Nevertheless tantalum is known to have strong stress localization [103], and it has been reported that by adding a shear stress to a superimposed pressure the Transformation Pressure (TP) decreases by a factor of 2 times in Iron based materials [105-106], so both twinning and phase transformation were considered as possibilities.

In order to study the mechanisms responsible for this dramatic change in texture, an investigation of the grain interaction/deformation-rotation sheared to high strains was necessary. We opted to use the Visco-Plastic Self Consistent (VPSC) Model developed by Dr. Tomé and coworkers [90,91].

The code was provided and installed on our facilities, as it was explained in Chapter 2 a program was necessary to convert our data to the necessary input files

required by the VPSC program, in specific it requires the conversion from grains to weighted average orientations. An example of the transformed microstructure is given in Figure 4.5

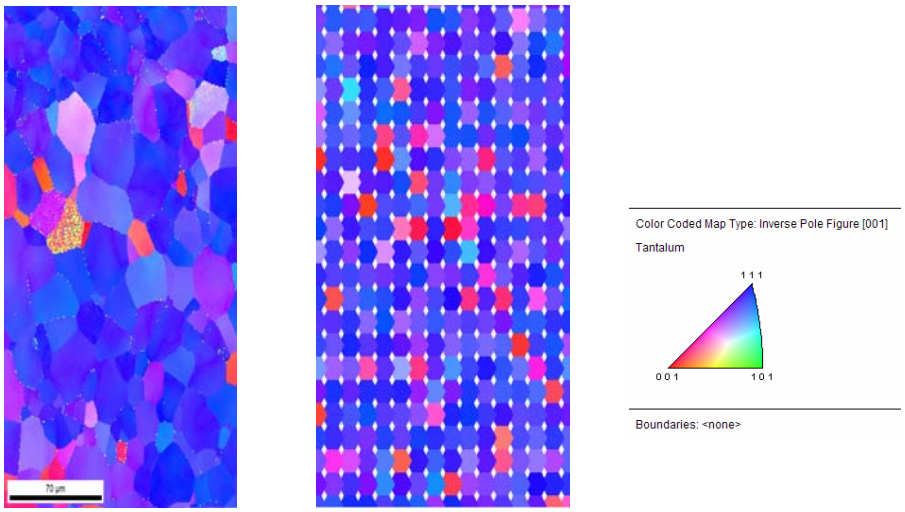

Figure 4.5 Microstructure of Ta (a) Experimental (b) Idealized

The weighted fraction of each orientation on the idealized structure is calculated by dividing the number of measurements that lie within one grain (defined by the OIM software), over the total number of measurements in the scan. So we input the experimental microstructure tested the two hypotheses we had. Figure 4.6 shows the results for the two different mechanisms.

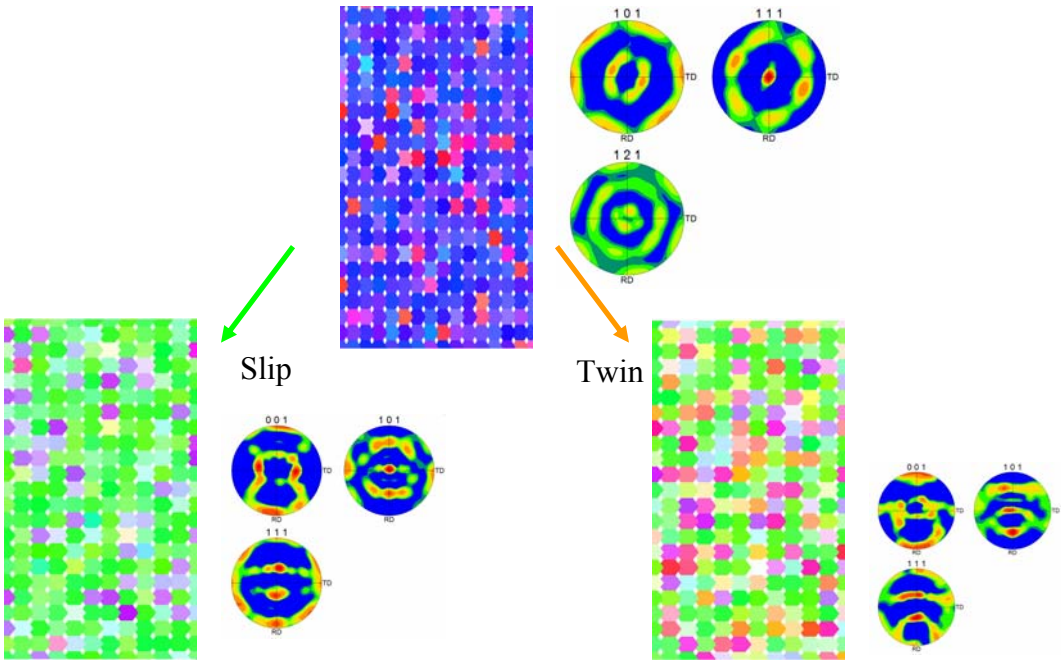

Figure 4.6 Microstructure of Ta (a)Original (b)obtained by slip (c) obtained by twinning

At the same time we had performed the changes of the anvil setup from flat-flat to domed-flat anvils and run an EBSD scan on the whole sample. The results are presented in Figure 4.7 for the cases of 2 and 4 GPa. It was found that the samples experienced the same texture development from {111} to {101}.

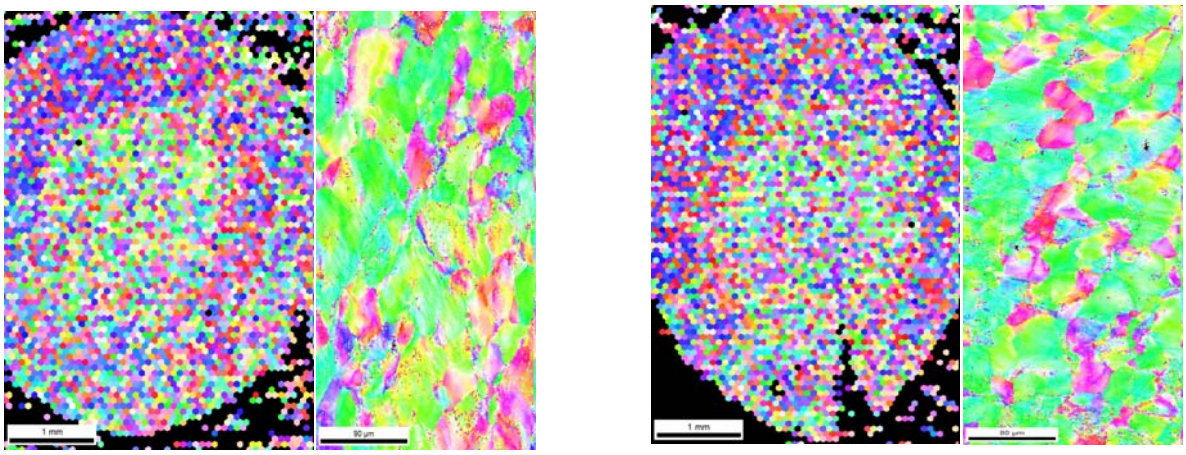

Figure 4.7 Microstructure of Ta sheared at (a) 2GPa, (b)4GPa

These results (along with TEM evidence that will be described later) indicate that the samples were deformed mainly by dislocation glide with twinning found not to be a major factor, or a factor at all. It is important to note that the specimens are deformed by dislocation activity occurring on {101} as the principal slip plane but also on {121} planes and to a lesser degree, {123} planes. This is typical for BCC.

In the light of these results, we concluded that any explanation for the increase in hardening due to the pressure should be a result of dislocation-based mechanism acting in the microscale.

4.5 Microscale approach

Based on the amount that imposed pressure causes an increase in each individual dislocation based mechanism we should expect the flow stress to increase between 5-10% when we double the pressure from 2 to 4GPa, but as we have seen the increase is much higher. By studying the microstructures at the dislocation level by using Transmission Electron Microscopy we should be able to determine the details of the dislocation activity. This effort was complemented by performing DD simulations with the implementation of the change in individual properties due to pressure effects on the interaction forces.

4.5.1Transmission electron microscopy

As it has been explained in the experimental section, one of the ideas behind the design and implementation of the tri-anvil experiment was that it would provide samples that required minimum preparation in order to be suitable for post mortem analyses. In the case of TEM analysis, the samples recovered after deformation were prepared in such way that the central part of the specimen was TEM- transparent. Deformation substructures of the samples deformed at room temperature under different confining pressures have been examined and studied in order to elucidate the physical mechanisms of dislocation multiplication and motion. Figures 4.8 show the microstructure of the samples that were deformed while held at a pressure of 2GPa.

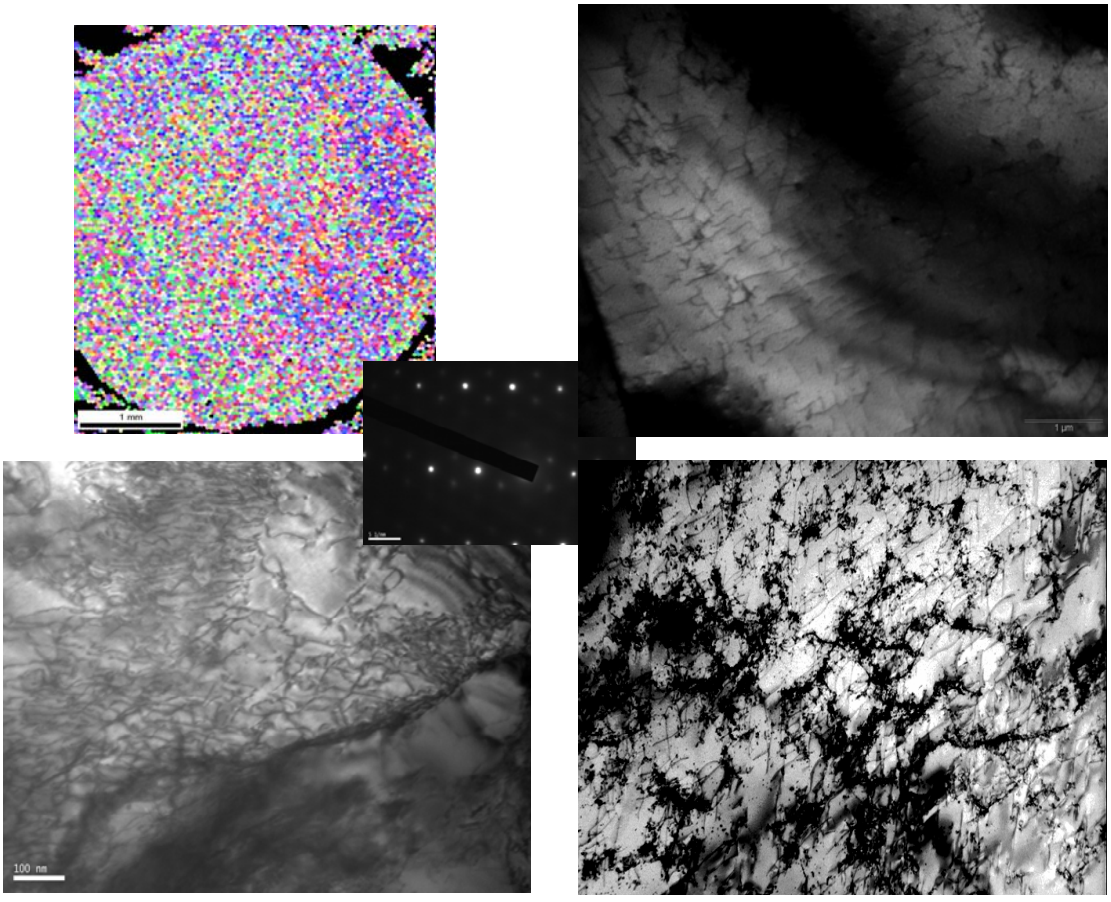

Figure 4.8 Dislocation structure for samples deformed at 2 GPa..

Figure 4.8 (a) shows the central part of the specimen that contains a developed {101} orientation in most of the grains, as it has been determined this is the texture that results after a shear deformation. Figure 4.8 (b) is a diffraction pattern of one the grains residing in this area, this DP confirms that the grains being analyzed under TEM correspond to a <101> normal. Figures 4.8 (c-e) show that the dislocation density is mainly formed by dislocation with screw character. Physical mechanisms for dislocation multiplication as well as dipole formation under different conditions have been discussed by several authors in particular by Rhee et al [92]. In their study with the help of Dislocation dynamics, they were able to establish that the multiplication of dislocations in BCC Mo resulted from sources that form in the initial stages of deformation, these sources are in the form of grown-in superjogs and can move, coalesce and pin each other under stress. Screw dislocations produced by such sources form a cross-grid microstructure characteristic of bcc metals.

These results confirmed that the deformation is mainly due to dislocation activity, no twinning was observed and the microstructure is the one expected for this material.

For the specimens deformed at a pressure of 4 GPa, we used the same electropolishing procedure for preparing the specimens. Figures 4.9 show the microstructure obtained for different specimens deformed while held at 4GPa. Figure 4.9(a) shows again that the samples developed a {101} texture, again this orientation is confirmed by the diffraction pattern obtained from one of the grains in the deformed microstructure. Figures 4.9 (c-e) show a totally different microstructure from the ones

obtained under 2 GPa, in this case the dislocation structure consists of well developed dislocation cell walls. In some cases as shown in Figure 4.9 (c) the interior of these cells was completely free from dislocation debris. The cells were on the order of 100-200 nm wide while the length extended several hundreds of nm, almost to the micron scale.

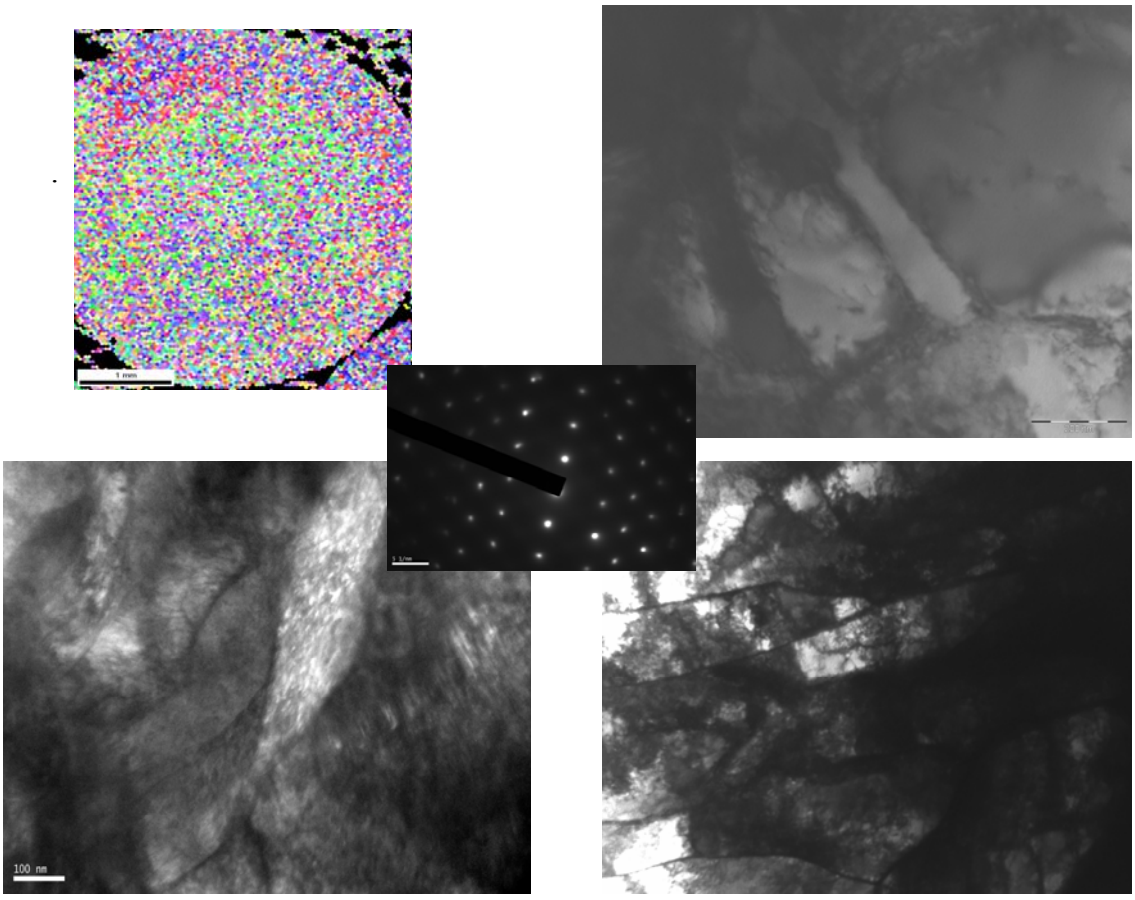

Figure 4.9 Dislocation structure for samples deformed at 4 GPa..

In other cases and by tilting the samples it was possible to image dislocation segments, by using a single tilt TEM we studied the character of these walls. Figure 4.9(a) shows an example of the developed cell network, inside the sub-grain some segments can be appreciated and by using the smallest aperture we could select the area

enclosing two of these segments. By tilting the sample with respect to the incident beam we were able to perform approximately the invisibility condition for one of the segments.

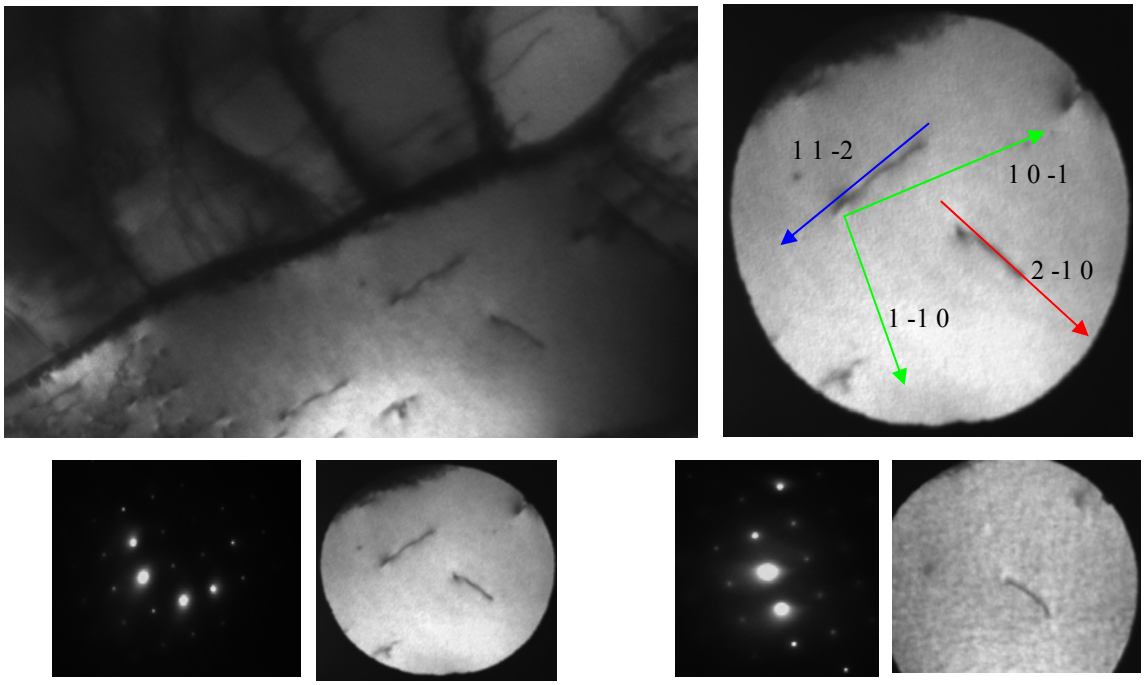

Figure 4.10 Dislocation structure for samples deformed at 4 GPa..

So after comparing the diffraction patterns with the ones given in Williams and Carter textbook, and by applying geometrical relationships, the line direction was calculated to be < 11 -2>. As we know the Burgers vector should be parallel <1 1 1>, in this case the same as the **g** vector. The dislocations trapped correspond to pure edge segments. Again the dislocation cell walls are approximately parallel to the calculated reference frame (in green), so for this particular image the dislocations can go either in or out of the plane, a schematic of this is given in Figure 4.11.

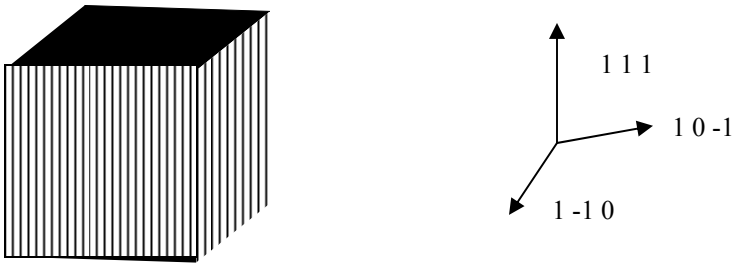

Figure 4.11 Schematic of the dislocation cell formed at 4 GPa.

.

The dislocation cells are the product of the coalescence of screw dislocations that came and stayed together as a response to the external stresses. This phenomenon could account for the increase on the flow stress for different pressures. As the pressure is being increased the dislocation should be more prone to form these dislocation walls, limiting the mean free path for dislocation motion. The question still remained of how the pressure affects this tendency to form dislocation substructures.

There is little documented evidence of this is phenomenon. A study by Tokii[107] found that ordered substructures were observed in the NB-Ti alloy at pressures as low as 1 GPa. In short terms they claimed that the structures are due to an increase in the dislocation interaction terms given by the form of Equation 4.10

$$f_r = \frac{b_1 b_2 \cos\theta}{2\pi r}\left[\mu + k_2 P\right] \tag{4.10}$$

This increase in the interaction forces accounts for the dislocations with opposite sign to be more easily annihilated and with same sign to stay together. Their results are presented in Figure 4.12,

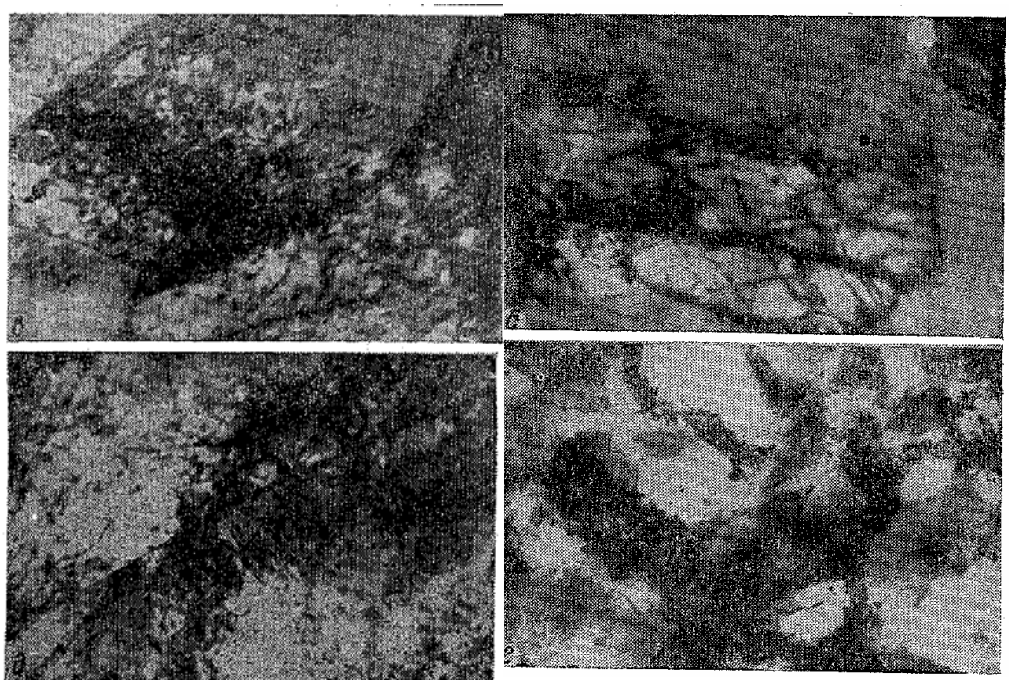

Figure 4.12 Dislocation structures formed on Nb-Ti alloy (a) 25% strain at no pressure (b)25% strain at 0.3GPa (c)60 % room pressure(d) 60% strain at 1 GPa .[107]

Their results are in qualitative agreement with those shown in this thesis. Figures 4.12 (a) and (c) correspond to our low pressure deformed structures where dislocations behave normally and Figures 4.12 (b) and (d) are similar to our 4GPa structures, when the effect on how the dislocations react to the imposed hydrostatic pressure is more noticeable.

Based on this evidence and the results obtained both by this research and by all the authors mentioned in the previous sections, the last step of this research was to simulate the behavior of the dislocation activity by using Dislocation dynamics. The plan was to alter the different parameters that appear to be affected by the pressure such as the mobility and the dislocation forces.

4.5.7 Dislocation dynamics

Numerous studies have shown that in the framework of linear elasticity theory there is no effect of the superimposed hydrostatic pressure on the forces acting on the dislocations [52-54]. Nevertheless, there is abundant literature on experimental studies [12-29,92,110-112] that contradicts this assertion, and indeed some properties such as mechanical behavior [21-29,100-101], differ under hydrostatic pressure from those carried out under normal conditions. Taking into account this experimental evidence, one may conclude that we shall look beyond the first order approximation (linear elasticity) model.

There have been authors such as Tokii [108-109] that studied the contribution of the pressure on the dislocation behavior by using a nonlinear elasticity approach, specifically they considered a quadratic approximation in the derivatives of the dislocation displacement. They started with the concept of the potential energy a body under isotropic pressure with distortion:

$$\Pi = \iiint_{v_0} A d\tau_0 + P \iiint_{V} d\tau \tag{4.11}$$

Where A is the specific potential energy of the distortion, $\iiint_{v_0} d\tau_0$ is the integral over the deformed body, and $\iiint_{V} d\tau$ is the integral over the undeformed body, in this manner the first term on the right side of Equation 4.11 represents the potential energy of the distortion and the second term, the work of the pressure. By using this concept and the

second order quantities in the displacement derivatives dU_i/dx_k they derived an expression for the dislocation energy in a hydrostatically compressed body.

$$\boldsymbol{E} = \boldsymbol{E}_s + \boldsymbol{E}_{p\varepsilon} = \int \left[\frac{\lambda}{2}\left(\boldsymbol{U}_{ii}\right)^2 + \mu \boldsymbol{U}_{ik}\boldsymbol{U}_{ik} + \boldsymbol{P}\aleph^3 \left(\frac{1}{2}\left(\boldsymbol{U}_{ii}\right)^2 + \omega_i \omega_i - \frac{1}{2}\boldsymbol{U}_{ik}\boldsymbol{U}_{ik} \right) \right] \boldsymbol{d}\tau_0 \quad (4.12)$$

In the left side of the equation E_s is the natural dislocation energy given by the linear elastic theory and $E_{p\varepsilon}$ is the energy resultant of the interaction of the strain field produced by the pressure and the dislocation field. As for the right hand side, λ and μ, l and n are the Murnaghan coefficients, the U_{ik} and ω_i are the deformation field displacement derivatives with:

$$U_{ik} = \frac{1}{2}\left[\frac{dU_i}{dx_k} + \frac{dU_k}{dx_i} \right] \qquad \text{and} \qquad \omega_i = \frac{1}{2} e_{ikl} \frac{dU_k}{dx_l} \quad (4.13)$$

$$\text{And } \aleph = 1 - \frac{P}{3\lambda + 2\mu}$$

By using the condition for the dislocation stress field $\int_{V_e} \hat{T} d\tau_1 = 0$ where $\int_{V_e} \hat{T} d\tau_1 = 0$ is the stress tensor produced by the dislocations, then, the energy is given by

$$\boldsymbol{E} = \int \left[\left(\frac{\lambda}{2} + \boldsymbol{k}_1 \boldsymbol{P} \right) \left(\boldsymbol{U}_{ii}\right)^2 + \left(\mu + \boldsymbol{k}_2 \boldsymbol{P}\right) \boldsymbol{U}_{ik}\boldsymbol{U}_{ik} \right] \boldsymbol{d}\tau_0 \quad (4.14)$$

where

$$k_1 = -\frac{P}{3\lambda + 2\mu}\left(\frac{1}{2}\lambda - \mu + 3l - m + \frac{1}{2}n\right)$$

and $$k_2 = -\frac{P}{3\lambda + 2\mu}\left(3\lambda + 6\mu + 3m - \frac{1}{2}n\right) \tag{4.15}$$

are coefficients in the expression for the change in volume associated with the dislocation. To obtain the equilibrium conditions for the dislocation in a hydrostatically compressed medium, the author used the concept of variational calculus.

Consider two dislocation interacting in a compressed crystal. The deformation tensor for this condition will be given by

$$U_{ik}^{\gamma} = U_{ik}^{I} + U_{ik}^{II} \tag{4.16}$$

where U_{ik}^{γ} is the deformation tensor of the dislocation. From 4.17 one can calculate the energy density of the dislocation I in the presence of the stress field of dislocation II, having both of them immersed in a compressed crystal.

$$\Phi = \frac{1}{2}\sigma_{ik}^{I}U_{ik}^{I} + \sigma_{ik}^{II}U_{ik}^{II} + Pk_1(U_{ii}^{I})^2 + Pk_2(U_{ik}^{I})^2 + 2Pk_1U_{ii}^{I}U_{kk}^{II} + 2Pk_1U_{ik}^{I}U_{ik}^{II} \tag{4.17}$$

where the second, the fifth and the sixth terms describe the interaction energy of dislocations I and II under pressure. Then by introducing

$$V_{ik}^{\gamma} = 2k_1U_{ii}^{\gamma}\delta_{ik} + 2k_2U_{ik}^{\gamma} \tag{4.18}$$

the energy of the dislocation I can be written as

$$E^I = \int \Phi d\tau_0 = \int \left(\frac{1}{2}\sigma_{ik}^I U_{ik}^I + \frac{P}{2} V_{ik}^I U_{ik}^I + \sigma_{ik}^{II} U_{ik}^I + P V_{ik}^{II} U_{ik}^I \right) d\tau_0 \qquad (4.19)$$

And in this case the equilibrium condition is $\frac{\partial}{\partial x_i}\left(\sigma_{ik}^{II} + P V_{ik}^{II} + \sigma_{ik}^{(r)}\right) = 0$ where

$$\sigma_{ik}^{(r)} = -\frac{1}{3}\left[\sigma_{ii}^{II} + (6Pk_1 + 2Pk_2)U_{ii}^{II}\right]\delta_{ik}$$

To find the interaction force of two dislocations, one has to calculate the work done by the stress field D_{ik}^{II} for the displacement of an element *dl* of the dislocation I by a distance δr

$$-\delta E^I = \oint_{D_1} f_i \delta x_i dl = \int D_{ik}^{II} \delta U_{ik}^I d\tau_0 \qquad (4.20)$$

where f_i is the interaction force between dislocations, $D_{ik}^{II} = \sigma_{ik}^{II} + P V_{ik}^{II} + \sigma_{ik}^{(r)}$, and $-\delta E^I = \oint_{D_1} f_i \delta x_i dl = \int D_{ik}^{II} \delta U_{ik}^I d\tau_0$ is the deformation tensor change of the second dislocation induced by the displacement δr.

By using the equilibrium condition one can obtain from Equation 4.19

$$f_i = e_{ikl}\tau_k \left[\sigma_{lm}^{II} + P V_{lm}^{II} + \sigma_{lm}^{(r)}\right] b_m \qquad (4.21)$$

Again in the case of *P=0*, one obtains the classical Peach –Koehler equation. One important point to be made here is that the superimposed pressure changes the magnitude

of force between the two dislocations. As it is really difficult to obtain a general solution, the authors considered various cases here are mentioned only two.

Case 1: A straight-line dislocation on an infinite cell: no effect. The dislocation energy in a compressed crystal does not depend on the dislocation location. Therefore no force is exerted on a straight-line dislocation, as was expected

Case 2: Two straight screw dislocations parallel to one of the axes with burgers vectors $\mathbf{b_1}$ and $\mathbf{b_2}$ separated by a distance r

$$f_r = \frac{b_1 b_2 \cos\theta}{2\pi r}\left[\mu + k_2 P\right] \tag{4.22}$$

The importance of Equation 4.22 is that, qualitatively, it is almost identical to the expressions obtained by Steinberg-Guinan [60-62], Jung [113] and several other authors. In all the studies the effect of the pressure was to have an effect on μ the shear modulus, and any increase in yield stress was directly obtained from the shear modulus. The difference now with our approach is that any change in μ should not be used directly to predict the flow stress at a given pressure but rather indirectly, it should be analyzed how any change (big or small) in μ could affect the dislocation behavior and eventually lead to an increase in the flow stress.

4.5.7.2Dislocation dynamics results

In previous simulations Frank- Read sources were introduced a priori, this as is well known, will lead to strain hardening on top of pressure induced hardening.

Nevertheless there is strong evidence (92,114-115) that propose that the sources will be created at some point if the dislocations are left to evolve naturally, where naturally means that their interactions are controlled by PK type forces.

For this purpose simulations were run by having initial configurations that resembled the experimentally observed microstructures of BCC metals, Figures 4.13 (a) and (b) show the typical structures found in BCC materials, as it has been documented, the microstructure consists of long screw dislocation segments that go either in one direction or form a cross-grid pattern.

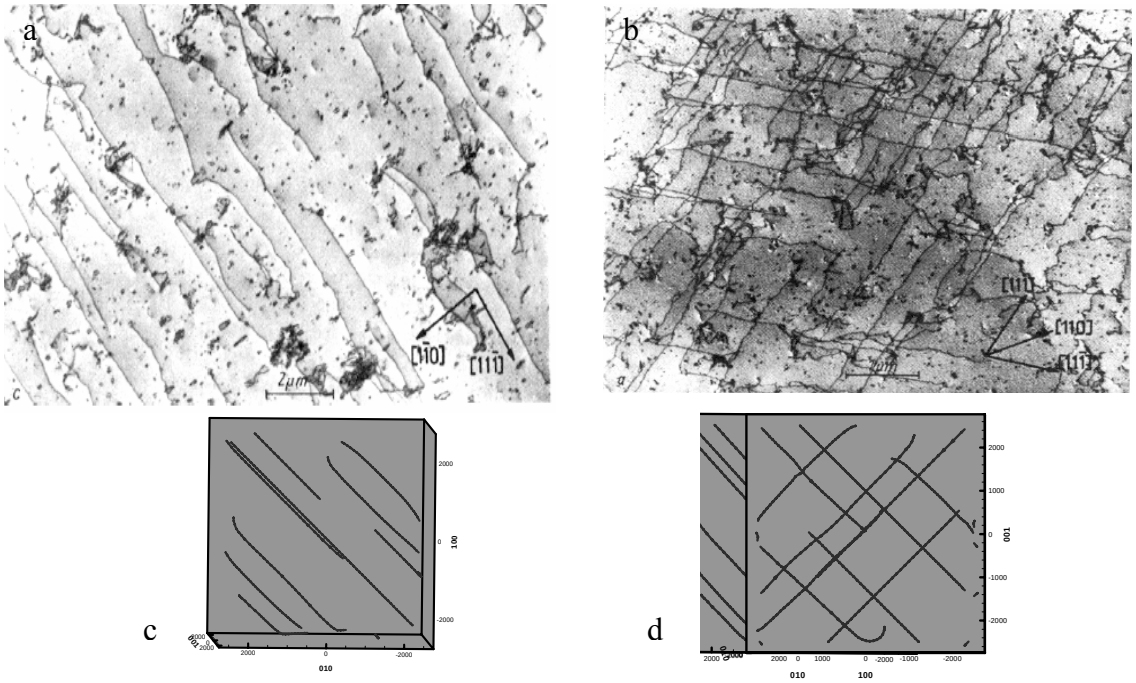

Figure 4.13 Initial dislocation structures (a) (b) experimental (c)(d) simulated[65].

The simulated configurations are shown in the Figures 4.13 (c) and (d), they were randomly assigned one of the {111} type of Burgers vector, the slip plane and the plane on which they were allowed to cross-slip, this was possible by modifying a subroutine in

the code and is given in the Appendix A7. For this set of numerical experiments, a strain rate of 6 in the ε_{13} direction was used and the simulations were performed at room temperature.

The configuration with dislocations consisting of segments oriented in one direction showed a cell formation in the corners of the simulation cell upon shearing. After discussion it was concluded that the final configurations were the result of numerical instabilities of DD code.

Figure 4.14 shows the resultant microstructure of the cross grid configuration with no changes in the PK terms.

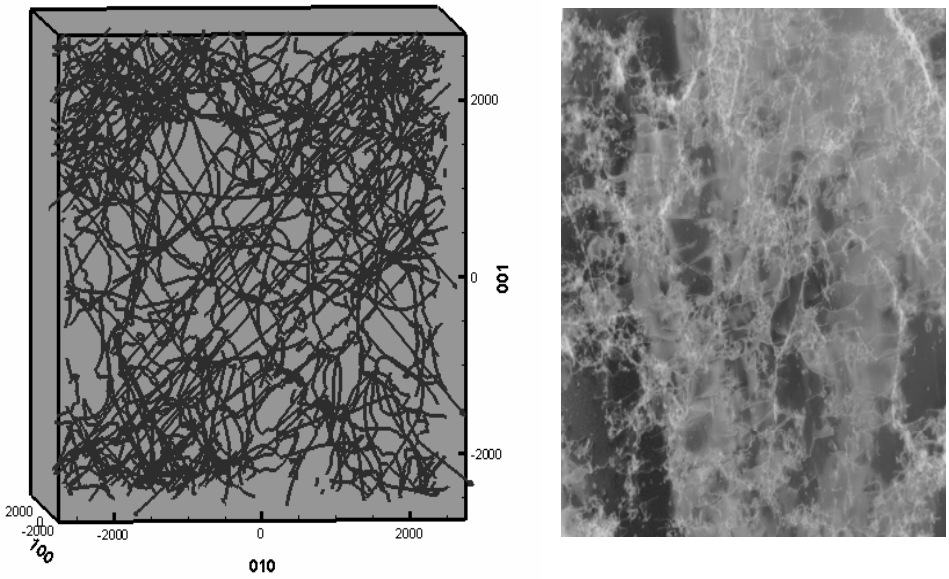

Figure 4.14 (a) DD results of PK original (b)TEM micrograph of a Ta sample deformed at 2GPa

Figure 4.15 shows the resultant microstructure of the cross grid configuration when the Peach-Koehler term was changed due to the effect of the pressure

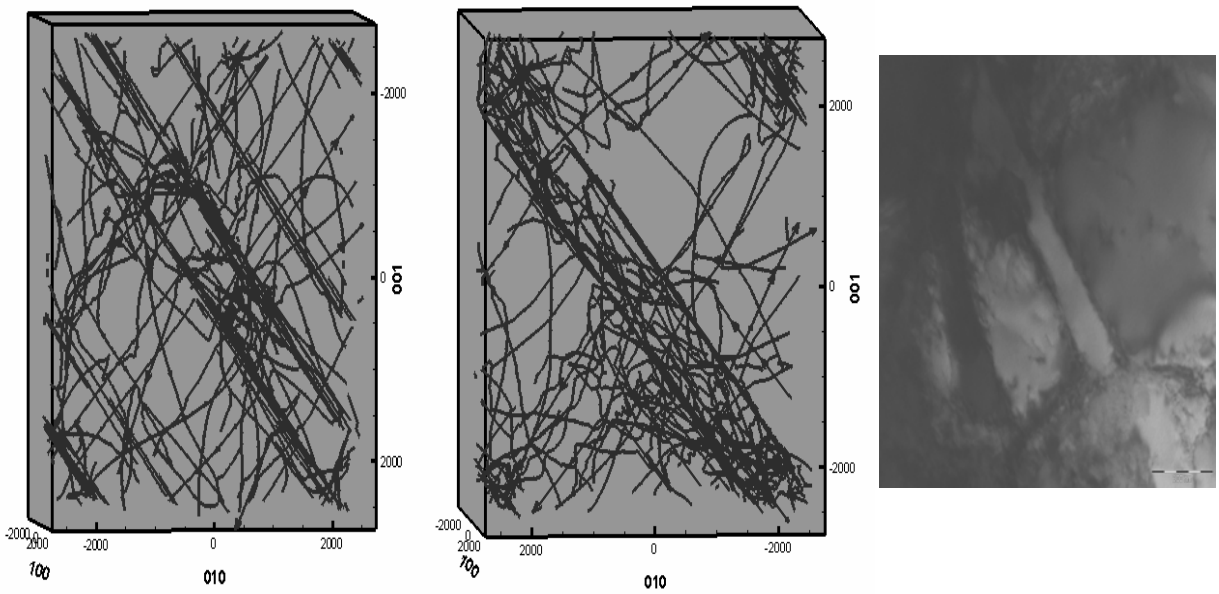

Figure 4.15 DD showing the results of changing PK force by (a)+50% (b)-50% (c)TEM micrograph of a Ta sample deformed at 4GPa

When comparing the final microstructure of Figure 4.14 (a) and Figures 4.15(a-b) it is evident that the superimposed pressure plays a key role on the dislocation "natural" evolution. By changing the PK term there is an enhancement in dislocation annihilation and coalescence, the simulated dislocation arrangement resembles, in some degree, the experimental microstructure Figure 4.15(c). Figure 4.16 shows the stress strain response of the simulations cells, it should be noted that all the samples were subject to the same final deformation of 1 %

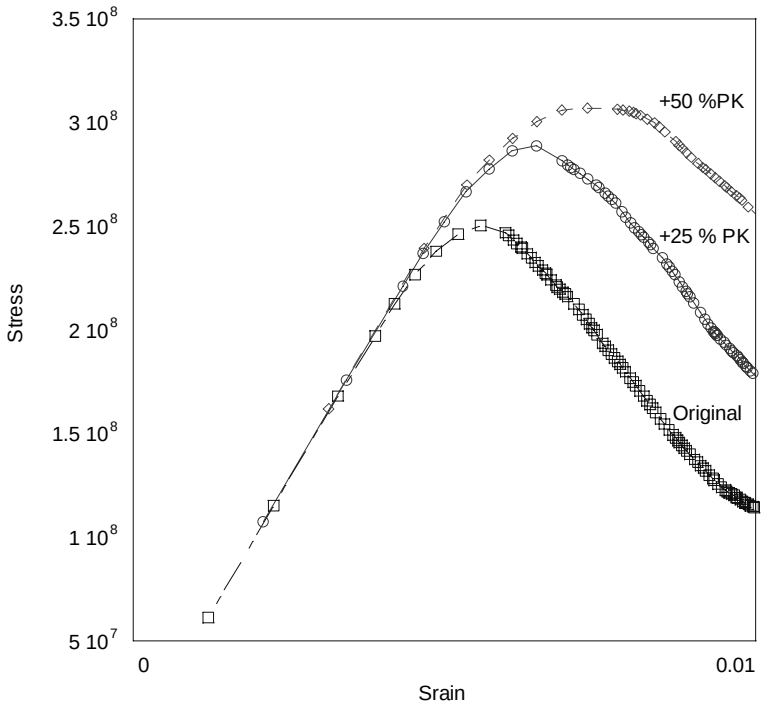

Figure 4.16 Stress-strain results for the cross-grid configuration.

The results presented here were obtained by adding a huge increment on only one of the factors controlling the dislocation reactions, with +/- 50 % of the Peach-Koehler term. Nevertheless, if a more careful treatment is followed on all the different mechanisms that account for the overall mechanical behavior such as mobility, Peierls stress and other factors with individual increases kept on the order of + 5 % as predicted by Steinberg, Moriarty and others. It is our hypothesis that all of them combined will add up and lead to similar results as the ones presented in this thesis.

Chapter 5
Molybdenum results

In this chapter are presented experimental results of oriented Mo single crystals deformed using the trianvil apparatus. These tests were done in order to isolate the behavior of specific slip systems.

5.1 Single crystal preparation

Mo single crystals were grown using the flat-zone method by Accumet Inc. Because of the nature of this kind of experiments. A high purity with respect to interstitials such as O, C, N, H and He is required. Purification was performed at the LLNL facility using the standard procedure to obtain crystals that are virtually free from contamination (decarburization followed by UHV anneal resulting in material with less than 60 at. ppm interstitial impurity content). By purifying the crystals intrinsic dislocation behaviors can be observed, in addition adverse effects caused by dislocation interactions with interstitials should be eliminated.

The specimens analyzed in this investigation consisted of oriented single crystals of Mo. The specimens were thinned to approximately 100 microns in height and were on the order of 2-3 mm in width and length.

In general, as stated in Chapter 1 the CRSS in a BCC metal is expected to have a strong orientation dependence under both pure shear and non-shear conditions [13,30-34].

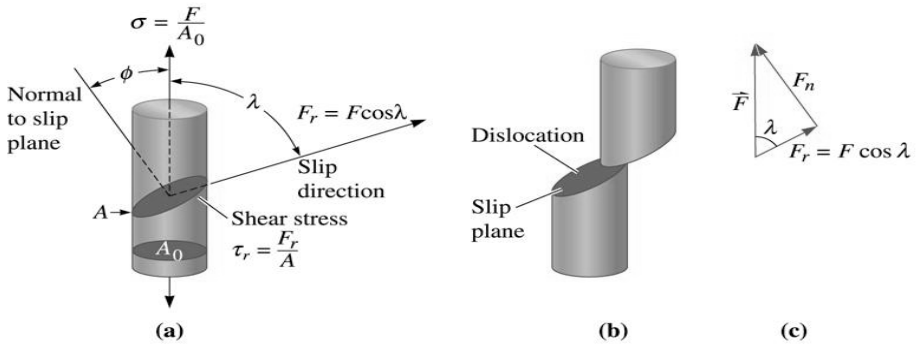

Figure 5.1 Schematic exemplifying the CRSS for the Schmid law.[web]

Because of this dependence the analysis was done so that these single crystal slivers were oriented such that the {110} and {121} slip planes were aligned in the plane of compression. They were oriented such that simple shear deformation was achieved by single slip on these slip planes along the <111> direction with no additional slip activity.

The specimens were obtained from a rod of single crystal Mo. To determine the orientation of the crystallite a small piece was cut out of this rod and EBSD was performed to measure the orientation. The red face was oriented in the SEM as shown in the coordinate system in Figure 5.2.

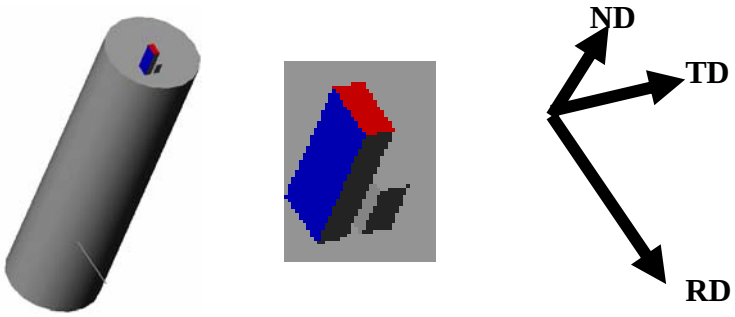

Figure 5.2 Schematic of the single crystal piece gotten to perform the study.

The results for the pole figures and orientation image are shown in Figure 5.3:

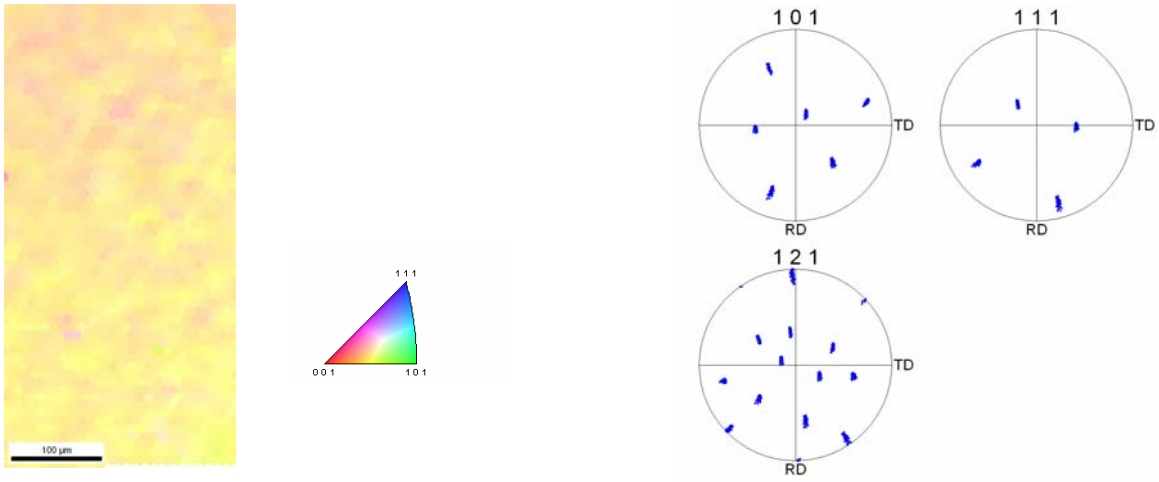

Figure 5.3 OIM results used to give the orientation to the specimen being tested..

Using the pole figure allows a better interpretation; of special interest were the 101, 111 and 121 poles.

The interpretation of the pole figure is at follows:

- The 101 pole, it can be extracted that the 101 pole is found at approximately 135º between the normal and the transverse direction.
- The 111 pole is found at ~ 45º between ND and the TD.
- The 112 coincides approximately with the RD chosen.

With this analysis a relation between the rod and the crystal reference frame was assigned. Due to that the thickness of the specimens were needed in the range of 100 microns, the final thickness was given to the material by a technique of wire electric discharge machining (EDM).

The specimens cut were analyzed again by the OIM technique in order to verify the orientation.

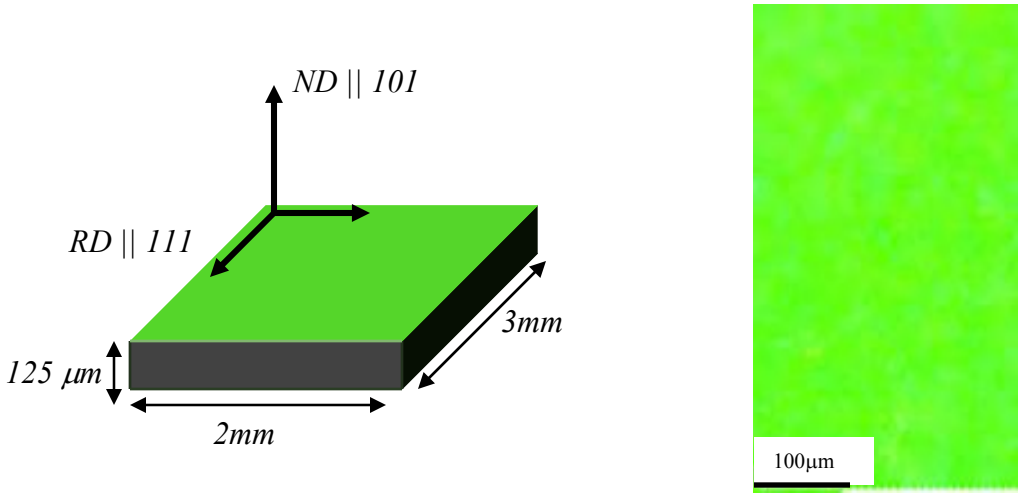

Figure 5.4a Inverse pole figure of the single crystal with the desired geometry for the 110 specimens.

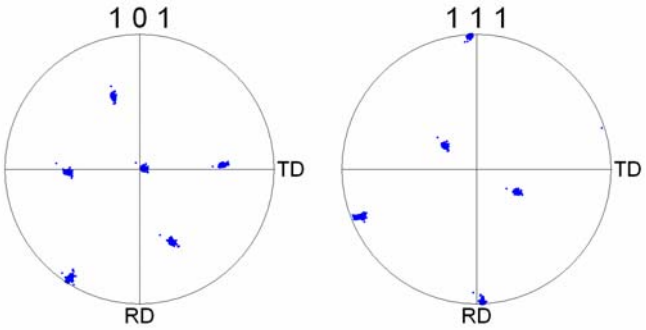

Figure 5.4b Pole figure of the single crystal showing the desired geometry for the 110 specimens.

The PF shows that the specimen is oriented so that (101) face is parallel to direction of applied load and the shear direction is aligned with the [111] crystal orientation, as it was required for this kind of experiments. Similar procedure was followed to obtain the 121 single crystal specimens.

5.2 Yield strength results

After assuring that the specimen was under hydrostatic pressure, tests for different thickness, strain rates and orientation were performed according to the procedure explained in Chapter 3. The typical shear stress – shear strain curve is shown in Figure 5.5, this is for the 100 μm specimen. The first analysis of the stress-strain curve was to estimate the yield stress from these plots. As depicted in Figure 5.5 the yield stress was obtained by taking the value of the stress when the stress- strain curve ceased to be linear, it was accomplished by overlapping a line on the plot and using the 0.2 % yield criterion.

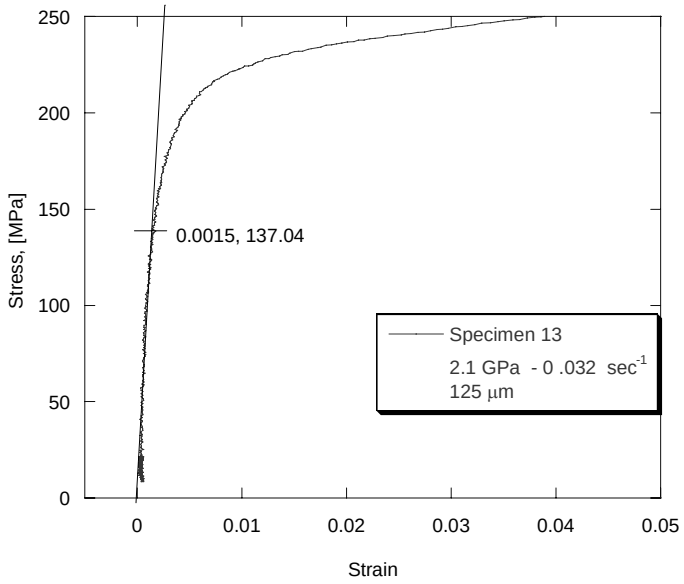

Figure 5.5 Typical plot of Stress-strain obtained in this experiment showing the value obtained for the Y_s, close to a strain of 0.2%.

The yield stress was measured and averaged for all the available data on a specific imposed condition. The results are plotted in Figure 5.6.

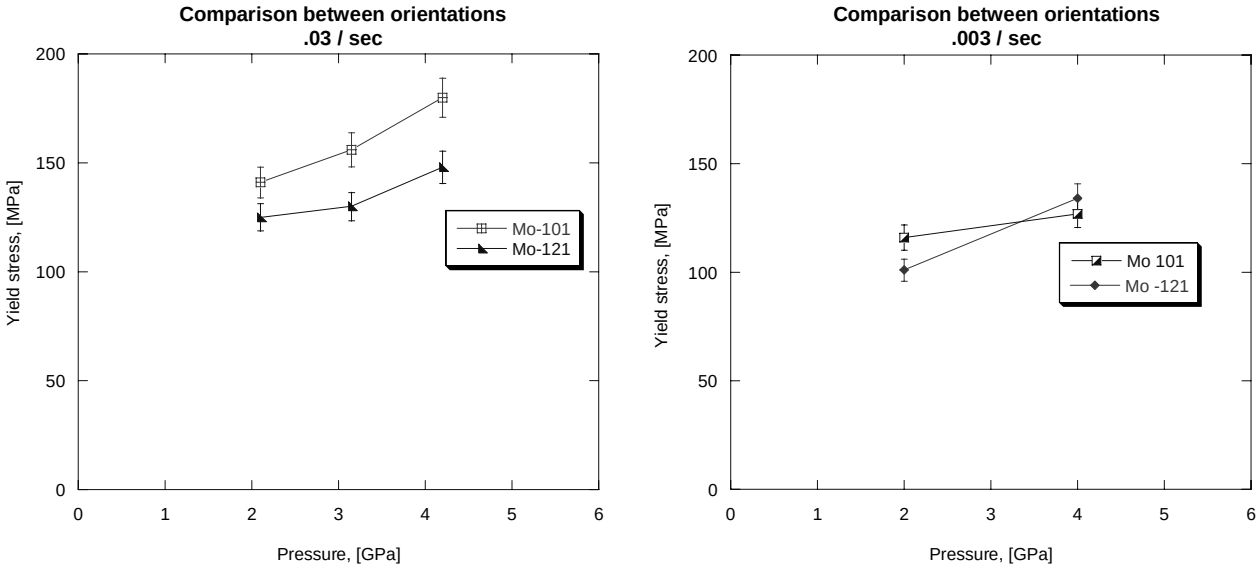

Figure 5.6 Results of the change in Ys for the {110} and {121} systems for different strain rates.

It can be appreciated in Figure 5.6 that the yield strength is changing to a lesser degree than that observed in the polycrystalline tantalum where increments close to 200% are present.

This could be due to several factors, one of them is the lack of trapping dislocations within the grain boundaries, in the case of deformation of the single crystals there is an absence of this effect. It is important to note that the yield stress of the {121} system is lower than the {110} at most cases with these imposed pressures and strain rates, the only difference comes at a strain of 0.003 where the {121} systems shows a slightly higher strength than the correspondent {101}.

5.3 Dislocation mobility

The second analysis was to calculate the stress necessary to attain a certain velocity. This velocity is a function of the geometry of the specimen, the strain rate and most importantly the strain. From the shear stress-shear strain data the values of stresses at strain close to 1% were taken from the plotted data available at all conditions as it is depicted in Figure 5.7.

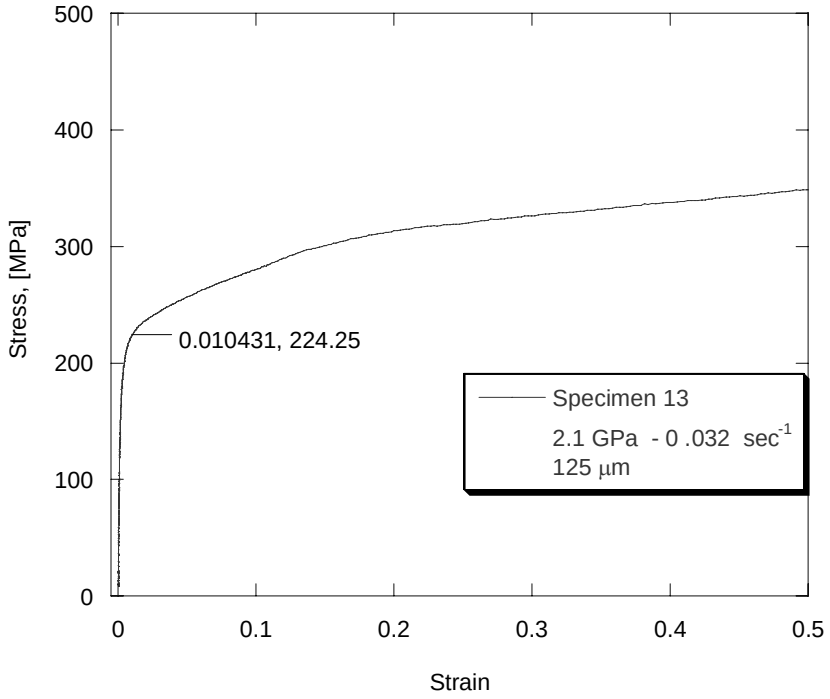

Figure 5.7 The stress was obtained to give the material a given strain and therefore a given velocity to the mobile dislocation. .

The results for the average values for stress are shown in Table 5.1, these stresses were obtained for tests with two different strain rates.

Table 5.1 Stresses at 1%deformation, [MPa]			
System	Pressure	Velocity, [cm / sec]	
		1.23	12.3
101	2.1 GPa	172	226.55
	4.2 GPa	171	247.5
121	2.1 GPa	170.5	198.66
	4.2 GPa	172	208.5
Mo	Conrad	60.23	86.41

With these stresses at the given strain the mobility was calculated under some assumptions as it is indicated in the following section.

5.3.1 Dislocation mobility calculation

From the two experimentally established dislocation velocity – applied shear stress relations shown in the background section, several predictions for the stress-strain behavior curves at one atmosphere are available.

The model that will be used to correlate the stress-strain behavior with the dislocation properties is based on the first model using the Equation 5.1 [37]

A basic equation immediately obtained is

$$\dot{\varepsilon} = b\rho v \tag{5.1}$$

where $\dot{\varepsilon}$ is the macroscopic strain rate, b is the burgers vector of the dislocation, ρ is the number of mobile dislocations and v is the velocity of a particular dislocation.

If the assumption that only pure edge and pure screw dislocations are present in the material and both of them contribute in the same amount to the strain, therefore the strain can be expressed as

$$\dot{\varepsilon} = b(\rho_e v_e + \rho_s v_s) \tag{5.2}$$

It has been found experimentally that the edge dislocations move 50 times faster than screw dislocations, then the relative dislocation densities would be:

$$\rho_s / \rho_e = v_e / v_s = 50 \tag{5.3}$$

And the total number of dislocation is

$$\rho = (\rho_e + \rho_s) = \frac{\rho_s}{50} + \rho_s \approx \rho_s \tag{5.4}$$

So Equation 5.1 transforms approximately to [35]

$$\dot{\varepsilon} = 2b\rho v_s \tag{5.5}$$

Another simplification is to relate the number of dislocations to the total strain in the form $\rho = \alpha\varepsilon$ [35,37,116], where α is to be determined by the geometry of the specimen.

To calculate the factor α, we used the simplified idea that one dislocation moves a distance *b* on one plane of the specimen, and always in the sense of shear. As shown in Figure 5.8.

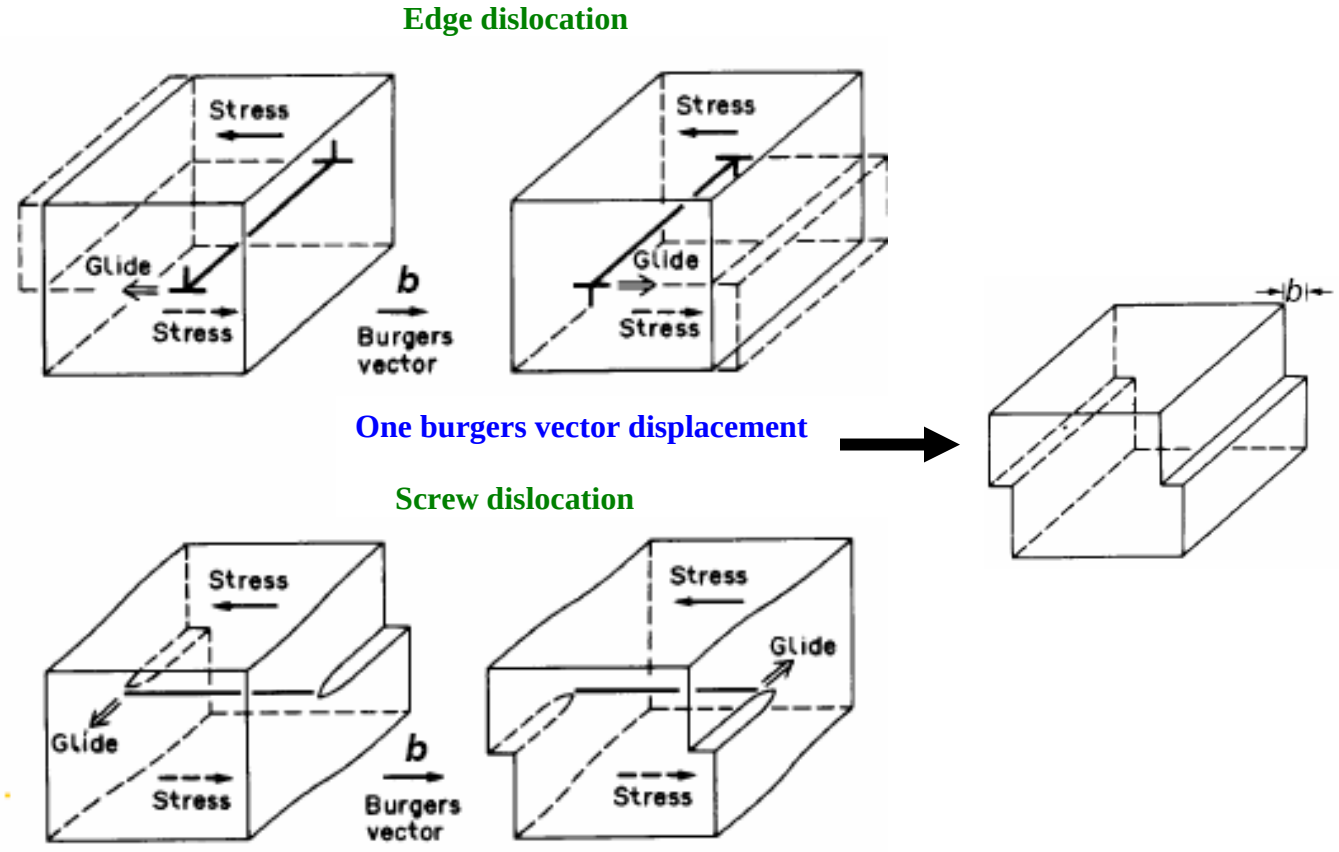

Figure 5.8 Assumption that the specimen is strained by one burgers vector for each dislocation activated and moved out of the specimen. [web]

From the geometry of the specimen being deformed, an idealization can be made for deformation of the specimen edges (see Figure 5.9).

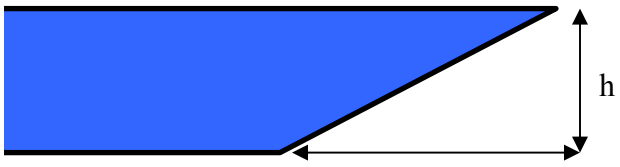

e

Figure 5.9 Schematic showing the end of the specimen.

Therefore the total number of dislocations can be calculated in the following form

$$n = \sum_{0}^{h/d_{110}} \frac{\varepsilon_{eh}}{b} \tag{5.6}$$

or by using only parameters in our geometry we can relate the total dislocation length that we need to cause the plastic deformation simply by:

$$l_{\perp} = bn = \sum_{0}^{h/d_{110}} \varepsilon_{e(h)} \tag{5.7}$$

This length is calculated as taking half of the total length of lines filling a rectangle as shown schematically in Figure 5.10

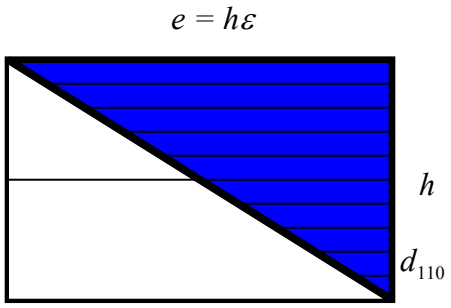

Figure 5.10 Schematic used to calculate the total dislocation length.

Each line has a length of $h\varepsilon$ and is equally separated by an inter-planar distance $d_{110} = a_0/\sqrt{2}$ for the 110 plane as is indicated in Figure 5.7. From here it is easy to calculate the dislocation length as follows:

$$l_{\perp} = \frac{e^{*}h/d_{110}}{2} = \frac{h^2}{2d_{110}}\varepsilon \tag{5.8}$$

To estimate the density we used the volume of the material V = 2 mm x 3 mm x 125 μm = 7.5 * 10^{-10} m^3. Introducing the values for the specimen:

height h = 125 μm and interplanar spacing $d_0 = a_0/\sqrt{2}$ = 0.223 nm

Finally the density can be expressed as:

$$\rho_{\perp} = \frac{l_{\perp}}{V} = \frac{h^2}{2a_0 v}\varepsilon = 4.68 * 10^6 \varepsilon \tag{5.9}$$

so in our case $\alpha = 4.68*10^6$ cm^{-2} for the 110 specimens, and in the case of 121 $\alpha = 8.1*10^6$ cm^{-2}. In the literature, values found experimentally are close to 10^8-10^9 for specimens on the order of at least 10^2 larger than those used in the present study [35,116]. From these values we can say that we are in good approximation by making this assumption. To calculate the dislocation mobility we used the following equation

$$v_g = Mb(\tau - \tau_f) \tag{5.10}$$

where the glide velocity v_g is predicted to behave in this form for a dislocation gliding on the Peierls stress barrier [15,116], and Mb is the slope resulting from the plot of v_g vs. τ .

5.3.2 Dislocation mobility results

Plotting the values from Table 4.1, and substituting the values for the parameters of our specimens the mobility was calculated graphically as shown in Figures 5.11 and 5.12. The results are summarized in Table 5.2.

Table 5.2
Mobility

System	Pressure	Mobility, Pa^{-1} s^{-1}
101	2.1 GPa	7.6
	4.2 GPa	5.5
121	2.1 GPa	14.5
	4.2 GPa	11.2
Mo	Conrad	15.9

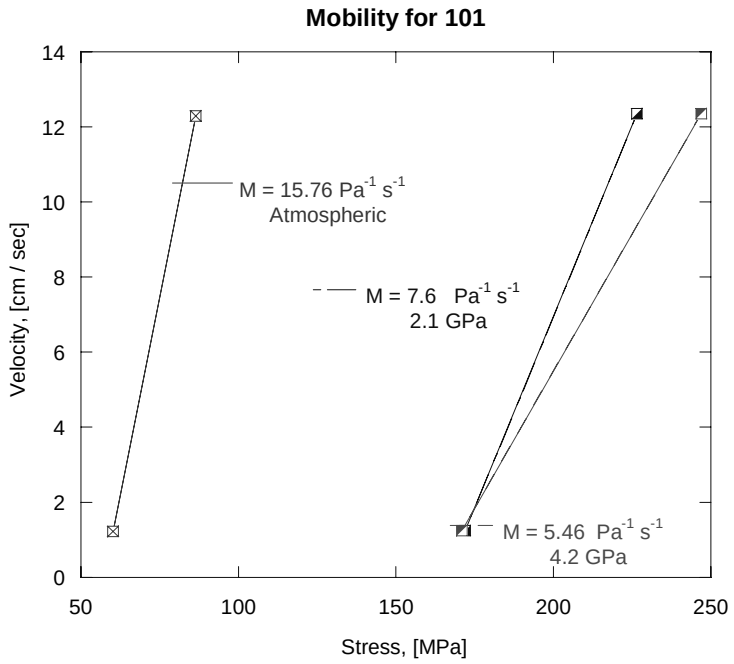

Figure 5.11 Plot of v vs. τ for the 101 orientation.

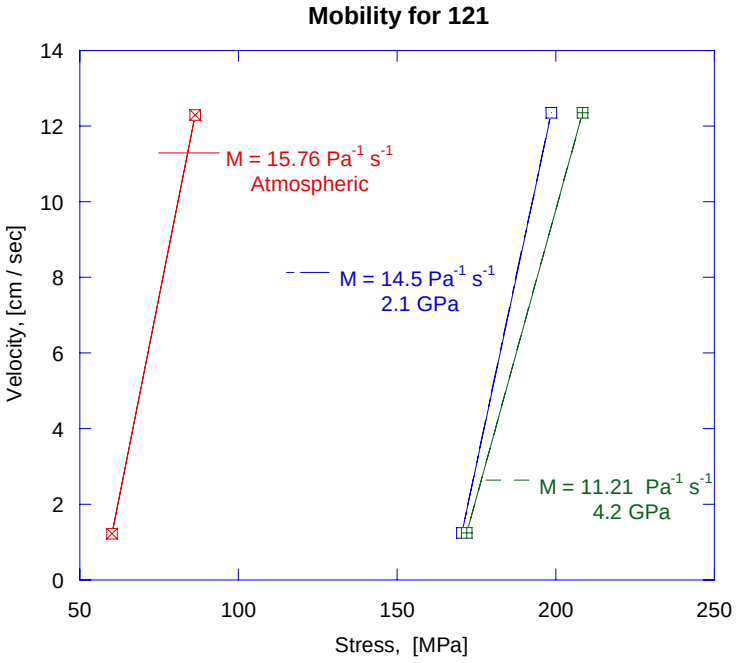

Figure 5.12 Plot of v vs. τ for the 121 orientation.

These results for the values of the dislocation mobility lie within the range of the assumed values of the mobility used by Rhee, et al [92] (= 1 $Pa^{-1}s^{-1}$) for screw dislocations in Mo for a dislocation discrete dynamics (DD) simulation at one atmosphere.

More important from these results is to note the higher mobilities of the 121 type of dislocations with respect to the 110 system at room temperature. These results are in agreement with the results at atmospheric pressure from a work by Conrad et al [39-40]. Their results are given in the graphs as comparison with the present results. During their work, it was observed, surprisingly, that the dislocations tended to move primarily on the {121} planes in spite of the higher resolved shear stress for the {110} systems. It was a constant under the range of stresses at which the experiment was carried out. From their results it is expected that a higher mobility of the {121} type of dislocation, this was corroborated here for specimens under high pressure.

Chapter 6
Contributions of This Work

Over the course of this dissertation several theories of strength were introduced and analyzed such as Tresca's, von Mises', Steinberg-Guinan's. In order to validate/contradict the concepts laid out by these theories it is necessary to conduct experiments. In the particular case of high pressure experiments, the earliest test is attributed to August Foppl [118] in the beginning of last century, he was interested in the various other strength theories, and to clarify the question of which should be used, he implement some interesting experiments. By using a thick-walled cylinder of high-grade steel, he succeeded in making compressive tests of various materials under great hydrostatic pressures.

Ever since the field of high pressure experimentation has advanced. In Chapter 1, the effects of hydrostatic pressure on mechanical behavior and deformation of materials was summarized, where some of them show a dependency of the flow stress with the imposed pressure. One of the most representative works (besides Bridgman) is the work by Spitzig and Richmond [100-101]. In their study, they established that the necessary increase in applied stress should be directly related to the increase in strain energy. They used this phenomenon trying to explain their experimental results on aluminum and iron based materials, shown in Figure 6.1 (Aluminum)

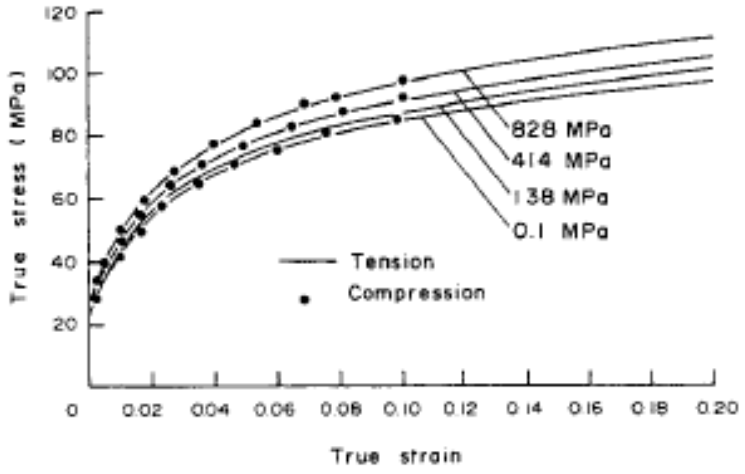

Figure 6.1 Effect of the pressure on flow stress of aluminum

They reached a relation that shows the flow stress depends linearly upon hydrostatic pressure, $\boldsymbol{p}$, in the form

$$\sigma = \sigma_0(1 + 3\alpha \boldsymbol{P}) \tag{6.1}$$

Where σ_0 is the value of σ at $\boldsymbol{p}$=0 (1atm) and is strain dependent, whereas α is the pressure coefficient which was found to be constant and equal to 58.7 and 16.5 TPa^{-1} for aluminum and all the iron-based materials respectively. By focusing on dislocation motions as the sole source of the pressure sensitivity of the flow stress we can reach a similar equation as Equation 6.1 and given by Equation 6.2

$$\tau = \tau_0(1 + \frac{2}{\boldsymbol{G}_0}\frac{\boldsymbol{dG}}{\boldsymbol{dP}}\boldsymbol{P}) \tag{6.2}$$

By combination of the last two equations we found: $\alpha = \frac{2}{3G_0}\frac{dG}{dP}$. If now we enter the values calculated by Steinberg for the pressure derivative of the shear modulus [references], a value of α is found to be 9.7 TPa^{-1} for Ta. The experimental calculated value of α for the mechanical response of Ta in our study was close to 600 TPa^{-1} . This

discrepancy suggests that the flow stress is not solely dependent on the pressure-dependent Peierls stress but also is affected by the dislocation interaction and jog mechanics.

Even though an increase on the flow stress is noted, there are several inconveniences with the previous and similar studies that use a liquid/gas phases to create the high pressure environments. The most important are listed below

- The pressure levels attained during the experiments. The pressure was less than 1GPa for the study just mentioned, and less than 2GPa for the majority introduced in Chapter 1. For higher pressures, the DAC is usually used, although this device allows ultrahigh pressures to be reached, it has the deficiency that the hydrostatic, frictional and deviatoric stresses increase in an uncontrolled manner making it difficult to extract reliable data on the flow stress of the material.
- Contamination is another factor that should be accounted. As mentioned in Chapter 1, in most cases the specimen that were tested under high pressure was coated or jacketed with some impermeable membrane The membrane is very thin and should not affect the actual response of the specimen, but nevertheless it imposes constraints on the specimen surface that might limit the natural plastic flow of the material.
- The type of observables measured by these tests. As it was shown in this thesis, the hydrostatic pressure produces an increase in the shearing capacity of the materials. In these type of tests the increase in shear stress

is indirectly extracted from the SD (strength differential) effect: strength difference at tension and compression. The SD effects have been observed in high strength steels, aluminum alloys, and polymers.

The major contribution of this work is development of a testing procedure that overcomes most of the problems mentioned above.

- ✓ It does not use any medium to impose the pressure, so contamination is not an issue.
- ✓ The pressure levels are above the average for the majority of the studies. To date a pressure of 6 GPa is the maximum we have reached, but it is dependent upon the specimen size and could be easily increased by reducing the specimen's diameter.
- ✓ As we have shown in Chapter 3, the deviatoric components are kept to a minimum and the pressure distribution, Bridgman's anvil cell Achilles' heel over the years, has been enhanced by the re-design of the anvil geometry. EBSD on the deformed samples showed that the regions that were load-bearing cover most of the area of the sample leading to an optimum in pressure uniformity.
- ✓ The best characteristic of this device is that it measures directly the shear stress of the material and its dependence upon high pressure. Contrary to previous studies where an increase in shear stress was inferred from SD measurements, it was shown in Chapter 3 and 4 that the stress measured is

a pure shear stress. This was supported by the texture measurements in the deformed specimens. EBSD analysis corroborated the predictions by the VPSC model that a {111} texture material will develop a {101} texture upon pure shearing.

Summing up, after all the improvements mentioned throughout this thesis, we have developed one of the most accurate experimental methodology to measure the shear strength of materials under pressure.

Another contribution of this work is the approach that should be followed when predicting the strength's pressure dependence. The main limitation with Steinberg's and similar types of models is that they predict the yield stress, and overall mechanical behavior, to be directly related to μ, the shear modulus. The conclusions are drawn directly from the effect of the pressure on μ, and as we have seen in order to have a significant effect, the pressure should be approaching ultrahigh values (on the order of Mbars), and therefore the dependency of flow stress with moderate pressures (<10 GPa) is usually neglected. Our study has shown that any change in μ should not be used directly to predict the flow stress at a given pressure but rather indirectly, it should be analyzed how any change (big or small) in μ could affect the dislocation behavior (cell formation) and eventually lead to an increase in the flow stress. This assertion was confirmed by the experimental results. They demonstrate that the samples were sheared to the same strain (confirmed by using EBSD-VPSC) but develop a totally different dislocation arrangement (measured using TEM) with the confining pressure as the only variable.

Finally, another contribution of our study is the confirmation that the BCC materials tested, polycrystalline Ta and Mo single crystal, deviate from the ideal elastic-plastic behavior. This ideal behavior is generally exhibited by most of the FCC metals, where their flow stress description at the dislocation level or the continuum level uses the J_2 plasticity theory [119,120]. There are at least two possible sources for the departure of most bcc metals from the ideal. One is the form of grain boundaries on the atomic scale. This state of disorder quite naturally implies a state of non-uniformity and heterogeneity in the strength properties of grain boundaries. The other possible source of non-ideal behavior for bcc metals is the fact that the core structure of dislocations spreads over many atomic layers of glide planes. As it is shown in Chapter 4, this fact greatly decreases the mobility of the dislocations and results in a greater sensitivity to temperature and pressure dependent behavior

The nonuniformity of strength of grain boundaries in fcc materials is of little importance because the great mobility of the dislocation structures implies that the loads on the grain boundaries are insufficient to cause any disruption of the grain boundary. However, in bcc metals the grain boundaries are much more highly stressed than in fcc metals [120]. Probably the grain boundary behavior is much more variable than that of the grain-to-grain form. Even if only shear stresses are needed for the individual crystals, both shear and normal stresses are needed for the grain boundary failure. Macroscopically this then requires both shear and normal stresses. The behavior of the polycrystalline aggregate thus depends not only on the shear stress on the slip planes in the individual grains, but also on normal stresses acting within the grains and on the grain

boundaries. Therefore to fully characterize a polycrystalline aggregate macroscopic characteristics involved are the shear stresses and the mean normal stress (hydrostatic pressure). This final assertion was corroborated by the different increases in flow stress for the Mo single crystal with respect to the polycrystalline Ta. In the first case an increase of 20 % was measured, while for the latter case increases close to 100% were estimated when doubling the pressure.

Chapter 7
Summary and Conclusions

A new procedure to study the mechanical properties of materials deformed by shearing strains while subjected to high pressure has been described in this work.

As was emphasized, one of the principal concerns when using this method was to corroborate that by applying a normal load, a pressure of hydrostatic-type was imposed on the thin-foil specimens. If this condition is reached, no deviatoric stresses are expected. Therefore the material should not be deformed before the shearing process took place, and the properties should remain unchanged before and after the removal of the normal load. A section is given in Chapter 3 on the details of the experiment and qualitatively in the changes experienced by the Ta, material used as a control for validating this assertion.

Based on the results exposed in Chapter 3, this procedure has proven to be a good method to study the shear stress – shear strain behavior under hydrostatic pressure. It was found that the microstructure and properties do not change significantly due solely to the effect of the pressure applied. This was corroborated via Vickers hardness characterization, with the hardness being almost equal to that of the un-deformed material, close to 116 GPa. In addition, validation was done through structural analysis via EBSD and TEM imaging. Neither of these techniques revealed significant deformation of the microstructure nor dislocation multiplication during the loading process.

After validation of the experiment, tests were performed on polycrystalline Ta and the oriented single crystals of Mo. The experiment allowed the validation of models for materials held under high pressure.

When using polycrystalline Ta, the outcome of the tests showed an influent role of the hydrostatic pressure on properties such as yield strength, and indirectly shear modulus, with the yield strength increasing more rapidly than that predicted by the models such as Steinberg and Guinan. The model predicts an increment in yield strength of close to 3% up to a pressure of 4.2 GPa. Experimentally, an increase close to 190% was observed for this material at the same pressure. It was observed that the higher the pressure the higher the rate of hardening of the specimens being deformed.

After failing to explain this behavior with the continuum models (von Mises, Tresca and Steinberg-Guinan), a multi-scale approach was followed. We started by obtaining information calculated from atomistic simulations that showed a pressure dependence such as the dislocation core polarization, intrinsically related with an increase in Peierls stress, unfortunately the increases on these properties is expected to be a factor only when the pressure approaches the Mbar (hundreds of GPa) range. Nevertheless, Molecular Dynamics offers twinning as an alternative to dislocation motion as the favored deformation mechanism under high pressure conditions.

This result and the measured dramatic change on texture led us to consider twinning as a possibility. Our assumption was tested by using the VPSC code and performing EBSD on a larger number of samples deformed with the improved Trianvil.

Based on the results, it was concluded that the change in texture was due to accumulation of slip. Close to a strain of 1, the texture is predicted to change from {111} + {100} to{101}+{121}+{123}, the primary and secondary slip planes in BCC. These {101}+{121}+{123} textures were present in all the samples subjected to pressures greater than the threshold pressure to have internal shearing. Based on these last results, we concluded that the increase in flow stress is solely due to an effect of the pressure on the dislocation behavior.

Next we analyzed the different factors that could contribute to the increase of the shear strength when increasing pressure. Their contribution is summarized below:

- Temperature and impurities were not considered because all the tests were performed at room temperature and all the specimens contain the same low impurity level (less than 60 ppm after the purification process).

- The effect of pressure on properties that are a function of the shear modulus were calculated, such as: Peierls stress, dislocation energy and interaction. The increments for each one of them were in the range of 5-10% as presented in the Chapter 4.

- One factor that was ruled out in explaining the observed results was the jog behavior at elevated pressures. The movement of a jog is a diffusion-based process and generally requires thermal activation.

- One of the less obvious but important factors was the dislocation interaction term. The energy of interaction depends on G, *b* and ν. As was shown, based on the contribution to the interaction energy we should expect the flow stress to increase between 5-10% when we double the pressure from 2 to 4GPa. Nevertheless studies show that this term may have a greater effect on how the dislocation arrange themselves when subjected to pressure, this arrangement can contribute indirectly to increases in flow stress.

To experimentally investigate this phenomenon, microstructures at the dislocation level were analyzed using Transmission Electron Microscopy. This effort was complemented by performing DD simulations with a pressure dependent shear modulus incorporated in the algorithm.

The experimental (TEM) evidence shows different microstructures with the pressure being the only variable. At low pressures (2 GPa), an expected microstructure containing only dislocations was found to be responsible for the plastic deformation. At higher pressures (4 GPa) the dislocations appear to arrange themselves into elongated cell walls, with widths of 50-100 nm and lengths close to a micron. Similar results were obtained by Tokii and co-workers when subjecting Ti-Nb samples to pressure close to 1GPa. They concluded that the pressure generated an increase in the dislocation interactions. With the interactions being stronger, the dislocations were more easily attracted causing an enhanced coalescence/annihilation depending on the burgers vector of the dislocations. This enhanced interaction causes the material to develop a microstructure formed of dislocation cells with almost no dislocation debris in the interior

of the cells. Dislocation dynamics were run with the typical dislocation arrangement of long screw segments as the initial configurations. The parameter that was changed was the magnitude of the interactions. A more complicated and careful implementation should be performed but the results obtained indicate that DD code predicts a slightly different dislocation configuration when changing the magnitude of the interactions, although we are aware that the interaction is rather large (25-50%).

After performing the tests on the polycrystalline Ta, we performed a small number of experiments on single crystal specimens. Changes in yield stress are noticed immediately. The increments are not as dramatic as in the case of polycrystalline Tantalum. For both orientations the increment in yield stress was on the order of 25% for pressures up to 4.2 GPa.

The mobility was calculated by making some simplifications of the deformation process, and assuming the materials were behaving according to the constitutive equations presented in Chapter 5. The values obtained for the mobility lie in the range used in discrete dislocation dynamics simulations for this kind of material. A value of 1 $Pa^{-1}s^{-1}$ is often arbitrarily assigned to the screw dislocation at ambient pressure. The values obtained experimentally were on the same order of magnitude: 5 and 14 for the {101}<111> and {121}<111> systems respectively.

Worthy of mention are the differences between the specimens prepared for this study. The {121}-type specimens showed a higher mobility and lower yield stress in most cases at room temperature over the pressures studied than the {110} specimens.

This was not expected. Values of the critical resolved shear stress are normally assumed to be somewhat higher in the {101} planes than on the {112} planes. The results presented here apparently in contradiction with the expected behavior, are indeed corroborating studies on Molybdenum by Conrad and Prekel in the late sixties where it was observed that dislocations were more mobile on {121} planes than on {101} planes.

.

Chapter 8
Suggestions for Future Work

Here are presented suggestions by which this work can be extended or complemented.

8.1 Suggestions for the experimental efforts that should be pursued:

- Deformation to higher pressures than the 4.5 GPa attained in this thesis. As it stated in the thesis, the anvils were made out of WC material. Even using this material the anvils were cracked under a load close to 30 kips, translated to a pressure of 6 GPa. The recommendation here is to achieve higher pressures by changing the specimen dimensions instead of increasing the load.

- The BCC materials are known for having a strong dependence on temperature. By making modifications to the actual apparatus, deformation at high temperatures could serve to study the effect of temperature. If this modification is made the Steinberg-Guinan model, that predicts dependence on both pressure and temperature, could be fully tested.

- Only two materials slip systems were studied here Ta and Mo. This work could be extended to other materials well studied in the literature as iron (or any steel) and Tungsten to mention some with the same BCC structure but different atomic properties. Additionally this study could be extended beyond the BCC lattice and compared with other structures such as FCC (Aluminum,

Copper) or HCP (Titanium) to investigate the effect of pressure in a more diverse set of materials.

8.2 Suggestions for the Modeling efforts: *Mohr Coulomb –type of response*

As we have shown, the pressure induced enhancement of dislocation interactions is causing the specimen to change from a coarse grained microstructure (average size of 20 microns) to a finer dislocation-based microstructure (cells with thickness of 50-100 nm). This phenomenon of grain size refinement could bring other types of deformation. Several investigations, both via computer modeling and experiments [121,122], suggest that Grain boundary (GB) sliding or other types of grain boundary accommodation mechanisms become dominant when the grain size is in the nanoscale regime (Figure 8.1).

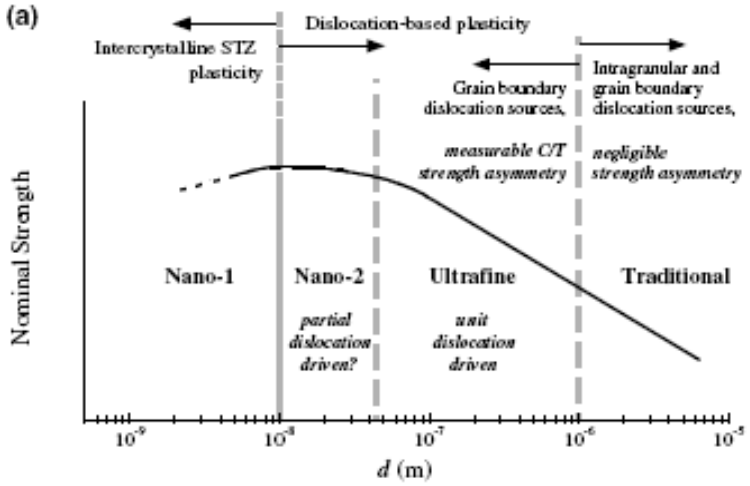

Figure 8.1 A mechanism map for deformation behavior is presented in (a), showing the nominal changes in the underlying mechanisms of plasticity at different grain sizes [122].

A MD study by Bringa showed that the relation between the stresses needed to deform plastically a nano-phase sample and hydrostatic pressure is remarkably linear, like in a simple friction mechanisms, and can therefore be captured with a Mohr-Coulomb law developed for granular materials.

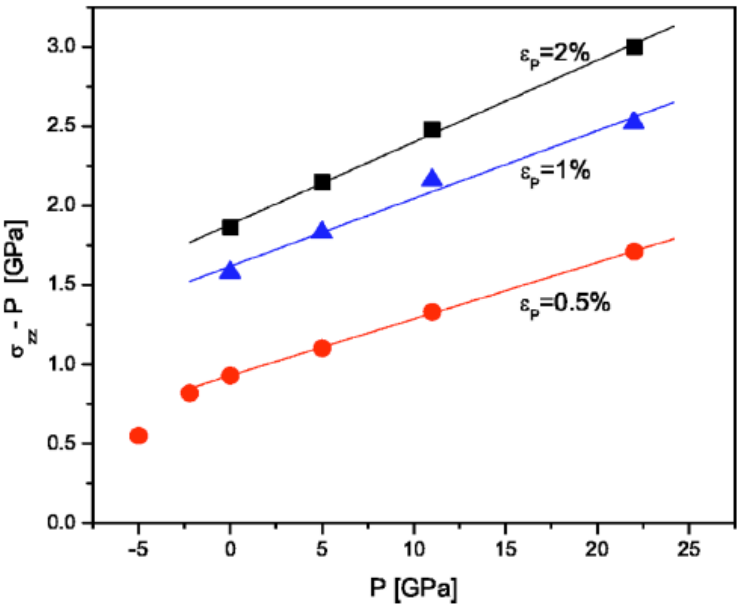

Figure 8.2 Stress necessary to produce a given amount of plastic deformation vs hydrostatic pressure[121]

There is a marked similarity of the results from this study with the ones presented in this thesis, therefore the material following a Mohr-Coulomb type of deformation, once it has developed the fine microstructure shown in Chapter 4 , could be accounted as a possibility that might be explored.

Dislocation response to High pressure

One of the issues that has not been totally described nor extensively investigated is how the material develops a hydrostatic state of stress from an applied uni-axial stress. We (I) have the idea that the dislocations are self-organizing in a reversible manner in

order to support the local stresses, a type of a Newton's third law of action and reaction. A study by Shehadeh and Bringa [123] on the shock loading of aluminum show a relaxation from a uniaxial to a relaxed hydrostatic stress (Figure 8.3).

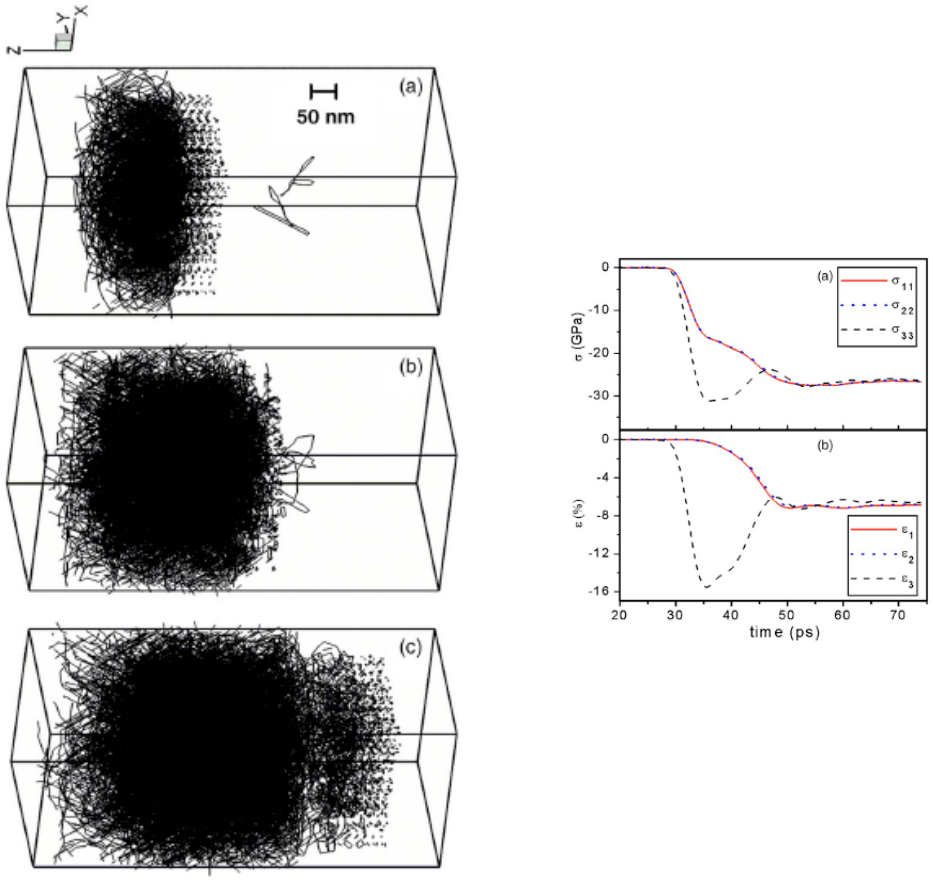

Figure 8.2 MDDP simulation of a 35 GPa, 50 ps rise time shock wave showing plastic relaxation [123].

Figure 8.3 (a) depicts a shock front moving from left to right. Loops are homogeneously nucleated as the wave travels through the material, while those previously nucleated grow as the crystal relaxes. Dislocation-dislocation interactions become dominant at high density, leading to the development of a three-dimensional pattern of intersecting loops in all available {111} slip planes, with large numbers of jogs and junctions. Shown in Figure 8.3 (b) is the stress history in a slice where the dislocation

is first nucleated showing a fluid-like behavior $\sigma_{33} \approx \sigma_{22} \approx \sigma_{11}$ such that shear stress tends to zero after some time. The strain history showing the transition from 1D to 3D ($\varepsilon_3 \approx \varepsilon_2 \approx \varepsilon_1$) is also shown

It is possible that the dislocation configuration is different at 2 and 4 GPa, with the higher the hydrostatic stress the higher the dislocation density and therefore higher tendency to develop a cell structure upon shearing.

References

[1]. McMillan Paul F *Chemistry of materials under extreme high pressure - high - temperature conditions*. Chemical communications (Cambridge, England) (2003), (8), 919-23

[2]. Aladag, Erdem; Pugh, H. Ll. D.; Radcliffe, S. V. *"Mechanical behavior of beryllium at high pressure"*. Acta Metallurgica, 17(1 (12), 1467-81 (1969)

[3]. Li, H.; Pugh, D.; Chandler, E. *"The deformation and fracture under pressure of a number of metals used in high pressure equipments"*. High Pressure Eng. , 2nd 53-61 (1977)

[4]. H Li. Pugh, *"Irreversible effects of high pressure and temperature on materials."* ASTM, 68, Philadelphia, (1964)

[5]. Das, *"Substructure and mechanical behavior of tungsten as function of pressure"*, Case institute, (1970).

[6]. Weir, S.R.; Akella, J.; Ruddle, C.; Goodwin, T. and L. Siung. *"Static strength of Ta and U under ultrahigh pressures"* Phys. Rev. B, 11258-11265, (1998).

[7]. Söderlind, P. and J.A. Moriarty, *"First-principles theory of Ta up to 10 Mbar pressure: Structural and mechanical properties,"* Phys. Rev. B 57, 10340-10350, (1998).

[8]. Yang, L.H.; Söderlind, P. and J.A. Moriarty, *"Atomistic simulation of pressure-dependent screw dislocations in bcc Ta,"* Mat. Sci. Eng. A309-310, 102-107, (2001).

[9]. B.J. Lee, M.I. Baskes, H. Kim, and Y.K. Cho, "Second nearest-neighbor modified embedded atom method potentials for bcc transition metals", Phys. Rev. B, 64,184102-1 – 184102-11, (2001)

[10]. Yang, L. H.; Soderlind, Per; Moriarty, John A. *"Accurate atomistic simulation of (a/2)[111] screw dislocations and other defects in bcc tantalum"*. Phil. Mag. A: Phys. of Cond. Matter: Structure, Defects and Mechanical Properties (2001), 81(5), 1355-1385

[11]. Moriarty, John A.; Belak, James F.; Rudd, Robert E.; Soderlind, Per; Streitz, Frederick H.; Yang, Lin H. *" Quantum-based atomistic simulation of materials properties in transition metals"* J. of Phys.: Condensed Matter , 14(11), 2825-2857 (2002)

[12]. Moriarty, John A.; Benedict, Lorin X.; Glosli, James N.; Hood, Randolph Q.; Orlikowski, Daniel A.; Patel, Mehul V.; Soderlind, Per; Streitz, Frederick H.; Tang, Meijie; Yang, Lin H. *"Robust quantum-based interatomic potentials for multiscale modeling in transition metals"*. J. of Mat. Res. , 21(3), (2006)

[13]. Xu, Wei; Moriarty, John A. *"Atomistic simulation of ideal shear strength, point defects, and screw dislocations in bcc. transition metals: Mo as a prototype"*. Physical Review B: Condensed Matter , 54(10), 6941-6951,(1996)

[14]. Kubin, L.P. and Canova,G, "*The modeling of dislocation patterns*", Scripta metall. Mater. 27, 957-962, (1992).

[15]. H.M. Zbib, H.M., Rhee, M. and Hirth, J.P.*, "On Plastic Deformation and the Dynamcis of 3D Dislocations"*, Int. J. Mech. Science, 40, 113-127, (1998)

[16]. T. Diaz de la Rubia, Zbib, H.M., T. Kharishi, B. Wirth, Victoria, M. and M. Caturla, *"Flow Localization in Irradiated Materials: A Multiscale Modeling Approach",* Nature, 406, 871-874, (2000).

[17]. H. Yasin, Zbib, H.M. and Khaleel, M. A., *"Size and Boundary Effects in Discrete Dislocation Dynamics: Coupling with Continuum Finite Element"*, Materials Science and Engineering A309-310, 294-299, (2001).

[18]. H.M. Zbib, T.D. de la Rubia, M. Rhee, and J.P. Hirth, *"3D dislocation dynamics: stress-strain behavior and hardening mechanisms in FCC and BCC metals,"* J. Nucl. Matls. 276, 154-165, (2000).

[19]. V. Bulatov, Tang, M. and Zbib, H.M., *"Crystal Plasticity from Dislocation Dynamics"*, Materials Research Society Bulletin, 26, 191-195, (2001).

[20]. H.M. Zbib, Diaz de la Rubia and Bulatov, V. *"A Multiscale Model of Plasticity Based on Discrete Dislocation Dynamics"*. ASME J. Eng. Mater, Tech., in press, (2001)

[21]. Bridgman, P.W., *"Effects of shearing stresses combined with high hydrostatic pressure"*, Phys. Rev. 48: 825-847 (1935)

[22]. Larsen, Esper S.; Bridgman, P. W.. *"Shearing experiments on some selected minerals and mineral combinations"* American Journal of Science , 36 81-94. (1938)

[23]. Bridgman, P. W.. **"***Shearing phenomena at high pressures, particularly in inorganic compounds".* Proceedings of the American Academy of Arts and Sciences, 71 387-460, (1937)..

[24]. Bridgman, P.W., *"Studies in large plastic flow and fracture with special emphasis on the effects of hydrostatic pressure"*, McGraw Hill, (1952).

[25]. Bridgman, P. W.. *"The technique of high pressure experimenting"* Proceedings of the American Academy of Arts and Sciences , 49 627-43, (1914).

[26]. Bridgman, P. W.. *"New high pressures reached with multiple apparatus."* Phys. Rev. , 57 , 342-3, (1940).

[27]. Bridgman, P.W., "*Effects of hydrostatic pressure on the plastic properties of the metals",* Rev. Mod. Phys 17 3-14 (1945)

[28]. Bridgman, P.W., *"Flow phenomena in heavily stressed metals"*, J. Appl. Phys. 8 328-336 (1937)

[29]. Bridgman, P. W.. *"Shearing phenomena at high pressure of possible importance for geology"* J. of Geol. , 44, 653-69, (1936).

[30]. Charbonnier, C.; Kruml, T. and Martin J. L., *"Multiscale Modelling of Materials"* (MRS Symp. Proc. Vol 653c) (2001)

[31]. M.S. Duesbery and V. Vitek, *"Plastic anisotropy in bcc transition metals"* Acta Mater. 46,1481, (1998).

[32]. Duesbery, M. S. *"Influence of core structure on dislocation mobility"* Phil. Mag. , 19(159), 501-26,(1969).

[33]. Hirth, J. P.; Lothe, J. *"Elastic and core anisotropies for the [111] screw dislocation in cubic crystals"* Phys. Stat. Solidi , 15(2), 487-94, (1966).

[34]. Rosenberg, J. M.; Piehler, H. R. *"Calculation of the Taylor factor and lattice rotations for bcc. metals deforming by pencil glide"* Met. Trans., 2(1), 257-9, (1971).

[35]. Kocks, U. F., Argon, A. S., and Ashby, M. F., . *"Thermodynamics and Kinetics of slip*" Prog. Mater. Sci., 19, 1. (1975)

[36]. Johnston, W.G.; Gilman, J.J. "*Dislocation velocities, densities and plastic flow in LiF"*, J. Appl. Phys, 30, 129 (1959)

[37]. Gilman, J. J. *"Dislocation mobility in crystals*", J. of Applied Phys., 36(10), 3195-206, (1965).

[38]. D . Hull and DJ Bacon, *"Introduction to dislocations"*, Pergamon press, (1984)

[39]. Weertman and Weertman, *"Elementary dislocation theory*", Oxford university press, (1992)

[40]. Prekel, H. L.; Conrad, Hans. *"Dislocation velocity measurements and thermally activated motion in molybdenum*". Acta Metallurgica , 15(5), 955-8, (1967).

[41]. Prekel, H. L.; Lawley, A.; Conrad, H. *"Dislocation velocity measurements in high purity molybdenum"*, Acta Metallurgica , 16(3), 337-45 (1968).

[42]. Christian, Jack W. *"The relation between dislocation velocity and effective-flow stress"* Acta Metallurgica , 15(7), 1257-8, (1967).

[43]. Dorn, J. E.; Mitchell, J.B.; Hauser, F.E. *"Dislocation dynamics"*. Proceedings of the Society for Experimental Stress Analysis , 22(2), 353-62, (1965).

[44]. Liu, D. S.; Lewandowski, J. J. *"The effects of superimposed hydrostatic pressure on deformation and fracture: Part I. Monolithic 6061 aluminum"*. Metallurgical Transactions A: Physical Metallurgy and Materials Science (1993), 24A(3), 601-8.

[45]. J.L. Lewandowski and P. Lowhaphandu, *"Effect of hydrostatic pressure mechanical behavior and deformation processing of materials on materials"*, Int. Mat. Reviews, 43(4), 145-164, (1998),

[46]. Radcliffe, *"Irreversible effects of high pressure and temperature on materials"* ASTM, 141, Philadelphia, (1964)

[47]. Margevicius, R. W.; Lewandowski, J. J.; Locci, I. E. *"Yield point behavior in nickel-aluminum (NiAl)*" Scripta Metall. et Mater., 29(10), 1309-12, (1993).

[48]. Margevicius, R. W.; Lewandowski, J. J.. *"Deformation texture of hydrostatically extruded polycrystalline nickel-aluminum (NiAl)*" Scripta Metall. et Mater., 29(12), 1651-4 (1993).

[49]. M .I. Emerets, *"High Pressure experimental methods"*, Oxford Press, (1996)

[50]. Newhall, D. H.; Abbot, L. H. "*The bulk modulus cell - new high-pressure measurement instrument"* Chemical Engineering Progress , 56(3), (1960).

[51]. Jones, G.; Dunstan, D. J. *"Diamond - anvil uniaxial stress cell*", Rev. of Sci. Inst. , 67(2), 489-93, (1996).

[52]. Lassila, D.H, "*Material Strength at Pressure",* LDRD Strategic Initiative final Report, (2004)

[53]. Tresca, Comp. Rend., 59, 754, (1864)

[54]. Coulomb, C.A. (1773), Mem. De. Math et de Phys. 1 , 343, 382 (1776)

[55]. Von Mises, Angen Math met., 8, 161, (1928)

[56]. Bullen, F. P.; Henderson, F.; Wain, H. L.; Paterson, M. S. *"The effect of hydrostatic pressure on brittleness in chromium*". Phil. Mag. , 9(101), 803-815, (1964)

[57]. Besag, F. M. C.; Bullen, Francis P. *"Effect of pressurization on yield by twinning in Armco iron.* Philosophical Magazine, 14(132), 1259-1270, (1966).

[58]. Das, G.; Radcliffe, S. V. *"Effects of hydrostatic pressure on the mechanical behavior of tungsten"* Proc. Int. Conf. Strength Metals Alloys , Meeting Date 1967, 9 334-42, (1968).

[59]. Auger, J. P.; Francois, D. "*Variation of fracture toughness of a 7075 aluminum alloy with hydrostatic pressure and relationship with tensile ductility*" Int. J. of Fract., 13(4), 431-41, (1977).

[60]. Auger, J. P.; Francois, D. "*Fracture toughness measurements on a high-strength aluminum alloy under hydrostatic pressure"*. Revue de Physique Appliquee (1974), 9(4), 637-49

[61]. DJ Steinberg, SG Cochran, MW Guinan *"Constitutive model for metals applicable at high strain rate"*, J. Appl. Phys. 51: 1498- 1505 (1980).

[62]. D. Steinberg, D Breithaupt, C Honodel *" Work-hardening and effective viscosity of solid beryllium"*, Physica 139 & 140B, 762-765 (1986).

[63]. DJ Steinberg and CM Lund , *"A constitutive model for strain rates 10^{-4} to 10^{6} s^{-1}"* , J. Appl. Phys. 65, 4 (1989).

[64]. LH Thomas, E. Fermi, Proc. Cambridge Phil. Soc,23, 542,(1927)

[65]. Kaufmann, H. J.; Luft, A.; Schulze, D. *"Deformation mechanism and dislocation structure of high-purity molybdenum single crystals at low temperatures*" Crys. Res. and Tech. , 19(3), 357-72, (1984).

[66]. Lawley, A.; Gaigher, H. L. *Deformation structures in zone-melted molybdenum*. Phil. Mag., 10(103), 15-33, (1964).

[67]. T. Imura, K. Noda, H. Matsui, H. Saka, H. Kimura, in: Dislocations in Solids, University of Tokyo Press, p. 287., (1985).

[68]. Vitek, V.. Theory *of the core structures of dislocations in body-centered-cubic metals.* Crystal Lattice Defects, 5(1), 1-34, (1974).

[69]. Vitek, V.; Perrin, R. C.; Bowen, D. K. *"Core structure of 1/2<111> screw dislocations in bcc. crystals"*. Phil. Mag., 21(173), 1049-1073, (1970).

[70]. Vitek, Vaclav. Atomic structure of stacking faults, twins, and screw dislocations in bcc. metals. Int. Conf. Strength Metals Alloys, Conf. Proc., 2nd (1970), 2 389-93.

[71]. Duesbery, M. S.. The mechanical properties of the dislocation core. Contemporary Physics (1986), 27(2), 145-68.

[72]. Duesbery, M. S.; Richardson, G. Y. The dislocation core in crystalline materials. Critical Reviews in Solid State and Materials Sciences (1991), 17(1), 1-46

[73]. Sigle, W.. High-resolution electron microscopy and molecular dynamics study of the (a/2)[111] screw dislocation in molybdenum. Philosophical Magazine A: Physics of Condensed Matter: Structure, Defects and Mechanical Properties (1999), 79(5), 1009-1020.

[74]. Hirth and Lothe, Theory of Dislocations, 2nd Ed.

[75]. Fikar, Viguier, Krumi and Dupas, "Searching for the proper law of dislocation" J. Phys. Condens. Matter 14, 12887–12895 (2002)

[76]. Xu, Dong-Sheng; Chang, Jin-Peng; Li, Ju; Yang, Rui; Li, Dong; Yip, Sidney. "*Dislocation slip or deformation twinning: confining pressure makes a difference"* Mat. Sci. & Eng. A: Structural Materials: Properties, Microstructure and Processing , A387-A389, 840-844, (2004)

[77]. Xu, D. S.; Yang, R.; Li, J.; Chang, J. P.; Wang, H.; Li, D.; Yip, S. *"Atomistic simulation of the influence of pressure on dislocation nucleation in bcc Mo"* Computational Materials Science , 36(1-2), 60-64, (2006).

[78]. Finnis, M. W.; Sinclair, J. E. *"A simple empirical N-body potential for transition metals"* Philosophical Magazine A: Physics of Condensed Matter: Structure, Defects and Mechanical Properties (1984), 50(1), 45-55.

[79]. Finnis, M. W. *" Energy and elastic constants of simple metals in terms of pairwise interactions".* Journal of Physics F: Metal Physics, 4(10), 1645-56, (1974)

[80]. Finnis, M. W.. "*Defect energies and linear screening theory in simple metals"* J. of Physics F: Metal Physics , 5(12), 2227-40., (1975).

[81]. Holland, D. Brunner and Seeger A. *"Work Hardening and flow stress of ultrapure molybdenum single crystals"*, Mater Sci Eng A, 254, 319-321, (2001).

[82]. M.F. Horstemeyer, M.I. Baskes, A. Godfrey, and D.A. Hughes, *"A large deformation atomistic study examining crystal orientation effects on the stress-strain relationship."* Int. J. Plasticity 18, 203, (2002).

[83]. Hanaffe, H.F. *"Effect of hydrostatic pressure on dislocation mobility"*, Case Institute, 90-96, (1966).

[84]. Lucke, Kurt; Lange, Hansheinz. *"Solidification curve of pure aluminum crystals and formation of deformation bands*" Zeitschrift fuer Metallkunde ,43, 55-65,(1952).

[85]. M.S. Duesbery, in: F.R.N. Nabarro (Ed.), Dislocations in Solids Elsevier, Amsterdam, 67, (1989)

[86]. Seeger, A.; Wuethrich, C. *"Dislocation relaxation processes in body-centered cubic metals"* Nuovo Cimento della Societa Italiana di Fisica, B: General Physics, Relativity, Astronomy, and Plasmas , 33B(1), 38-75, (1976).

[87]. Ito, K.; Vitek, V. *"Atomistic study of non-Schmid effects in the plastic yielding of bcc metals*" Phil.Mag. A: Physics of Condensed Matter: Structure, Defects and Mechanical Properties, 81(5), 1387-1407, (2001).

[88]. Keyes, RW *"Continuum Models of activated process of solid under pressure*", 710, (1963).

[89]. OIM software: Help menu

[90]. Lebensohn, R.A, Tome, C.N.; *"A self-consistent visco-plastic model:prediction of rolling textures of anisotropic polycrystals"*. Mat. Sci. Eng. A 175(2) 71-82 (1994).

[91]. Lebensohn, R.A, Tome, C.N. *"A self-consistent visco-plastic approach for the simulation of plastic simulation and texture development of polycrystals: Application to zirconium alloys"*. Acta Metall. Mater. 41, 2611–2624 (1993)

[92]. Tomé C, Lebensohn RA *"VPSC instruction manual"*, LANL, May 2007

[93]. Rhee, M., Lassila, D. H., Bulatov, V. V., Hsiung, L. and de la Rubia, T. *"Dislocation multiplication in bcc molybdenum: a dislocation dynamics simulation"*, Phil. Mag. Letters 81(9) 595 – 605 (2001)

[94]. Towle, L.; Riecker, R; *"Some consequences of the pressure gradients in Bridgman anvil devices"*, J. Geophys. Res. 71(10) 2609-2617, (1966)

[95]. Myers, M. *"Contribution to calibration of high pressure systems from studies in an opposed anvil apparatus"*, High Pressure Measurements, Butterworths, (1963).

[96]. Myers, M.B.; Dachille, F.; Rustum, R., *"Pressure multiplication effect in opposed-anvil configurations"*. Rev. Sci. Inst. 34 401-2 (1963).

[97]. Montgomery, P.W, Stromberg WH, Jura G.H., *"Calibration of Bridgman anvils, a pressure scale to 125 kb"*, High Pressure Measurements, Butterworths, (1963).

[98]. Jackson, J.W, and Waxman, M, *"An analysis of pressure and tress distribution under rigid Bridgman-type anvils"*, High Pressure Measurements, Butterworths, (1963).

[99]. Ma, Yanzhang; Selvi, Emre; Levitas, Valery I.; Hashemi, Javad. *"Effect of shear strain on the □ -□ phase transition of iron: a new approach in the rotational diamond anvil cell"*. Journal of Physics: Condensed Matter (2006), 18(25)

[100]. Levitas, Valery I.; Ma, Yanzhang; Hashemi, Javad; Holtz, Mark; Guven, Necip. *"Strain-induced disorder, phase transformations, and transformation-induced plasticity in hexagonal boron nitride under compression and shear in a rotational diamond anvil cell: In situ x-ray diffraction study and modeling"* J. of Chemical Physics , 125(4), (2006)

[101]. Spitzig, W.A., and Richmond, O., *"The effect of pressure on the flow of metals"* , Act. Metall. 32 457-463 (1984)

[102]. Brownrigg, A.; Spitzig, W. A.; Richmond, O.; Teirlinck, D.; Embury, J. D. *"The influence of hydrostatic pressure on the flow stress and ductility of a spherodized 1045 steel"*. Acta Metall. 31(8) 1141-50 (1983).

[103]. Hsiung, L. M.; Lassila, D. H.. *"Shock-induced deformation twinning and omega transformation in tantalum and tantalum-tungsten alloys".* Acta Mater., 48(20), 4851-4865 , (2000).

[104]. Hsiung, L. M.; Lassila, D. H.. *"Shock-induced omega phase in tantalum. Scripta Materialia"* , 38(9), 1371-1376, (1998).

[105]. Hsiung, L. M.; Lassila, D. H.. *"Shock-induced displacive transformations in tantalum and tantalum-tungsten alloys"* Scripta Materialia , 39(4/5), (1998).

[106]. Shoenfeld, S. *"Dynamic behavior of polycrystalline tantalum",* Int. J. Plast. 14(9) 871-890, (1998)

[107]. Lew, A.; Caspersen, K.; Carter, E. A.; Ortiz, M. *"Quantum mechanics based multiscale modeling of stress-induced phase transformations in iron"* J. of the Mech. and Phys. of Solids , 54(6), 1276-1303, (2006).

[108]. Tokii, V.V., Zaitzev VI, Filatov, B.P. *"Mechanism of the formation of ordered dislocation structures of metals deformed under high hydrostatic pressure".* Ukranskii Fizichskii Zhurnal 18(7) 1178-1181 (1973).

[109]. Tokii, V.V., Zaitzev VI, *"Hydrostatic pressure effect on dislocations".* Phys stat. sol. (a) 12 53-60 (1972).

[110]. Galkin, A. A., Tokii, V.V., Zaitzev VI, *"Influence of isotropic hydrostatic pressure in the interactions of dislocations".* Soviet Phys – Doklady 17(5) 498-500 (1972).

[111]. Aladag, Erdem; Davis, Lance A.; Gordon, Robert Boyd. *"Cross slip and the plastic deformation of sodium chloride single and polycrystals at high pressure*". Philosophical Magazine (1970), 21(171), 469-78.

[112]. Pampillo, C. A.; Davis, L. A. *"Volume change during deformation and pressure dependence of yield stress"* J. of App. Phys., 42(12), 4674-9, (1971).

[113]. Auten, T. A.; Davis, L. A.; Gordon, R. B. *"Hydrostatic pressure and the mechanical properties of sodium chloride polycrystals"* Phil. Mag. , 28(2), 335-41, (1973)..

[114]. Jung, J., *"A note on the influence of hydrostatic pressure on dislocations"* Phil. Mag. A: Physics of Condensed Matter: Structure, Defects and Mechanical Properties, 43(4), 1057-61, (1981).

[115]. Stainier, L., Cuitiño, A.M.; Ortiz M., *"A micromechanical model of hardening, rate sensitivity and thermalsoftening in bcc single crystals",* J. of Mech. and Phys. of sol. 50, 1511-1545, (2002)

[116]. Meyers, MA, BensonsDJ, Voringer, Kad, Xuw, Fu "*Consitutive description of dynamic deformation: physically based mechanisms"* Mat. Sci. and Eng. A322 194-216, (2002)

[117]. Devincre, B.; Kubin, L.; Hoc, T. *"Physical analyses of crystal plasticity by DD simulations"* Scripta Materialia, 54(5), 741-746, (2006).

[118]. Timoshenko S.P., *History of Strength of Materials*, McGraw-Hill, New York, (1953).

[119]. Christensen, Richard M.. *"Yield functions/failure criteria for isotropic materials*" Proceedings of the Royal Society of London, Series A: Mathematical, Physical and Engineering Sciences (1997), 453(1962), 1473-1491

[120]. Christensen, Richard M. *"Yield functions/failure criteria for isotropic materials", J*. of Mech. of Mat and Struct. 1(1),(2006)

[121]. Bringa, E. M.; Caro, A.; Leveugle, E. *"Pressure effects on grain boundary plasticity in nanophase metals"*. Applied Physics Letters , 89(2), (2006)

[122]. Lund, A.C.; Shuh C.A. *"Strength asymmetry in nanocrystalline metals under muitiaxial loading",* Acta Mat., 53, 3195-3205 (2005)

[123]. Shehadeh, Mutasem A.; Bringa, E. M.; Zbib, H. M.; McNaney, J. M.; Remington, B. A. *"Simulation of shock-induced plasticity including homogeneous and heterogeneous dislocation nucleations"*. App. Phys. Letters, 89(17), (2006)

APPENDICES

Appendix A.1 Extensometer properties

The operating properties of the extensometer are in Table A.1

Table A.1 Extensometer properties	
Operating Temperature	- 450º F to 300 º F
Gage diameter	0.303 in
Bridge Resistance	350 ohms
Displacement range	± 0.015 in

Brass pins .303'' long were used in order to calibrate the extensometers. A more detailed analysis could be made on the behavior of the machine, comparing the difference between the angles read by the ram and the extensometers at different pressures (see Figure A.1).

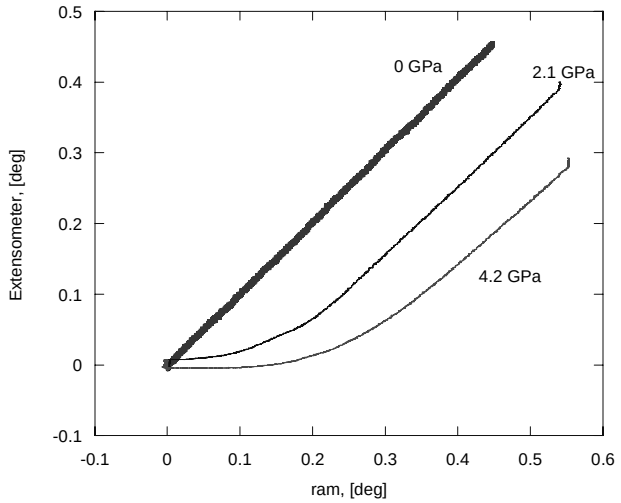

Figure A.1 Machine compliance as function of pressure.

An exact 1 to 1 relation is found between the extensometer and ram at atmospheric pressure, at high pressures is apparent that the higher the pressure, the larger he compliance of the machine.

Appendix A.2 Designs to adapt the Tri-anvil apparatus to WSU facilities

Figure A.2.1 Load Cell adapter: this part was designed to attach the upper part of the apparatus to the crosshead of the MTS machine.

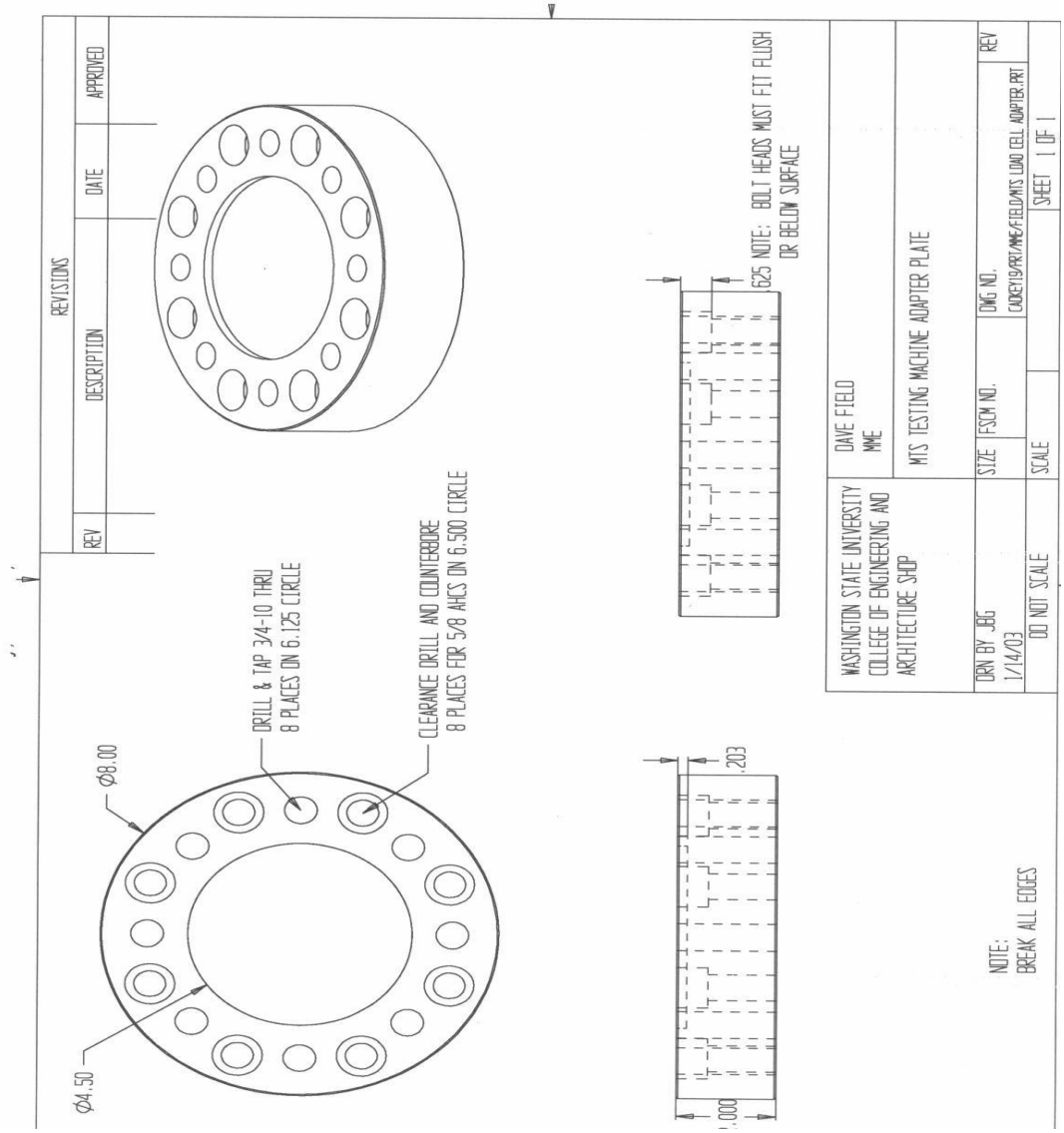

Figure A.2.2 Exchanger features: the following two features were designed in order to help in exchanging the dies used in this research and other of ongoing projects using the same MTS machine.

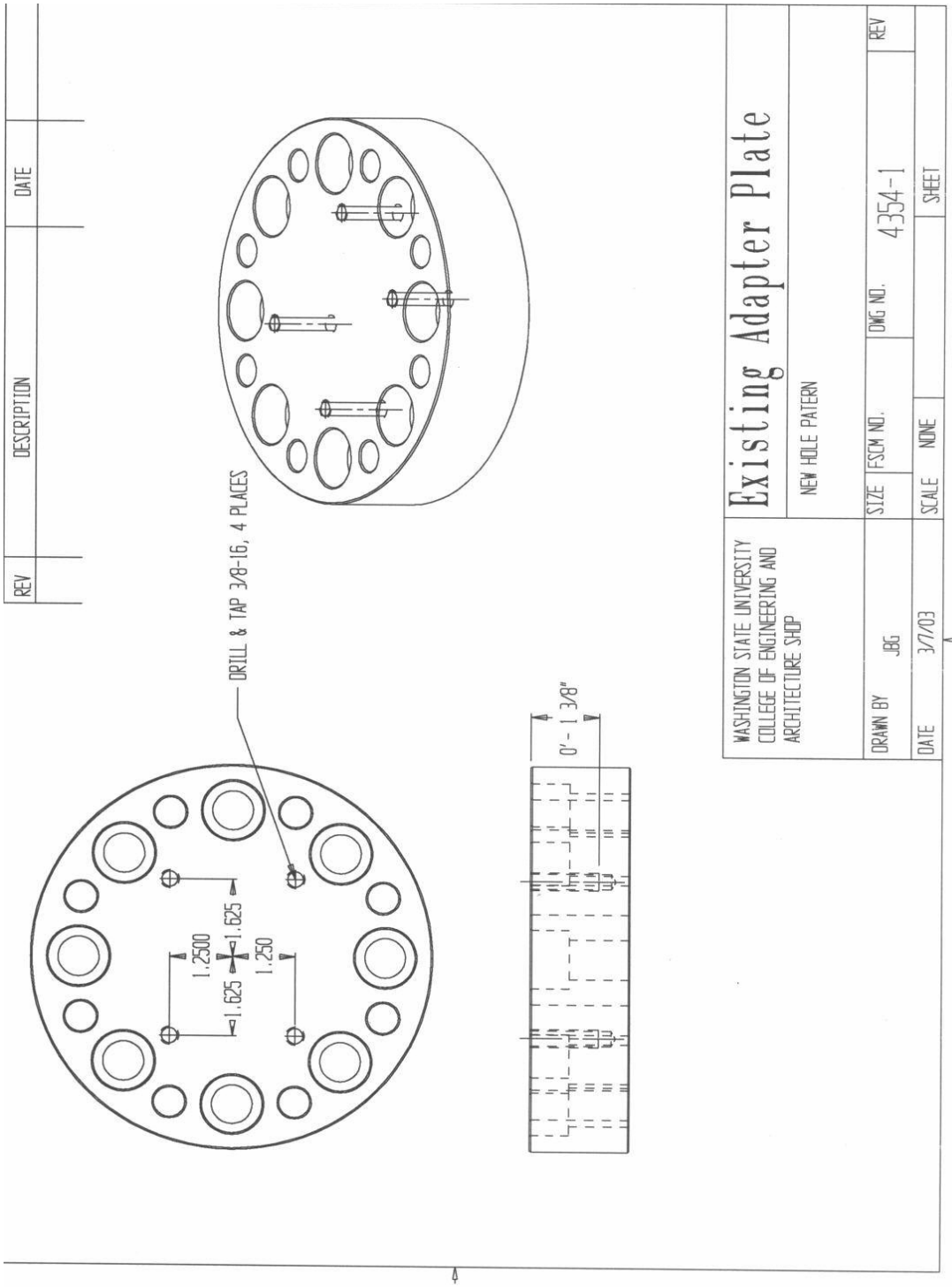

Figure A.2.3 Exchanger feature - 2

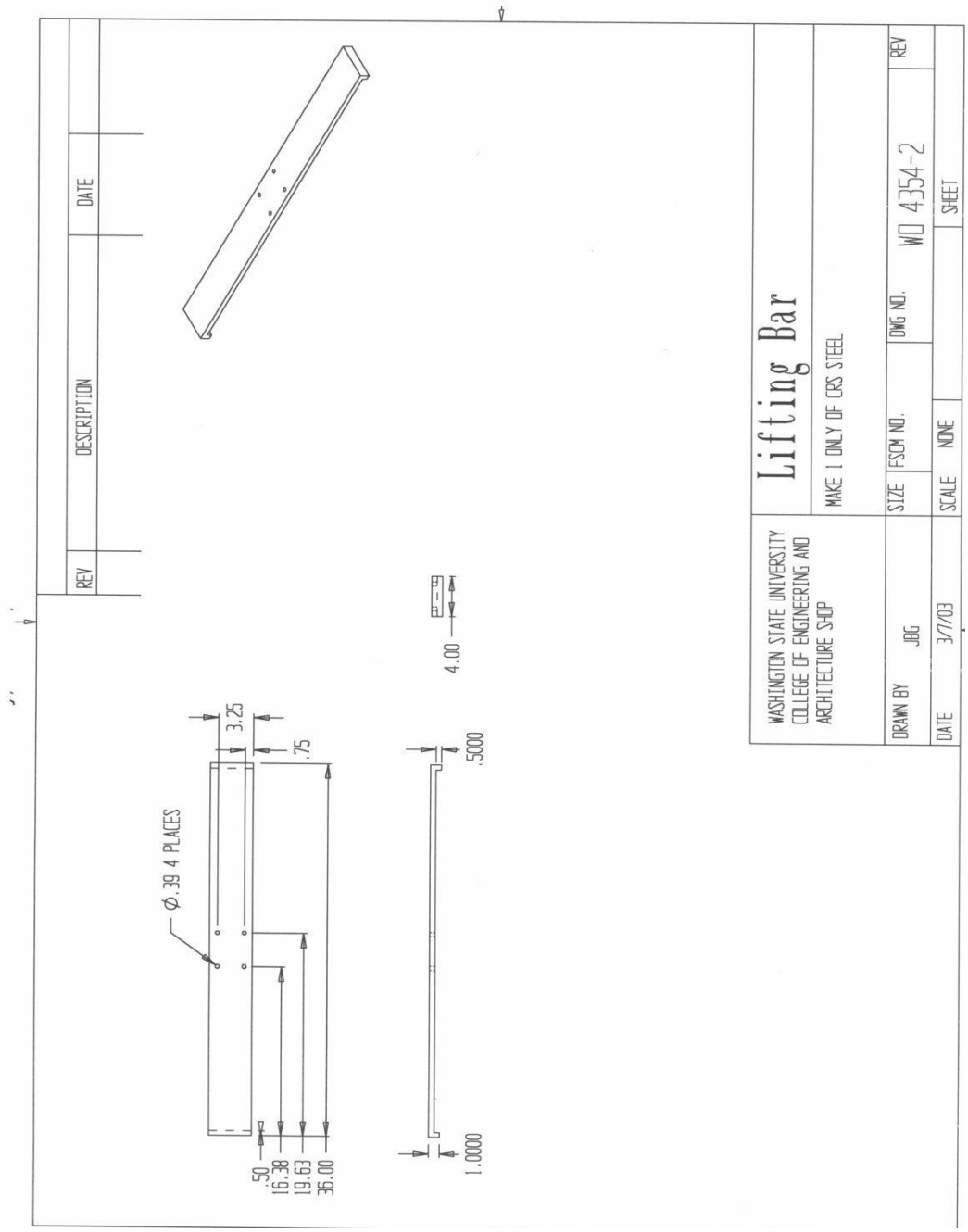

Appendix A.3 VPSC input files.

Information about the run conditions, the paths and names of the various input files that the code may require are all declared in VPSC6.IN, which may be regarded as the 'master' input file. Next is given the file that was used for running the VPSC simulations along with the description of all the components of the file.

VPSC7.IN file used in our simulations

```
1                          number of elements (nelem)
1                          number of phases (nph)
1.0  0.0                   relative vol. fract. of phases (wph(i))
*INFORMATION ABOUT PHASE #1
0                         grain shape and orient ctrl (ishape=0 to 4)
1.0  1.0  1.0             initial ellipsoid ratios (dummy if ishape=4)
0.0  0.0  0.0             init Eul ang ellips axes (dummy if ishape=3,4)
* name and path of texture file (filetext)
bcctantalum\Taexporiginal.tex
* name and path of single crystal file (filecrys)
bcctantalum\Ta.sxa
* name and path of grain shape file (dummy if ishape=0) (fileaxes)
shape1.100
*PRECISION SETTINGS FOR CONVERGENCE PROCEDURES (default values)
0.001 0.001 0.001 0.001    errs,errd,errm,errso
100 100 25     itmax:   max # of iter, external, internal and SO loops
0  2. 10. 2.   irsvar & xrsini,xrsfin,xrstep (dummy if irsvar=0)
1              ibcinv (0: don't use <Bc>**-1, 1: use <Bc>**-1 in SC eq)
*INPUT/OUTPUT SETTINGS FOR THE RUN (default is zero)
0          irecover:read grain states from POSTMORT.IN (1) or not (0)?
0          isave:   write grain states in POSTMORT.OUT at step 'isave'?
0          icubcomp:calculate fcc rolling components?
0              nwrite (frequency of texture downloads)
*MODELING CONDITIONS FOR THE RUN
0              ihardlaw (0:Voce, 1:MTS, 2:composite grain)
1              iratesens (0:rate insensitive, 1:rate sensitive)
0              interaction
(0:FC,1:affine,2:secant,3:neff=10,4:tangent,5:SO)
1  1  1        iupdate: update orient, grain shape, hardening
0              nneigh (0 for no neighbors, 1 for pairs, etc.)
0              iflu (0: don't calc, 1: calc fluctuations)
*NUMBER OF PROCESSES (COMBINATION OF UNIFORM OR VARIABLE
LOAD,PCYS,LANKFORD)
2
*IVGVAR AND PATH\NAME OF FILE OR STRESS SUBSPACE OR ANGULAR INCREMENT
0         ivgvar=0 will run a monotonic strain path
bcctantalum\shear.ta
2         ivgvar=2 will calculate PCYS at the end
1 2             -->   section of stress space
```

Description of the components:

****
File VPSC6.IN
****

Line 1: number of elements 'NELEM' (usually one)
Line 2: number of crystallographic phases in the aggregate 'NPH'
Line 3: relative volume fractions of the phases 'WPH(1:nph)' Line 4: reminder.
Line 5: index for grain shape and grain orientation control (ISHAPE=0 to 4)
ISHAPE=0 : average grain shape is assumed for each grain when calculating the Eshelby tensor.
ISHAPE=1 : same as before plus keeps track of individual grain shapes and orientations.
ISHAPE=2 : uses individual grain shapes and orientations to calculate Eshelby tensor.
ISHAPE=3 : same as before plus reads initial grain orientations from FILEAXES.
ISHAPE=4 : same as before plus reads initial grain shapes from FILEAXES.
Line 6: initial length of ellipsoid axes (length1, length2, length3) describing average grain shape (dummy if ISHAPE=4). Only the ratios matter, and not the absolute values.
Line 7: Euler angles describing the initial position of the average ellipsoid with respect to the sample axes (dummy if ISHAPE=3,4). Axis1 will be assumed to be of length1, axis2 of length2, axis3 of length3.
Line 8: reminder.
Line 9: name and path of crystallographic texture file FILETEXT.
Line 10: reminder
Line 11: name and path of single crystal properties file FILECRYS.
Line 12: reminder
Line 13: name and path of grain morphology file FILEAXES (dummy if ISHAPE=0,1,2).
Line 14: reminder.
Line 15: relative tolerances ERRS, ERRD, ERRM, ERRSO allowed in the convergence procedures inside SUBROUTINE VPSC7 (see Section 2-1). Typically 0.001..
Line 16: maximum number of iterations ITMAXEXT and ITMAXINT allowed in the convergence procedure of the loop over grain stress states, and the loop over the overall modulus. Typically ITMAXEXT=100 and ITMAXINT=25. Also number of iterations associated with the Second Order loop (typically 25)
Line 18: parameter IRECOVER.
If IRECOVER=0 uses Taylor stresses as the initial guess in the first step.
If IRECOVER=1 reads grain and polycrystal states from POSTMORT.IN.
Line 19 parameter ISAVE.
If ISAVE=0 does not write initial state of grains and polycrystal.
If ISAVE=*n* writes grain and polycrystal states into POSTMORT.OUT for deformation step *n*.
Line 20: parameter ICUBCOM.
If ICUBCOM=1 calculates the volume fraction associated with each of the typical fcc rolling components (copper, cube, Goss, S) for each deformation step. VPSC7 will look for file CUBCOMP.IN to read orientation of all crystallographically equivalent components.
If ICUBCOMP=0 skips such calculation.
Line 21: parameter NWRITE controls frequency of texture writing in file TEX_PHn.OUT.
Texture is written every NWRITE incremental steps.
If NWRITE=0 (default) texture is written only for the last step.

Line 22: reminder
Line 23: parameter IHARDLAW
If IHARDLAW=0 uses the hardening parameters associated with the Voce law. Parameters are read from file FILECRYS.
If IHARDLAW=1 uses MTS hardening parameters. This is not an option provided to the standard user.

If IHARDLAW=2 uses a 'composite grain' hardening model, specific to twinning barriers. This is not an option provided to the standard user.

Line 24: parameter IRATESENS.

If IRATESENS=1 it allows for the rate sensitivity induced by the power *n* in Eq. 5-1.

If IRATESENS=0 it scales in Eq. 5-1 to the norm of the macroscopic strain-rate, which has the effect of making the result rate-insensitive.

This option does not affect the system activity or the texture evolution; only affects the stress.

Line 25: type of inclusion-matrix INTERACTION to be used. (0:Taylor, 1:affine, 2:secant, 3:n^{eff}=10, 4:tangent, 5: second order). → see Section 5-7.

Option 3 is recommended as the standard for a self-consistent simulation.

INTERACTION=-1 allows to run a Relaxed Constraints simulation. Valid only for rolling. Assumes relaxation of shear strain components from the beginning of deformation. Not fully tested!

Line 26: parameters IUPDORI, IPDSHP, IUPDHAR.

If the corresponding parameter is =1 (default) updates grain orientation, grain shape and grain hardening after every incremental step.

If the parameter =0 it keeps the initial orientation, shape or CRSS throughout the run.

Line 27: parameter NNEIGH.

If NNEIGH=0 it does not couple the reorientation of the grains when updating orientation. This should be the default.

If NNEIGH=n it couples the reorientation of every grain with the reorientation of 'n' neighbors chosen randomly from the discrete texture file (typically NNEIGH=1). The effect of this coupling is to slow down the evolution of texture during deformation.

Line 28: parameter IBCINV (default =1). Inside SUBR VPSC solves either Eqs. 5-40 (IBCINV=1) or Eqs. 5-41 (IBCINV=0).

Line 29: parameter IFLU. If IFLU=1 calculates intragranular stress fluctuations inside grains. Slows down the run considerably. Default is IFLU=0, unless running a Second Order case (INTERACTION=5).

Line 30: parameter IRSVAR and other related parameters. Controls the outermost loop in SUBROUTINE VPSC. Default is IRSVAR=0.

Line 31: reminder

Line 32: number of sequential tests (i.e.: strain history) to be run in the simulation.

Line 33: reminder

Each process requires two lines in what follows. The first line declares IVGVAR, the second line contains information pertinent to the process, as follows.

Line 34-35+: IVGVAR.

* If IVGVAR=0 the code will enforce the same velocity gradient in every step. The load conditions are read from a PROCESS file: path\name are declared in this line

* If IVGVAR=1 the code will call SUBROUTINE VAR_VEL_GRAD at each deformation step (see description in Section 2-3). Inside the subroutine the user can either program an algorithm giving the velocity gradient at each step (see EXAMPLE 2b → rolling+shear). No PROCESS file is required in this case, but a dummy name must be used in VPSC7.IN. Else, the user can read the components of the velocity gradient from a file (typically, the deformation history of a given element generated by a FE code) whose path and name is declared in VPSC7.IN.

* If IVGVAR=2 the code calculates a 2-dimensional projection of the Polycrystal Yield Surface, by probing the aggregate with strain-rate vectors contained in the projection subspace. Instead of a PROCESS file the user should provide in this line the two components (out of the 5 deviatoric components) defining the projection sub-space (see Section 2-5 and EXAMPLE2).

* If IVGVAR=3 the code calculates the Lankford coefficient by simulating tensile tests in the (x_1,x_2) plane of the texture (see EXAMPLE2). Instead of a PROCESS file the user should provide in this line the angular increment (in degrees) for the tensile 'probing', from the RD to the TD.

The three main files, read in VPSC.IN, necessary to perform the simulations are:

a. Process file: contains the information about velocity gradient and mechanical test conditions.
b. Texture file: has the information about initial crystallographic texture
c. Deformation file: provides the information about single crystal parameters and deformation modes.

In the next pages is given all the files used to run the simulations, along with their description.

Process file: shear.ta

```
40   5 0.025   298.     nsteps   ictrl   eqincr   temp
* boundary conditions
    1       1       1           iudot     |    flag for vel.grad.
    1       1       1                     |    (0:unknown-1:known)
    1       1       1                     |
                                          |
    0.      0.      1.          udot      |    vel.grad
    0.      0.      0.                    |
    0.      0.      0.                   |
                                          |
    0       0        0           iscau    |    flag for Cauchy
            0        0                    |
                     0                    |
                                          |
    0.      0.       0.          scauchy  |    Cauchy stress
            0.       0.                   |
                     0.                  @
```

Description

```
**************************************************************************
 PROCESS file (path & name read from VPSC7.IN)
**************************************************************************
```

Line 1: parameters NSTEPS ICTRL EQINCR TEMP
NSTEPS: number of incremental deformation steps
ICTRL: Type of incremental step imposed to achieve final deformation.
* If ICTRL=0 a Von Mises equivalent strain increment is imposed.
* If 1<ICTRL<6 one of the strain or stress tensor components is imposed. Which one depends on the value of IUDOT or ISCAU read below. (Voigt convention used: 1,2,3,4,5,6 indicate 11,22,33,23,13,12 respectively)
* If ICTRL=7 the time increment TDOT is imposed and multiplies the strain rate tensor to give the strain increment.
EQINCR: Magnitude of increment imposed to achieve final deformation.
* If ICTRL=0 the EQINCR is the Von Mises strain increment
* If 1<ICTRL<6 then EQINCR is the increment of the strain tensor component or the time increment (when a creep test is enforced).
* If ICTRL=7 it is the time increment.
TEMP: temperature (not used unless running MTS hardening: IHARDLAW=1)

Line 2: reminder.
Lines 3-5: flags IUDOT(3,3) associated with each of the nine components of the velocity gradient tensor $L_{i,j}$ The corresponding component is enforced or not when IUDOT(i,j) is 1 or 0 respectively.
Lines 6-8: components of the macroscopic velocity gradient in arbitrary units. All nine are to be given in order to make an initial stress guess. Only those with IUDOT=1 are enforced.
Lines 9-11: flags ISCAU(6) associated with each of the six independent components of the Cauchy stress tensor. The corresponding component is enforced or not when ISCAU(i) is 1 or 0 respectively. ISCAU and IUDOT have to be complementary.
Lines 12-14: components of the macroscopic Cauchy stress in arbitrary units. Only those with IUDOT=1 are enforced and need to be given (usually equal to zero for free surfaces).

Texture file: 'Tantaexporiginal.tex'

```
dummy
dummy
Ta    texture     generated   by    JP.ESC      (05/24/07)
B     398   0
      321.764     58.166      40.65 0.001444565
      124.412     56.446      217.67      0.005236547
      142.257     43.278      225.76      0.003972553
      323.012     37.935      45    0.000902853
      322.883     52.141      46.97 0.002166847
      188.513     50.347      133.67      0.009389671
      20.926      43.123      312.11      0.001083424
      354.991     42.911      316.24      0.001625135
      37.474      51.091      309.48      0.002527988
      31.292      51.97 315.29      0.003250271
      157.41      40.264      232.84      0.001444565
      134.079     49.909      221.76      0.004153124
      213.429     48.375      136.88      0.001986277
      68.412      52.379      321.29      0.001083424
      36.671      52.971      313.01      0.003972553
      331.682     37.803      48.73 0.001444565
      215.599     46.492      123.76      0.001083424
      35.323      57.123      323.29      0.002708559
      21.45 46.237      314.46      0.001263994
      31.957      46.283      309.2 0.006319971
      317.964     46.945      50.81 0.003611412
      314.106     52.083      42.97 0.004333694
      189.998     22.524      127.91      0.001263994
      326.074     50.862      53    0.000902853
      130.266     50.95 221.3 0.0030697
          ...         ...       ...   ...
```

Description

****
Texture file
****

Line 1: dummy
Line 2: dummy
Line 3: dummy
Line 4: first letter of the texture convention being used (**R**oe, **B**unge, **K**ocks) and the number of orientations to be read from the file.
Line 5 to end: the three Euler angles defining each orientation, and the associated volume fraction. They are read using free format.

Deformation file: 'Ta.sxa”

```
Tantalum ELASTIC CONSTANTS AND 'HARDENING' PARAMETERS
CUBIC             crysym
   1.   1.   1.    90.   90.   90.   unit cell axes and angles
Elastic stiffness for Fe at 300K [GPa] (Simmons and Huang)
 261.0   157.4   157.4   000.0   000.0   000.0
 157.4   261.0   157.4   000.0   000.0   000.0
 157.4   157.4   261.0   000.0   000.0   000.0
 000.0   000.0   000.0    82.0   000.0   000.0
 000.0   000.0   000.0   000.0    82.0   000.0
 000.0   000.0   000.0   000.0   000.0    82.0
*Thermal expansion coefficients (single crystal in crystal axis):
  6.3e-6  6.3e-6   6.3e-6   0.0e0   0.0e0   0.0e0
INFORMATION ABOUT SLIP AND TWIN SYSTEMS
   4              nmodesx (total # of modes listed in the file)
   1              nmodes  (# of modes to be used in the calculation)
   1             mode(i) (label of the modes to be used)
   {110}<111> SLIP
  1   12   20    1                    modex,nsmx,nrsx,isensex
  0.0   0    0.   0.                   twshx,isectw,thres1,thres2
  2.   0.0     0.0    0.0     0.  0.   tau0,tau1,thet0,thet1 ,hpfac,hgnd
         1.0    1.0    1.0             hlatex
    0    1    1     1    1   -1       slip (n-b)
    1    0    1     1    1   -1
    1   -1    0     1    1   -1
    0    1   -1     1   -1   -1
    1    0    1     1   -1   -1
    1    1    0     1   -1   -1
    0    1    1     1   -1    1
    1    0   -1     1   -1    1
    1    1    0     1   -1    1
    0    1   -1     1    1    1
    1    0   -1     1    1    1
    1   -1    0     1    1    1
   {112}<111> SLIP
  2   12   20    1                    modex,nsmx,nrsx,isensex
  0.0   0    0.   0.                   twshx,isectw,thres1,thres2
  2.0   0.0   0.000  0.000    0.  0.   tau0,tau1,thet0,thet1 ,hpfac,hgnd
         1.0    1.0    1.0             hlatex
   -2    1   -1    -1   -1    1       slip (n-b)
    1   -2   -1    -1   -1    1
    1    1    2    -1   -1    1
   -2   -1   -1    -1    1    1
    1    2   -1    -1    1    1
    1   -1    2    -1    1    1
    2    1   -1     1   -1    1
   -1   -2   -1     1   -1    1
   -1    1    2     1   -1    1
    2   -1   -1     1    1    1
   -1    2   -1     1    1    1
   -1   -1    2     1    1    1
   {123}<111> SLIP
  3   24   20    1                    modex,nsmx,nrsx,isensex
  0.0   0    0.   0.                   twshx,isectw,thres1,thres2
```

```
  2.0   0.0   0.000  0.000    0.  0.  tau0,tau1,thet0,thet1 ,hpfac,hgnd
         1.0    1.0    1.0            hlatex
    1    2    3     1    1   -1       slip (n-b)
   -1    3    2     1    1   -1
    2    1    3     1    1   -1
   -2    3    1     1    1   -1
    3   -1    2     1    1   -1
    3   -2    1     1    1   -1
   -1    2   -3     1   -1   -1
    1    3   -2     1   -1   -1
    2   -1    3     1   -1   -1
    2    3   -1     1   -1   -1
    3    1    2     1   -1   -1
    3    2    1     1   -1   -1
    1   -2   -3     1   -1    1
    1    3    2     1   -1    1
    2   -1   -3     1   -1    1
    2    3    1     1   -1    1
    3    1   -2     1   -1    1
    3    2   -1     1   -1    1
    1    2   -3     1    1    1
    1   -3    2     1    1    1
    2    1   -3     1    1    1
    2   -3    1     1    1    1
   -3    1    2     1    1    1
   -3    2    1     1    1    1
   <112>{111} TWIN
 4  12  20   0                          modex,nsmx,nrsx,isensex
 0.707   0       0.100   0.500          twshx,isectw,thres1,thres2
 1.0     0.0     0.0     0.0     0.  0.  tau0,tau1,thet0,thet1
,hpfac,gndfac
       1.0   1.0                        hlat(nmodes)
   -2    1   -1    -1   -1    1
    1   -2   -1    -1   -1    1
    1    1    2    -1   -1    1
   -2   -1   -1    -1    1    1
    1    2   -1    -1    1    1
    1   -1    2    -1    1    1
    2    1   -1     1   -1    1
   -1   -2   -1     1   -1    1
   -1    1    2     1   -1    1
    2   -1   -1     1    1    1
   -1    2   -1     1    1    1
   -1   -1    2     1    1    1
```

Description

****
File 'FILECRYS':
****

Line 1: reminder
Line 2: crystal symmetry ‘ICRYST’. Could be CUBIC, HEXAGonal, TRIGOnal, ORTHOtropic, MONOClinic, TRICLinic. Only the first five letters of the word are read.

Line 3: crystal lattice parameters: relative length (a,b,c) of the unit cell axes, and angles (α, β, γ) between the axes.

Line 4: reminder

Line 5-10: elastic constants of the crystal (Voigt notation). VPSC calculates the Voigt, Reuss and Self-Consistent elastic constants of the initial texture, and writes them in RUN_LOG.OUT
Line 11: reminder
Line 12: thermal expansion coefficients of the crystal (Voigt notation). Read but ignored by VPSC.
Line 13: reminder
Line 14: total number of deformation modes listed in the file.
Line 15: the number of modes to be used in the calculation 'NMODES'.
Line 16: the correlative numbers that identify the active modes.
Line 17: a label for the mode.
Line 18: sequential # for the mode, number of systems in each mode (only the direct systems are listed), rate sensitivity 'NRS' and indicator of shear reversibility (ISENSE=1 → reversible ; ISENSE=0 → irreversible, usually associated with twinning but also works for directional slip systems).
Line 19: characteristic twin shear for the mode (TWSH) (zero for slip systems), flag for allowing secondary twin reorientation (ISECTW=1) or not (ISECTW=0), threshold volume fractions THRES1, THRES2 associated with Predominant Twin Reorientation scheme described in Section 1-7.
Line 10: parameters of the Voce law describing the hardening of the slip or twin systems that belong to this mode (see Section 1-6-1).
Line 11: latent hardening parameters $h^{ss'}$ coupling the shear in each system with the rest of the active systems (page 6). A total of 'NMODES' values are read from this line, and they couple only the modes being used in the simulation (see Section 1-6-1).
Line 11+: Miller indices of the normal and slip vectors of each system. For cubic, orthotropic & triclinic symmetry 3-index Miller notation. For hexagonal and trigonal crystals 4-index Miller-Bravais notation.

Appendix A.4 Matlab program (*.ang generator)

```
Complete program
clc;
clear;
numfile=input('Number of files to convert: ');
%textfile=input('Specimen to analyze: ','s');
addpath('C:\Documents and Settings\JuanPa\Desktop\conversion');

%****************************
%Texture file
%**********************Reading files
textfile='TEX_PH'
totalrows=0;
%numfile=1;
for m=1:numfile
      set=m;
      Nameoffile=[textfile int2str(set) '.OUT' ];
      Data(:,:,m)=importdata(Nameoffile,' ');
      data1(:,:,m)=Data(:,:,m);
      sizeoffile(:,:,m)=size(data1(:,:,m));
      totalrows=totalrows+sizeoffile(1,1,m)
end
% calculation of radians

for filesnum=1:numfile
   for rows=1:sizeoffile(1,1,filesnum)
      for I=1:3
         if (data1(rows,I,filesnum)<0)
            newdata(rows,I,filesnum)=(data1(rows,I,filesnum)+360)*3.141592/180;
         else
            newdata(rows,I,filesnum)=data1(rows,I,filesnum)*3.141592/180;
         end
      end
   end
end
angfile=[textfile int2str(set) '.ang'];
initial=3583;
final=3890;
diary texture10101.ang;
fprintf('# TEM_PIXperUM         1.000000\n');
fprintf('# x-star               0.483206\n');
fprintf('# y-star               0.737062\n');
fprintf('# z-star               0.903260\n');
fprintf('# WorkingDistance      10.000000\n');
fprintf('#\n');
fprintf('# Phase 1\n');
fprintf('# MaterialName         Molybdenum\n');
fprintf('# Formula              Mo\n');
fprintf('# Info                 \n');
fprintf('# Symmetry             43\n');
fprintf('# LatticeConstants     3.150 3.150 3.150  90.000  90.000  90.000\n');
fprintf('# NumberFamilies       4\n');
fprintf('# hklFamilies          1  1  0 1 0.000000 1\n');
fprintf('# hklFamilies          2  0  0 1 0.000000 1\n');
```

```
fprintf('# hklFamilies 2 1 1 1 0.000000 1\n');
fprintf('# hklFamilies 3 1 0 1 0.000000 1\n');
fprintf('# Categories 0 0 0 0 0\n');
fprintf('#\n');
fprintf('# GRID: HexGrid\n');
fprintf('# XSTEP: 30.000000\n');
fprintf('# YSTEP: 25.980762\n');
fprintf('# NCOLS_ODD: 19\n');
fprintf('# NCOLS_EVEN: 18\n');
fprintf('# NROWS: 28\n');
fprintf('#\n');
fprintf('# OPERATOR: Juan Pablo =)\n');
fprintf('#\n');
fprintf('# SAMPLEID:\n');
fprintf('#\n');
fprintf('# SCANID:\n');
fprintf('#\n');

for filesnum=1:numfile
   for rows=initial:final
         posix = rows;
         posiy = totalrows*100;
         fprintf('\t%5.3f\t%5.3f %8.3f %5.5f %8.5f 171.7 0.643 0 16619
0.514\n',newdata(rows,1,filesnum),newdata(rows,2,filesnum),newdata(rows,3,filesnum),posix,posiy);
   end
end
diary off;
```

Appendix A.5 Dislocation dynamics: Description of input files (data and DDinput) used for running the dislocation dynamics simulations are given next.

File: "data"

```
1.--crystal------maxstep------sidex------sidey----sidez
    'BCC'
                  1000000    5000.0         5000.0      5000.0
 2.--denisty(kg/m3)---shr(Pa)(MO)--pois--mobility(1/pa.s)--ba(m)
    16650.0     65.0e+09         0.35     100.0         2.860e-10
 3.--temper----stkFE(J/m^2) --ismobil--amfactor--Conduc--HeatCond.
       300.0    0.040            1        0.025    55.   153.
 4.-npol--ncell---ifree(0:R,1:F-R,3:P) --nsface1(3) --- nsface2(3)
    3      0           3                1 1 1        1 1 1
 5.--nscx, y, z (subcells and FEA elements)
   3  3  3
 6.--FiniteElementindexFE=0,1,2),indexFE1=0:GenData:1(Read),nfea:DD/FEA
steps
      0  0  40
 7.--Defect (loopfile 0=nodefects,1=YES)--
ndz=1(loops),2(SFT's),3(square),5(crack)
      0 1
 8.--Coordinate system (w.r.t. crystal)
      1. 0.  0.
      0.  1.  0.
      0.  0.  1.
 9.--PrintResultsEvery N steps, gnuFormt,Techplot (0:No,1:Yes)
       10           1         1
 10.--IntegOption(IDTdd=0 Const dt,1 Varible), imeshDD(0=cons, 1=auto)
      1   1
End of data-----------------------------------------------------------
```

Description

Block 1: --crystal------maxstep------side
- crystal: FCC or BCC (followed by a separate line)
- maxstep: maximum number of steps
- sidex, y, z: cell size (normalized by the magnitude of the Burgers vector)

Block 2: --density(kg/m^3)---shr(Pa)(MO)--pois--mobility(1/pa.s)--ba(m)
- density(rho): material density (kg/m^3)
- shr: shear modulus (Pa)
- pois: Poisson's ratio
- mobility(amg): dislocation mobility (of edge and mixed) (1/pa.s)
- ba(brgmgal) magnitude of burger's vector (m)

Block 3:-- temper--stkfe--ismobil--amfactor----thermk---heatc
- temper: Temperature (K)
- stkfe: Stacking Fault Energy (J/m^2)
- ismobil: 0 or 1, 0: mobility of edge = mobility of screw,
  1: mobility of screw = mobility of edge/mixed * amfactor

amfactor: = (mobility of screw)/(mobility of edge/mixed)
thermk: thermal conductivity (W/m K)
heatc: Specific heat capacity (J/Kg K)

Block 4: .--npolorder----ncell---------ifree-------nsface1(3)------nsface2(3)

npolorder: order of “superdislocation” expansion, =2
ncell: number of reflected cells (0=finite domain)
ifree: 0: rigid boundary, 1: free or reflection boundary, and 3: periodic
nsface1(3) = 1 or 0 (1=Yes free face x, y, z)
nsface2(3) = 1 or 0 (1=yes reflection boundary, x, y, z)

Block 5: .—nscx, y, z (nscx,nscy.nscz=number of subcells for long range stresses)

nscx,y,z 3,4,5..10 (not less than 3!)

Block 6:-- Finite element data

IndexFE = 0 no FEA, =1 Static FEA, =2 Dynamic FEA
IndexFE1 = 0 Generate FE data, = 1 Read FE data
Nfea Number of DD steps per one FEA step

Block 7:—Index for point defect

Loopfile: 0=no loops, 1=read loops
ndz: 1= loops, 2= SFT’s, 3=square

Block 8:—Define Coordinate system (w.r.t. crystal axis)

1. 0. 0. (direction of x-axis)
0. 1. 0. (direction of y-axis)
0. 0. 1. (direction of z-axis)
(in this example the cell axes are in the same direction of the crystal axes.)

Block 9: How often the results is printed out and written to **RESTART.FILE** (nndx)
Gnuformat (=1, if gnuplot format output is required),
techplotformat(=1, if techplot format output is required)

50 0 1

Block10.—Integration Option (IDTdd=0 constant time step deltt: =1 variable time step)
Meshing Option (imeshDD=0 constant remeshing,=1 auto remeshing)

File: “DDinput”

```
       2007
 1: total node  fixed  erate indxerate  jn jogn nstep ntotal
          20   100.0000       100.000000               5           0
0
           0           0
 2: timenow totalstrn stress deltt   dbt   load_type
  0.0000000E+00  0.0000000E+00  0.0000000E+00  9.9999999E-09
1.0000000E-07
           0
 3: Strain tensor
  0.0 0.0 0.0 0.0 0.0 0.0
 4: Applied stress tensor
   0.0 0.0 0.0  0.0  0.0  0.0
 5: Coordinates,bs
  -2500.       -1350.0      1000.0           0.5773503      0.5773503
  0.5773503
  -1000.0       150.0      2500.0           0.5773503      0.5773503
  0.5773503
  -800.0       -700.0    -2500.0            0.5773503      0.5773503
```

```
  0.5773503
  2400.0          2500.0      700.0          0.5773503      0.5773503
  0.5773503
   -300.00        -2500.0     0.0             0.5773503      0.5773503
  0.5773503
   2200.0         00          2500            0.5773503      0.5773503
  0.5773503
   300.0          -2500.0     100.0           0.5773503      0.5773503
  0.5773503
   2500.00       -300.0      2300.0         0.5773503      0.5773503
  0.5773503
   800.0          0.0         -2500.0         0.5773503     0.5773503
  0.5773503
   2500.0         1700.0      -800.0          0.5773503     0.5773503
  0.5773503
   -2500.0        -705.0      -600.0          0.5773503     0.5773503
  0.5773503
   600.0          2395.0      2500.0          0.5773503     0.5773503
  0.5773503
   -2500.0        400.0       -1180.0         0.5773503     0.5773503
  0.5773503
   -400.0         2500.0      920.0           0.5773503     0.5773503
  0.5773503
   -2500.0        300.0       570.0           0.5773503     0.5773503
  0.5773503
   -570.0         2230.0      2500.0          0.5773503     0.5773503
  0.5773503
  -1000.0         -2500.0     -500.0          0.5773503    0.5773503
  0.5773503
  2000.0          500.0       2500.0          0.5773503    0.5773503
  0.5773503
  -2500           -2500.0     -2500.0         0.5773503    0.5773503
  0.5773503
  2500.0          2500.0      2500.0          0.5773503    0.5773503
  0.5773503
6: nbrs, PLANE TYPE constraint  xslip btype
0           2           0           6           7           1
1           0           0           6           7           1
0           4           0           3           7           1
3           0           0           3           7           1
0           6           0           1           7           1
5           0           0           1           7           1
0           8           0           3           7           1
7           0           0           3           7           1
0          10           0           6           7           1
9           0           0           6           7           1
0          12           0           1           7           1
11          0           0           1           7           1
0          14           0           3           7           1
13          0           0           3           7           1
0          16           0           1           7           1
15          0           0           1           7           1
0          18           0           6           7           1
17          0           0           6           7           1
0          20           0           6           7           1
19          0           0           6           7           1
```

Description

Line 0: The year the file DDinput was created

Line 1: node fixed erate indxerate jn jogn nstep ntotal

node: the initial total number of nodes
fixed: the initial value of average segment length (in Burgers vector)
erate: strain rate (1/s)
indxerate: strain (or stress) component with strain rate erate
indxerate = 1, 2, 3, 4, 5, 6
ε_{11} ε_{22} ε_{33} ε_{23} ε_{13} ε_{12}
jn: initial number of junction nodes
jogn: initial number of jogs (nodes)
nstep: number of steps already executed (if restarting form an earlier run)
ntotal: number of iterations already executed (if restarting form an earlier run)

Line 2: timenow totalstrn totalstress deltt dbt loadtyp (0 or 1)
timenow:
totalstrn: total strain at nstep
totalstress total stress at nstep
deltt: time step during iteration
dbt: time step (made up the sum of deltt)
loadtyp: =0 for constant strain rate
=1 for constant stress (creep).

Line 3: strain increment 6 components

Line 4: external stress 6 components

Line 5: coordinates and Burgers vector for each node
coordinates: x, y, z for each node
Burgers vecto: x,y,z components for wach node

Line 6: list neighbors of each node, plane type , constraint , Burgers Vector Index (ixbtyp(i))
plane type (iplane(i)): For each node
constraint (icn(i)): For each node (0,1,…)
Burgers Vector index: For each node (1,2,..)

Line 7: Number of defects (if any). followed by Defect size, plane & Coordinates)for each defect.

Type of Nodal Constraints and Corresponding Index icn(i)

Table A5.1: Nodal constraints

Constraint Type	**icn(i) index**
Free node	0
Surface node:	
On yz plane	1
On xz plane	2
On xy plane	3
Node at corner	4
Cross-slip node	5
Pinned node	7
Jog node	9
Junction node	10

Table A5.2: Vectors assigned to each dislocation node

Main Vector	**For Each Node**
cx(i), cy(i), cz(i)	x, y, z coordinates
nbr(i,1), nbr(i,2), nbr(i,3)	defines neighbors
glbx(i), glby(i), glbz(i)	x, y, z components of Burgers vector
bjuncx(i), bjuncy(i),bjuncz(i)	x, y, z components of Burgers vector of junction
iplane(i)	index defining slip plane
ixbtype(i)	index defining Burgers vector
ixpltyp(i,j)	index defining common planes “j” for each Burgers vector “i” (e.g. for fcc, j=1,2 ixpltyp(1,1)=3 ixpltyp(1,2)=4)
icn(i)	constraint index defining motion of node
glveL(i)	glide velocity of segments
pchx(i), pchy(i), pchz(i)	x, y, z components of Peach Koehler force
fglide(i)	glide force
jndx(i)	junction index = 0 $\Rightarrow$ node not a junction node, or = junction number
jogndx(i)	jog index = 0 $\Rightarrow$ node not a jog or = jog number

The slip planes {110} and {112} are considered. There are 18 possible slip planes, and four Burgers vector. See Appendix A for all possible slip systems. A screw dislocation for a given Burgers vector could cross-slip on any of six planes defined by the index ixpltyp(i,j).

Table A5.3: Indices for slips planes and Burgers vectors (bcc)

Slip Planes		Data for cross-slip in BCC for planes {110} & {112}				
Index iplane(i)	Plane	Burgers Vector Index ixbtyp(i)	Burgers Vector	cross-slip index ixpltyp(i,j)	Slip System	
1	$(01\bar{1})$	1	[111]	1	$[111]\ (01\bar{1})$	1
2	(011)			3	$[111]\ (10\bar{1})$	2
3	$(10\bar{1})$			6	$[111]\ (1\bar{1}0)$	3
4	(101)			9	$[111]\ (2\bar{1}\bar{1})$	4
5	(110)			12	$[111]\ (11\bar{2})$	5
6	$(1\bar{1}0)$			15	$[111]\ (1\bar{2}1)$	6
7	$(2\bar{1}1)$	2	$[\bar{1}1\bar{1}]$	2	$[\bar{1}1\bar{1}]\ (011)$	7
8	$(21\bar{1})$			3	$[\bar{1}1\bar{1}]\ (10\bar{1})$	8
9	$(2\bar{1}\bar{1})$			5	$[\bar{1}1\bar{1}]\ (110)$	9
10	(211)			8	$[\bar{1}1\bar{1}]\ (21\bar{1})$	10
11	$(\bar{1}\bar{1}2)$			16	$[\bar{1}1\bar{1}]\ (\bar{1}21)$	11
12	$(11\bar{2})$			13	$[\bar{1}1\bar{1}]\ (1\bar{1}\bar{2})$	12
13	$(1\bar{1}\bar{2})$	3	$[\bar{1}\bar{1}1]$	2	$[\bar{1}\bar{1}1]\ (011)$	13
14	$(\bar{1}1\bar{2})$			4	$[\bar{1}\bar{1}1]\ (101)$	14
15	$(1\bar{2}1)$			6	$[\bar{1}\bar{1}1]\ (1\bar{1}0)$	15
16	$(\bar{1}21)$			7	$[\bar{1}\bar{1}1]\ (2\bar{1}1)$	16
17	$(\bar{1}\bar{2}1)$			11	$[\bar{1}\bar{1}1]\ (\bar{1}\bar{1}\bar{2})$	17
18	$(\bar{1}\bar{2}\bar{1})$			18	$[\bar{1}\bar{1}1]\ (\bar{1}\bar{2}\bar{1})$	18
		4	$[\bar{1}11]$	1	$[\bar{1}11]\ (01\bar{1})$	19
				4	$[\bar{1}11]\ (101)$	20
				5	$[\bar{1}11]\ (110)$	21
				10	$[\bar{1}11]\ (211)$	22
				14	$[\bar{1}11]\ (\bar{1}1\bar{2})$	23
				17	$[\bar{1}11]\ (\bar{1}\bar{2}1)$	24

Appendix A.6 Modification of the BCC subroutine: a modification based

```
CCCCCCCCCCCCCCCCCCCCCCCCCCCCCCCCCCCCCCCCCCCC
CCCC JP subroutine = ) CCCCCCCCCCCCCCCCCCCC
CCCCCCCCCCCCCCCCCCCCCCCCCCCCCCCCCCCCCCCCCCCC

       subroutine jprandom

       include "hmz.h"
       Parameter(wallbuffer=0.0,diag=0.57735026918963)
       Parameter(maxiter=100, fos=1.5)
       Parameter (b_mag = 2.86e-10)   !Magnitude of the Burgers vector

       Real Lmin, Lmax, Lrange, Lsrc, Lsq, numerator
       INTEGER s,step

       Print*,"Enter the number of screws"
       Read(*,*), NFRS
       Print*, "NFRS = ", NFRS
       Print*


       Print*,"Enter a seed value,s, for random number generation"
       Print*,"as a large integer say from 100001-200001:"
       Read(*,*), s
       Print*,"initial seed value, s = ", s
       Print*

       ss = s   !This stores the seed value in the variable ss
       step = INT(ran(ss)*10)   !step ranges from 0-10
       Print*,"step = ",step
       Print*

       density1 = 0.0   !dislocation density

C      nodesold = nodes

       Do i=1,NFRS*2,2
       ii = i + nodes

C      Randomly selecting the x,y spatial coordinates of the first node
C      , node i,
7      x = ran(s)          !x ranges from 0 to 1
       y = ran(s)          !y ranges from 0 to 1


       x = 2.0*x - 1.0     !x ranges from -1 to 1
       y = 2.0*y - 1.0     !y ranges from -1 to 1


       cx(ii) = halfx*x
       If (abs(cx(ii)) .ge. (halfx-wallbuffer)) then
           sign  = cx(ii)/abs(cx(ii))
           cx(ii) = cx(ii) - sign*fos*wallbuffer
       End if
       cy(ii) = halfy*y
```

```
            If (abs(cy(ii)) .ge. (halfy-wallbuffer)) then
                sign  = cy(ii)/abs(cy(ii))
                cy(ii) = cy(ii) - sign*fos*wallbuffer
            End if
            cz(ii) = halfz*z


      c     This determines the {011} glide plane for the current node
source.
      C     (i.e. for node ii).
      C     The plane is defined by its unit normal vector (a,b,c)

               p = ran(s)
               IF (p .le. 0.15) Then
                   iplane(ii)= 1
                   aa = c1x(1)
                   bb = c1y(1)
                   cc = c1z(1)
               Else if (p .le. 0.30) Then
                   iplane(ii)= 2
                   aa = c1x(2)
                   bb = c1y(2)
                   cc = c1z(2)
               Else if (p .le. 0.45) Then
                   iplane(ii)= 3
                   aa = c1x(3)
                   bb = c1y(3)
                   cc = c1z(3)
               Else if (p .le. 0.60) Then
                   iplane(ii)= 4
                   aa = c1x(4)
                   bb = c1y(4)
                   cc = c1z(4)
               Else if (p .le. 0.80) Then
                   iplane(ii)= 5
                   aa = c1x(5)
                   bb = c1y(5)
                   cc = c1z(5)
               Else
                   iplane(ii)= 6
                   aa = c1x(6)
                   bb = c1y(6)
                   cc = c1z(6)
               End if
               print*, "ii, iplane(ii), a,b,c ",ii,iplane(ii),aa,bb,cc


      C     Randomly determining the length of the current dislocation,
Lsrc,
      C     such that: 0.7halfx<Lsrc<halfx
            iterations1 = 0
      11    sl = ran(s)
            Lsrc = halfx*(1-0.3*sl)
            Print*, "ii, Lsrc = ", ii, Lsrc

      C     Determining the line sense vector of the current dislocation
line.
```

```
      C      This is the vector t=(tx,ty,tz)
             asq = aa*aa
             bsq = bb*bb
             csq = cc*cc

      15     sign = ran(s)
             IF (sign .le. 0.5) Then
                 sign = 1.0
             Else
                 sign = -1.0
             End if

             tx = sign*ran(s)      !-1.0<tx<+1.0
      C      txmax = 1.0/sqrt(2.0) !This is if we know the max. x-component
of t
                                   !based on geometric constraints
      C      tx = tx*txmax
             if(aa.gt.0.0.and.bb.gt.0.0.and.cc.gt.0.0)then
             a3 = bsq + csq
             b3 = 2.0*aa*bb*tx
             c3 = (asq+csq)*tx*tx - csq
             discriminant = b3*b3 - 4.0*a3*c3
             Print*,"ii, discriminant = ",ii, discriminant
             IF (discriminant .lt. 0.0) THEN
                Print*,"Negative discriminant! Going back to 15"
                GOTO 15
             End if

             coinflip = ran(s)
             If (coinflip .le. 0.5) Then
               ty = (-b3 + sqrt(discriminant))/(2.0*a3)
             Else
               ty = (-b3 - sqrt(discriminant))/(2.0*a3)
             End if

             tz = -(aa*tx + bb*ty)/cc
             Print*,"ii, tx, ty, tz = ",ii, tx, ty, tz
             eq = tx*tx + ty*ty + tz*tz
             Print*,"ii, eq = ",ii, eq
            else
            endif

            if(cc.eq.0.0)then
             ty=(-aa*tx)/bb
             tz=ran(s)
             mag=sqrt(tx**2+ty**2+tz**2)
             tx=tx/mag
             ty=ty/mag
             tz=tz/mag
             else
               if(aa.eq.0.0)then
                 ty = sign*ran(s)      !-1.0<tx<+1.0
                 tx =  ran(s)
                 tz=(-bb*ty)/cc
                 mag=sqrt(tx**2+ty**2+tz**2)
                 tx=tx/mag
                 ty=ty/mag
```

```
                tz=tz/mag
              else
                if(bb.eq.0.0)then
                  tz = sign*ran(s)      !-1.0<tx<+1.0
                  ty =  ran(s)
                  tx=(-cc*tz)/aa
                  mag=sqrt(tx**2+ty**2+tz**2)
                  tx=tx/mag
                  ty=ty/mag
                  tz=tz/mag
              else
                endif
               endif
              endif

      C       Determining the coordinate of node ii+1, based on the unit
vector t
              cx(ii+1) = cx(ii) + Lsrc*tx
              cy(ii+1) = cy(ii) + Lsrc*ty
              cz(ii+1) = cz(ii) + Lsrc*tz

              IF (iterations1 .ge. maxiter) GOTO 7

              IF ( (abs(cx(ii+1)) .ge. (halfx-wallbuffer))
             2 .or. (abs(cy(ii+1)) .ge. (halfy-wallbuffer))
             3 .or. (abs(cz(ii+1)) .ge. (halfz-wallbuffer)) ) Then
                   iterations1 = iterations1 + 1
                   GOTO 11
              End IF
              Print*,"iterations1 = ",iterations1

      C       Determining the separation distance, dist, between the
      C       paired FR sources such that: distmin<dist<distmax
              iterations2 = 0
      17      ssep = ran(s)
              dist = distmin + distrange*ssep
              Print*, "ii, separation distance = ", ii, dist

      C       Assigning plane indices for the rest of the nodes in the FR pair
              iplane(ii+1) = iplane(ii)

      C       Determining the length of the FR source pair in units of b.
      C       This is needed for dislocation density calcuation.
              dx = cx(ii+1) - cx(ii)
              dy = cy(ii+1) - cy(ii)
              dz = cz(ii+1) - cz(ii)
              src_pair_length = 2.0*sqrt(dx*dx + dy*dy + dz*dz)
              density1 = density1 + src_pair_length
      C Zbib ! I am here

      C       Selecting the Burgers vector index for nodes ii, ii+1, ii+2 &
ii+3
              Call bindex(iplane(ii), s, ixtyp(ii))
              ixtyp(ii+1) = ixtyp(ii)
              s = s + step   !Changing the seed value to a new
              End Do
```

```
C       Calculating initial dislocation density
        volume = sidex*sidey*sidez
        density1=Lsrc*NFRS
        density1= density1/volume /(b_mag*b_mag)
        Print*
        Print*,"Dislocation density = ",density1
        Print*

        density = density + density1  !Total dislocation density


        Do i = 1,  2*NFRS, 2
           ii= i + nodes
           nbr(ii,1) = 0
           nbr(ii,2) = ii+1
           nbr(ii,3) = 0
           icn(ii) = 0
           jndx(ii) = 0
           jogndx(ii) = 0
           bjuncx(ii) = 0.0
           bjuncy(ii) = 0.0
           bjuncz(ii) = 0.0

           nbr(ii+1,1) = ii
           nbr(ii+1,2) = 0
           nbr(ii+1,3) = 0
           icn(ii+1) = 0
           jndx(ii+1) = 0
           jogndx(ii+1) = 0
           bjuncx(ii+1) = 0.0
           bjuncy(ii+1) = 0.0
           bjuncz(ii+1) = 0.0

        End Do
        Do ii = 1, 2*NFRS
           i= ii + nodes
           IF (ixtyp(i) .eq. 1) Then
              glbx(i) = b(1,1)
              glby(i) = b(1,2)
              glbz(i) = b(1,3)
           Else if (ixtyp(i) .eq. 2) Then
              glbx(i) = b(2,1)
              glby(i) = b(2,2)
              glbz(i) = b(2,3)
           Else if (ixtyp(i) .eq. 3) Then
              glbx(i) = b(3,1)
              glby(i) = b(3,2)
              glbz(i) = b(3,3)
           Else if (ixtyp(i) .eq. 4) Then
              glbx(i) = b(4,1)
              glby(i) = b(4,2)
              glbz(i) = b(4,3)
           Else if (ixtyp(i) .eq. 5) Then
              glbx(i) = b(5,1)
              glby(i) = b(5,2)
              glbz(i) = b(5,3)
```

```
   Else
      glbx(i) = b(6,1)
      glby(i) = b(6,2)
      glbz(i) = b(6,3)
   End if
End Do


nodes = nodes + 2*NFRS

Return
End
```

Appendix A.7 Comparison of the Experimental data vs SGL Model

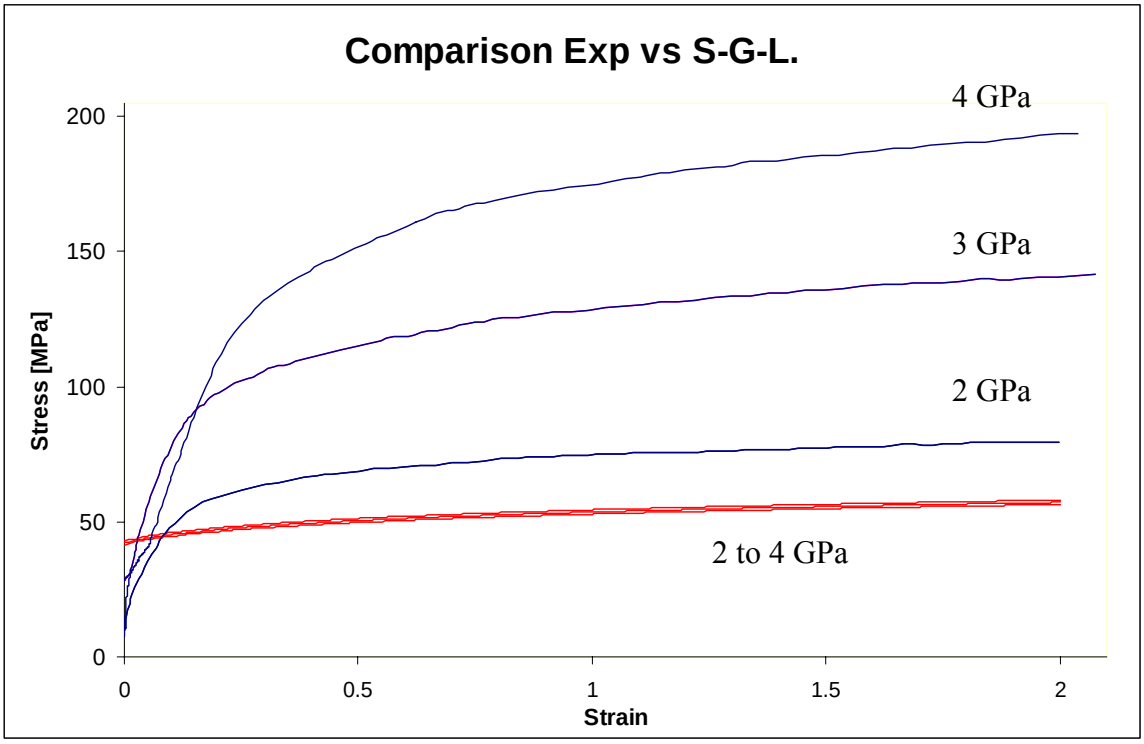

Figure A.7.1 Comparison of the effective stresses experimental vs. predicted by SGL.

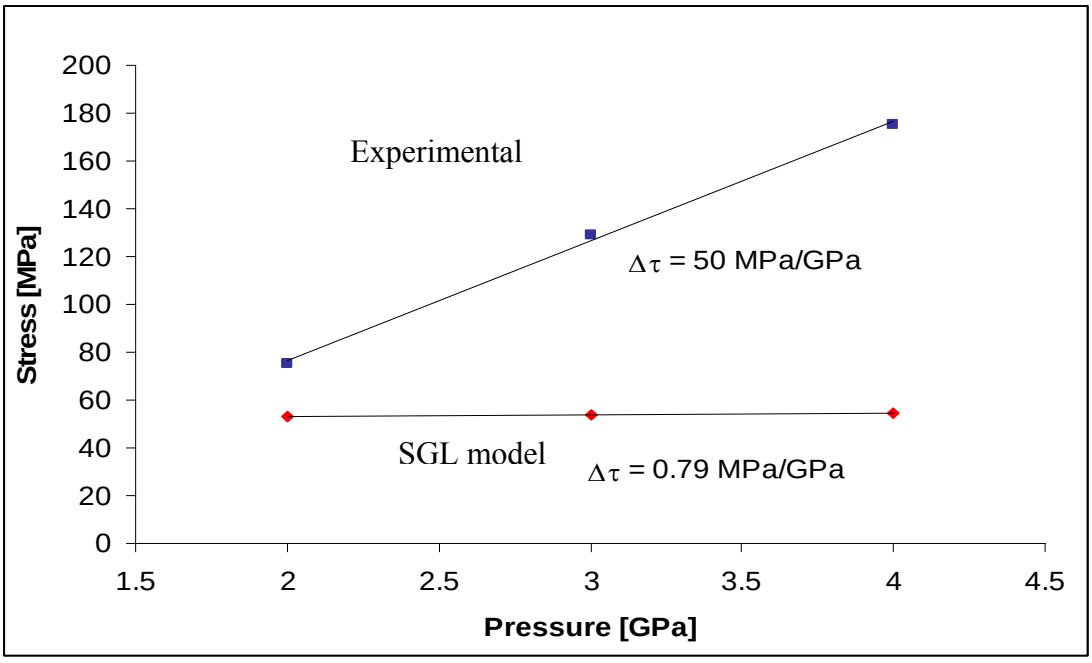

Figure A.7.2 Comparison of stress: experimental vs. SGL at strain =1.